MEASUREMENT OF THE $t\bar{t}$ DIFFERENTIAL CROSS SECTION, $d\sigma/dM_{t\bar{t}}$, IN $p\overline{p}$ COLLISIONS AT $\sqrt{s} = 1.96$ TEV

BY

ALICE PATRICIA BRIDGEMAN

B.A., The Johns Hopkins University, 2003

DISSERTATION

Submitted in partial fulfillment of the requirements
for the degree of Doctor of Philosophy in Physics
in the Graduate College of the
University of Illinois at Urbana-Champaign, 2008

Urbana, Illinois

Doctoral Committee:

Professor Mats Selen, Chair
Professor Tony Liss, Director of Research
Professor John Stack
Assistant Professor Brian DeMarco

Abstract

I present a measurement of the $t\bar{t}$ differential cross section, $d\sigma/dM_{t\bar{t}}$, in $p\overline{p}$ collisions at $\sqrt{s} = 1.96$ TeV using 2.7 fb^{-1} of CDF II data. I find that $d\sigma/dM_{t\bar{t}}$ is consistent with the Standard Model expectation, as modeled by `PYTHIA` with `CTEQ5L` parton distribution functions. I set limits on the ratio κ/M_{Pl} in the Randall-Sundrum model by looking for Kaluza Klein gravitons which decay to top quarks. I find $\kappa/M_{Pl} > 0.16$ at the 95% confidence level.

Acknowledgments

The last five years have been at times exciting, frustrating, very sad and very happy for me. I can say with certainty that I would not have come this far without the love and support of my wonderful parents, Dennis and Elizabeth Bridgeman. I remember when I was a child the first job I wanted was that of an elephant-rider in the circus. Well, I turned out to be a physicist, but I know they would have been there for me, helping me be the best elephant-rider in the world if that's what I wanted to become.

I also must thank the entire University of Illinois High Energy Group - my fellow grad students and postdocs, past and present, and all of the professors. Of course my advisor, Tony Liss, deserves top billing. He entrusted me to complete this analysis largely independently, which was a huge challenge but also incredibly rewarding in the end. Of course, no one really does a high energy physics analysis by themselves. I received incredible help from former U of I postdoc Anyes Taffard. Anyes does amazing work, in both quality and quantity, and I thank her for being an inspiration. Tom Schwarz not only convinced me to do SVD unfolding, but also helped me get it working. Tom also did the majority of the work on the background estimates which many people, including me, use. I thank him for sharing and letting me graduate that much faster. Erik Brubaker was extremely helpful for the last round of the analysis, it was really his insistence that things be done right that caused the final result to improve as much as it did. I could not have made my beyond the Standard Model Monte Carlo samples without the help of the top Monte Carlo coordinator Nate Goldschmidt. Thank you, Nate! Kevin Lannon and Charles Plager also helped me many times with top code. And for those many other collaborators I did not mention, and the vast technical staff at CDF and Fermilab, I thank you as well for your hard work - without you, I would have no data to analyze.

I must also thank my fellow graduate students that I have become friends with over the years. I will miss (or already do) Joe Gezo, Dan Vandervelde, Josh Sayre, Kevin Mantey, Alice Quisno, James Reed and the other assorted members of the Dos crew. I must also thank Ed Rogers, who has been my kindred spirit in the CDF group and helped me pass the qual. You have all made graduate school the best part of my now extremely long academic journey. Outside of physics I thank Jamie Bond for being a great friend and running buddy. I thank James Patrick for getting me to Illinois and past the prelim.

Finally I thank Kevin Inderhees for being with me through the very difficult process of finishing a dissertation. Thank you for putting up with my attempts to solve all problems when I should be sleeping and for my strange affinity for 80's rock tunes while writing. I'm sorry I will not be with

you in Urbana while you write your dissertation, but you will get through it and we can get Boris the orange cat when you are done.

This work was supported in part by the United States Department of Energy under grant DE-FG02-91ER40677.

Table of Contents

List of Tables . . . . . **viii**

List of Figures . . . . . **x**

Chapter 1 Introduction to Top Quark Physics **1**
1.1 Introduction 1
1.2 The Standard Model 2
1.2.1 Quantum Electrodynamics 3
1.2.2 Quantum Chromodynamics 3
1.2.3 The Weak Interactions 4
1.3 $t\bar{t}$ Production and Decay 13
1.3.1 $t\bar{t}$ Production at the Tevatron 13
1.3.2 Top Decay 17
1.4 The Top Quark in Physics Beyond the Standard Model 17

Chapter 2 The Fermilab Tevatron and the CDF II Detector **20**
2.1 Introduction 20
2.2 The Tevatron 20
2.3 CDF II Detector 21
2.3.1 Tracking Systems 22
2.3.2 Calorimetry 24
2.3.3 Muon Systems 24
2.3.4 Luminosity Measurement 25
2.3.5 Trigger 25

Chapter 3 Monte Carlo Models for Signal and Background **27**
3.1 Introduction 27
3.2 Monte Carlo Event Generation 27
3.2.1 Signal Event Generation 28
3.2.2 Background Event Generation 28
3.3 CDF Detector Simulation 29

Chapter 4 $t\bar{t}$ Event Selection **30**
4.1 Introduction 30
4.2 Event Selection 31
4.2.1 Trigger 31
4.2.2 Lepton Identification 32
4.2.3 Track and Primary Vertex Reconstruction 34
4.2.4 Jet Reconstruction and Uncertainties 34
4.2.5 Missing Transverse Energy Reconstruction 40

4.3 Heavy Flavor Tagging . . . 40
4.4 $t\bar{t}$ Signal . . . 41
4.4.1 Acceptance . . . 41
4.4.2 Reconstruction of $t\bar{t}$ Events . . . 44
4.5 Data Sample . . . 45

Chapter 5 Standard Model $t\bar{t}$ Backgrounds . . . 46
5.1 Introduction . . . 46
5.2 Normalization of the Backgrounds . . . 47
5.2.1 Electroweak and Monte Carlo Derived Backgrounds . . . 48
5.2.2 $t\bar{t}$ in the Pretag W+jets Sample . . . 48
5.2.3 Non-W Background Production . . . 49
5.2.4 W+heavy flavor Production . . . 49
5.2.5 Mistag Production . . . 50
5.2.6 Tagged Electroweak and non-W Backgrounds . . . 50
5.3 Data Sample Composition . . . 51
5.4 $M_{t\bar{t}}$ Distribution of the Backgrounds . . . 52

Chapter 6 A Review of Previous Results . . . 53
6.1 Introduction . . . 53
6.2 Searches for Narrow Resonances . . . 53
6.3 Search for Massive Gluons . . . 59

Chapter 7 Analysis Method . . . 62
7.1 Introduction . . . 62
7.2 Unfolding . . . 63
7.2.1 A Simple Example . . . 64
7.2.2 The Need for Regularization . . . 66
7.2.3 Regularized Unfolding . . . 66
7.2.4 Choosing the Regularization Parameter . . . 69
7.2.5 Algorithm Summary . . . 70
7.2.6 Implementing the Algorithm . . . 70
7.2.7 Unfolding the $M_{t\bar{t}}$ Distribution . . . 70
7.3 Calculating $d\sigma/dM_{t\bar{t}}$ . . . 72

Chapter 8 Systematic Uncertainties . . . 76
8.1 Introduction . . . 76
8.2 Sources of Uncertainty . . . 76
8.3 Evaluating Systematic Uncertainties . . . 78
8.4 Expected Sensitivity of the Analysis . . . 78

Chapter 9 Reducing the Systematic Uncertainties . . . 80
9.1 Introduction . . . 80
9.2 Measurement of Δ_{JES} from the Dijet Invariant Mass Distribution . . . 80
9.3 Parameterizing the Response Matrix . . . 84
9.4 Parameterizing the Acceptance . . . 84
9.5 Tests of Analysis Procedure with *in-situ* Jet Energy Scale Calibration . . . 84
9.6 New Systematic Uncertainties . . . 91

Chapter 10 Results . . . 93
10.1 Introduction . . . 93
10.2 Kinematic Distributions . . . 93
10.3 M_{jj} Fit . . . 93
10.4 Unfolding . . . 96
10.5 Differential Cross Section . . . 96
10.6 Cross Checks . . . 99

Chapter 11 Consistency with the Standard Model and Limits on New Physics . 101
11.1 Introduction . . . 101
11.2 Generation of RS Monte Carlo Events . . . 101
11.3 Setting Limits with CL_s . . . 102
11.3.1 The Anderson-Darling Statistic . . . 103
11.3.2 Constructing the Distributions . . . 104
11.4 Limits on the Coupling of RS Gravitons to Top Quarks . . . 105

Chapter 12 Conclusions . . . 107

References . . . 108

Author's Biography . . . 112

List of Tables

1.1 The quarks and leptons of the Standard Model. [1, 2] 2
1.2 The gauge bosons of the Standard Model. 3
1.3 Summary of representation of the first generation fermions under $SU(2)$ and their hypercharge. The same holds for the second and third generations. 9

3.1 Summary of Monte Carlo programs used to generate events for different classes of background events. 28

4.1 Possible final states of W^+ and W^- $t\bar{t}$ daughters. The numbers are the percentage of the decays with that final state. 30
4.2 Summary of event selection used in this analysis. 31
4.3 Binning of $M_{t\bar{t}}$ used in this analysis. 31
4.4 Efficiencies of the various triggers used in this analysis. 32
4.5 Requirements for electron identification. 33
4.6 Requirements for muon identification. 34
4.7 Acceptances for events with CEM, CMUP and CMX leptons which pass the event selection. The bins are defined in Table 4.3. 43
4.8 Event selection efficiency for events which pass the event selection according to lepton type and $M_{t\bar{t}}$ bin. The bins are defined in Table 4.3. 43
4.9 The event counts after event selection according to lepton trigger type and jet bin. The signal region is $\geq$ 4-jets, for a total of 650 events in 2.7 fb^{-1} of data. 45

5.1 Cross sections used in calculation of Monte Carlo derived backgrounds. [33] 48
5.2 Fraction of W+jets events with heavy flavor content (in percents), and the tagging efficiency for the events. 49
5.3 Predicted sample composition in each jet bin for 2.7 fb^{-1} of data. [36] 51

7.1 The mean and widths of the pull for the number of unfolded events in each bin, as defined in Equation 7.48, for pseudo-experiments constructed with $t\bar{t}$ signal only. . . 73
7.2 Denominator in bins of $M_{t\bar{t}}$, assuming 2.7 fb^{-1} of data. 74
7.3 The mean and widths of the pull for the number of unfolded events in each bin, as defined in Equation 7.48, for pseudo-experiments constructed with both signal and background events. 75

8.1 Summary of systematic uncertainties on $d\sigma/dM_{t\bar{t}}$ in each bin. All uncertainties are given as percentages. The bins are defined in Table 4.3. 78
8.2 Summary of total expected uncertainties. All uncertainties are given as percentages. 79

9.1 The mean and widths of the pull for the number of unfolded events in each bin, as defined in Equation 7.48, at various Δ_{JES} points. 90

9.2 Summary of systematic uncertainties on $d\sigma/dM_{t\bar{t}}$ in each bin for the improved analysis with Δ_{JES} fit. All uncertainties are given as percentages. The bins are defined in Table 4.3. 91
9.3 Summary of total expected uncertainties. All uncertainties are given as percentages 92
9.4 Comparison of expected uncertainties for the baseline analysis with no Δ_{JES} fit and the improved analysis with the Δ_{JES} fit. All uncertainties are given as percentages and the total does not include the uncertainty due to the luminosity measurement. . 92

10.1 Measured $d\sigma/dM_{t\bar{t}}$ in 2.7fb^{-1} of data. 98
10.2 Comparison of results in different sub-samples of the data. 100

11.1 Cross Sections for RS gravitons at various κ/M_{Pl} points. 102

List of Figures

1.1 The variation of α_s with energy [1]. 5
1.2 The Feynman diagram for the decay of π^+. 5
1.3 The Feynman diagram for the decays $D^0 \to K^{\pm}\pi^{\mp}$. 6
1.4 The leptonic left-right production cross section asymmetry as measured by two experiments at LEP [5]. 6
1.5 The leading order diagrams for $t\bar{t}$ production at the Tevatron. 13
1.6 The theoretical and measured cross sections for various processes of interest at the Tevatron. Plot courtesy of Mark Neubauer. 14
1.7 The pdf of the proton, as given by the `CTEQ5L` [6] dataset, for a Q^2 of 1600 GeV^2. . 15
1.8 The variation of the $t\bar{t}$ production cross section with top mass. The data point indicates the combination of CDF measurements of the top quark mass and $t\bar{t}$ production cross sections. 16
1.9 The best fit Higgs mass from a global fit to precision electroweak data, assuming the SM theory [8]. 18

2.1 The Fermilab Tevatron accelerator chain. 21
2.2 The integrated luminosity delivered and recorded by the CDF II detector. 21
2.3 An elevation view of the CDF II detector. 22
2.4 A schematic of the CDF II trigger system. The clock cycle shown is 132 ns, but the Tevatron currently operates at 396 ns. 26

4.1 The ratio of probe to trigger jet p_T [31]. 36
4.2 The uncertainties on the η-dependent jet corrections in various jet p_T bins [31]. . . . 36
4.3 The average transverse energy in a cone of radius R=0.4 in a minimum bias data sample [31]. 37
4.4 The uncertainty of the multiple interaction correction as function of jet p_T [31]. . . . 38
4.5 The absolute jet energy scale correction with uncertainties are a function of jet p_T [31]. 38
4.6 The underlying event jet energy scale correction with uncertainties are a function of jet p_T [31]. 39
4.7 The out of cone jet energy scale correction with uncertainties are a function of jet p_T [31]. 39
4.8 The total uncertainty on the jet energy scale as a function of jet p_T [31]. 40
4.9 A cartoon jet with a displaced secondary vertex [35]. 42
4.10 `SecVtx` b-tagging efficiency for $t\bar{t}$ events as a function of jet E_T. [35]. 42

5.1 The output of the neural network used to calculate the fraction of heavy flavor in data [36] 50
5.2 The mistag rate of the tight `SecVtx` tagger. [35] 51

5.3 The expected $M_{t\bar{t}}$ distribution of the backgrounds. The signal distribution is shown for reference. 52

6.1 The distribution of $M_{t\bar{t}}$ obtained using the matrix element technique [39]. 54
6.2 The observed and expected limits on Z' production obtained using the matrix element technique [39]. 55
6.3 The distribution of $M_{t\bar{t}}$ obtained using the χ^2 reconstruction technique [41]. 56
6.4 The observed and expected limits for a narrow Z'-like resonance obtained using the χ^2 reconstruction technique [41]. 57
6.5 The distribution of $M_{t\bar{t}}$ obtained from reconstructed objects in events with 3 jets [43]. 57
6.6 The distribution of $M_{t\bar{t}}$ obtained from reconstructed objects in events with 4 or more jets [43]. 58
6.7 The observed and expected limits for a narrow Z'-like resonance obtained using reconstructed objects for $M_{t\bar{t}}$ [41]. 58
6.8 The distribution of $M_{t\bar{t}}$ obtained using a modified matrix element technique [44]. . . 59
6.9 The 95% confidence level limits for narrow color octet resonances [44]. 60
6.10 The 95% confidence level limits for wide color octet resonances [44]. 61

7.1 True $M_{t\bar{t}}$ versus reconstructed $M_{t\bar{t}}$ in $t\bar{t}$ Monte Carlo simulation. 63
7.2 The logarithm of the elements of d, as defined in Equation 7.38 versus i. 71
7.3 The unfolded distribution, with $k = 4$, as compared to the true distribution. 71
7.4 The unfolded distribution, with $k = 1$, as compared to the true distribution. The solution is over-regulated. 72
7.5 The unfolded distribution, with $k = 8$, as compared to the true distribution. The solution is under-regulated. 73

9.1 The reconstructed M_{jj} signal distribution in Monte Carlo events at various values of Δ_{JES}. 81
9.2 The reconstructed M_{jj} background distribution at various values of Δ_{JES}. 82
9.3 The reconstructed M_{jj} signal distribution at various values of Δ_{JES}, along with the fitted probability distribution functions. 83
9.4 The reconstructed M_{jj} background distribution (at $\Delta_{JES} = 0$) along with the fitted probability density function. 84
9.5 Variation of $M_{t\bar{t}}$ with Δ_{JES} in each bin of $M_{t\bar{t}}^{true}$. Events in true bin 1 are in the top right plot, events in true bins 2 and 3 are the in the second row, *etc.* 85
9.6 Denominator in each bin as a function of Δ_{JES}. Bins 1 and 2 are in the first row, 3 and 4 in the second row, *etc.* The points are the values for $\Delta_{JES} = \{-2, -1, 0, 1, 2\} \cdot \sigma_{JES}$ and the black line is the fitted function. 86
9.7 Mean value of Δ_{JES}^{fit} from pseudo-experiments versus Δ_{JES}^{true}. 87
9.8 Mean value of Δ_{JES}^{fit} from pseudo-experiments versus Δ_{JES}^{true} after the correction is applied. 88
9.9 Mean of Δ_{JES}^{fit} pull distribution versus Δ_{JES}^{true} after the correction is applied. 88
9.10 Width of Δ_{JES}^{fit} pull distribution versus Δ_{JES}^{true} after the correction is applied. 89
9.11 The mean uncertainty on Δ_{JES}^{fit} from pseudo-experiments versus Δ_{JES}^{true}. 89

10.1 The distribution of E_T for the leading 4 jets in the data. 94
10.2 The distribution of p_T for the electron or muon in the data. 94
10.3 The distribution of $\not\!\!E_T$ in the data. 94
10.4 The distribution of H_T in the data. 95
10.5 The distribution of $M_{t\bar{t}}$ in the data. 95
10.6 The distribution of M_{jj} in the data. 95

10.7 The fitted M_{jj} distribution in data. 96
10.8 The distribution of $M_{t\bar{t}}$ in the data. The background distribution is normalized to N_{bkg}^{fit} and the $t\bar{t}$ content is the difference between the data and the background. . . . 97
10.9 The detector response matrix used for unfolding the reconstructed $M_{t\bar{t}}$ distribution in data. 97
10.10 The elements of the vector d in the data. 98
10.11 The unfolded background-subtracted $M_{t\bar{t}}$ distribution in data. 98
10.12 $d\sigma/dM_{t\bar{t}}$ measured in 2.7 fb^{-1} of data. The uncertainty does not include the 6% uncertainty due to the luminosity measurement. 99

11.1 The unfolded $M_{t\bar{t}}$ distributions for the RS graviton signal and the SM background. . 102
11.2 The fraction of pseudo-experiments with small p-values for a SM-only hypothesis for events in the BSM model with $\kappa/M_{Pl} = 0.15$. 104
11.3 The expected limit versus the starting bin number for the summation in Equation 11.6. 105
11.4 The A^2 distributions, from Monte Carlo events with the `MRST72` PDF set, for the SM-only and two BSM hypotheses. The value of A^2 in the data is shown by the arrow. 106
11.5 The expected and observed confidence levels for excluding κ/M_{Pl}. 106

Chapter 1

Introduction to Top Quark Physics

1.1 Introduction

Particle physicists seek to understand the nature of the most fundamental particles and the forces which govern their interactions. We search for the origin of mass, the underlying mechanism for the abundance of matter over anti-matter in the universe, and seek hints of a Grand Unified Theory that unites the four fundamental forces as we know them - strong, electromagnetic, weak and gravitational.

This dissertation describes an analysis of the $t\bar{t}$ differential cross section, $d\sigma/dM_{t\bar{t}}$, using the Collider Detector at Fermilab (CDF) II detector. The CDF experiment is positioned in the Tevatron accelerator at the Fermi National Accelerator Laboratory in Batavia, Illinois. The dissertation is organized as follows:

- This chapter motivates the measurement with an introduction to the Standard Model of particle physics with an emphasis on the role of the top quark. I also give a brief overview of the top quark in physics beyond the Standard Model.
- Chapter 2 describes the Tevatron and the CDF II detector.
- Chapter 3 describes the Monte Carlo simulations I use to model the physics processes under study.
- Chapter 4 outlines my selection of $t\bar{t}$ events.
- Chapter 5 explains the method used to calculate the Standard Model backgrounds to $t\bar{t}$ production.
- In Chapter 6 I give an overview of other experimental measurements of the $t\bar{t}$ invariant mass spectrum.
- Chapter 7 explains the analysis methodology in detail.
- In Chapter 8 I discuss the systematic uncertainties associated with this measurement and how I evaluate them. Chapter 9 explains a modification to the analysis which reduces these systematic uncertainties.
- In Chapter 10 I present the results of my measurement.

- Chapter 11 describes how I set limits on new physics beyond the Standard Model.
- I conclude with Chapter 12.

1.2 The Standard Model

The Standard Model (SM) of particle physics has been remarkably successful in describing the strong, electromagnetic and weak interactions. Gravity is not included in the SM (there is no rigorous quantum mechanical description of the force of gravity), but it is extremely weak compared to the other forces and not important at the relevant energy scales probed by particle physics. In the SM all matter[1] is comprised of quarks and leptons, all fermions with spin $\frac{1}{2}$, which can be divided into three generations as in Table 1.1. For each of the fermions in Table 1.1 there exists an anti-

		Name	Symbol	Charge/e	Mass $[MeV/c^2]$
First Generation	Quarks	up	u	$+\frac{2}{3}$	1.5 to 4
		down	d	$-\frac{1}{3}$	4 to 8
	Leptons	electron	e^-	-1	0.51
		electron neutrino	ν_e	0	$< 3 \cdot 10^{-6}$
Second Generation	Quarks	charm	c	$+\frac{2}{3}$	$(1.15 \text{ to } 1.35) \cdot 10^3$
		strange	s	$-\frac{1}{3}$	80 to 130
	Leptons	muon	μ^-	-1	106
		muon neutrino	ν_μ	0	< 0.19
Third Generation	Quarks	top	t	$+\frac{2}{3}$	$(172.6 \pm 1.4) \cdot 10^3$
		bottom	b	$-\frac{1}{3}$	$(4.1 \text{ to } 4.4) \cdot 10^3$
	Leptons	tau	τ^-	-1	1777
		tau neutrino	ν_τ	0	< 18.2

Table 1.1: The quarks and leptons of the Standard Model. [1, 2]

particle with the same mass but opposite charge, denoted for the quarks by the symbol $\overline{q}$ and for the leptons by ℓ^+. Until very recently it was assumed that the neutrinos were massless, but recent measurements of the flux of solar and atmospheric neutrinos provide compelling evidence that the neutrinos are in fact massive [1]. The physics of neutrinos is too complex to explain in detail here. But I should mention that while the anti-particles of the charged fermions are distinct particles, it is not known if the neutrino is its own anti-particle, denoted $\overline{\nu}$. Furthermore, the weak eigenstates of the neutrinos in Table 1.1 are distinct from the mass eigenstates. The three forces of the SM are described by gauge field theories which obey local symmetries and are mediated by field quanta. All of these quanta are spin 1 particles called gauge bosons. The gauge bosons are listed in Table 1.2. The quarks interact via the strong, weak and electromagnetic forces. The leptons do not interact strongly. Because they are charge neutral, the neutrinos can only interact weakly while the charged leptons interact both weakly and electromagnetically. In the next few sections I will describe the

[1] The Standard Model only describes ordinary matter in the universe. Experiments in cosmology tell us that this ordinary matter comprises less than 5% of the known universe, while dark matter, which interacts only weakly in a gravitational manner, comprises about 23% of the known universe. The rest of the universe is made of dark energy, about which we know very little. [1]

Force	Mediator	Charge/e	Mass $[GeV/c^2]$
Strong	gluon (g)	0	0
Electromagnetic	photon (γ)	0	0
Weak	$W^{\pm}$	± 1	80.425 ± 0.038
Weak	Z^0	0	91.1876 ± 0.0021

Table 1.2: The gauge bosons of the Standard Model.

various field theories of the SM in more detail [3]. In these sections I will use units where $\hbar = 1$ and $c = 1$.

1.2.1 Quantum Electrodynamics

Quantum Electrodynamics or QED is the gauge field theory which describes the electromagnetic force. QED is the oldest and best understood theory and the other gauge theories of the Standard Model are based on it to some extent.

The QED Lagrangian is given by:

$$\mathcal{L}_{QED} = \imath\overline{\Psi}(\not{D})\Psi - m\overline{\Psi}\Psi - \frac{1}{4}F_{\mu\nu}F^{\mu\nu}. \tag{1.1}$$

where

$$\mathcal{D}_\mu = \partial_\mu + \imath g_e A_\mu(x) \tag{1.2}$$

and

$$F_{\mu\nu} = \partial_\mu A_\nu - \partial_\nu A_\mu. \tag{1.3}$$

This Lagrangian is invariant under local $U(1)$ transformations:

$$\Psi \rightarrow e^{\imath\alpha(x)}\Psi \tag{1.4}$$

and

$$A_\mu \rightarrow A_\mu - \frac{1}{g_e}\partial_\mu\alpha(x). \tag{1.5}$$

The field A is a gauge field, the quanta of which is the photon. The coupling constant g_e is just the elementary unit of charge $e = \sqrt{4\pi\alpha}$. A mass term for the photon field with the form $\frac{1}{2}MA^\mu A_\mu$ is forbidden by the gauge symmetry, consistent with the massless photons observed experimentally. The global $U(1)$ symmetry of QED leads to conservation of electric charge.

1.2.2 Quantum Chromodynamics

The phenomenology of the strong interactions, as described by Quantum Chromodynamics (QCD), is different from that of electromagnetic interactions in many respects. First, quarks carry an additional quantum number known as color (hence chromodynamics). Color was introduced to explain the observation of, for example, the Δ^{++} baryon, a uuu state. Such a state appears to

violate Fermi-Dirac statistics of spin $\frac{1}{2}$ particles with three fermions occupying the same state. The introduction of three colors - red, blue and green - allows the fermions to each carry an additional quantum number and occupy the same state. Second, quarks are found in colorless confined states of baryons or mesons, never free. The baryons are three quark states with equal mixtures of red, green and blue, while mesons are two quark states of a color and its anti-color. Third, the interactions between quarks are observed to be weak at short distances and stronger at long distances.

The gauge theory of QCD is invariant under transformations of the non-Abelian $SU(3)$ group. The QCD Lagrangian is given by:

$$\mathcal{L}_{QCD} = \imath\overline{\Psi}(\partial\!\!\!/ - \imath g_s A\!\!\!/)\Psi - m\overline{\Psi}\Psi - \frac{1}{2}tr[F_{\mu\nu}F^{\mu\nu}]. \tag{1.6}$$

$\mathcal{L}_{QCD}$ appears very similar to $\mathcal{L}_{QED}$ with the substitution $e \rightarrow g_s = \sqrt{4\pi\alpha_s}$. However, there are important differences. Instead of one gauge field there are now eight gauge fields, corresponding to the eight generators of $SU(3)$, the T^a matrices, where:

$$T^a = \frac{1}{2}\lambda^a \tag{1.7}$$

and the λ matrices are Gell-Mann matrices. The appearance of A_μ in the Lagrangian is shorthand for $A^a_\mu \cdot T^a$. Also, because the Gell-Man matrices do not commute the tensor $F_{\mu\nu}$ is more complicated than the corresponding QED case, Equation 1.3 is modified to:

$$F_{\mu\nu} = (\partial_\mu A^a_\nu - \partial_\nu A^a_\mu - \imath g_s[A_\mu, A_\nu]). \tag{1.8}$$

This additional non-zero commutator term in Equation 1.8 ultimately leads to interactions among the gauge fields. As for the QED case, massive gluons are prohibited by the gauge symmetry.

The gluon-gluon interactions are in turn responsible for the increase in the strength of the QCD coupling at large distances. The variation of $\alpha_s = \frac{g_s^2}{4\pi}$ with energy is shown in Figure 1.1. Note that in units where $\hbar = 1$ and $c = 1$ that energy and distance are simply inversely related. At small length scales (large energies) the quarks and gluons behave as quasi-free particles because the strong coupling is small. [2] In the high energy regime QCD can be described perturbatively. At large separations (low energies), the strong coupling is large and quarks and gluons form bound states. The global $SU(3)$ symmetry of QCD leads to conservation of color, where only colorless bound states are observed. For the purposes of this analysis, I am only interested in the high energy regime where $t\bar{t}$ pairs are produced at the Tevatron.

1.2.3 The Weak Interactions

The pions are the lightest hadrons, composed of u and d quarks, that form a triplet of two charged pions ($\pi^\pm$) and a neutral pion (π^0). The π^0 can decay electromagnetically to two photons, with a lifetime of $(8.4 \pm 0.6) \cdot 10^{-17}$ seconds[1]. The $\pi^\pm$ cannot decay to two photons - charge would not

[2] The scale of QCD is set by $\Lambda_{QCD} = 217^{+25}_{-23}$ MeV [1]. "Small" and "large" energies are small or large with respect to Λ_{QCD}.

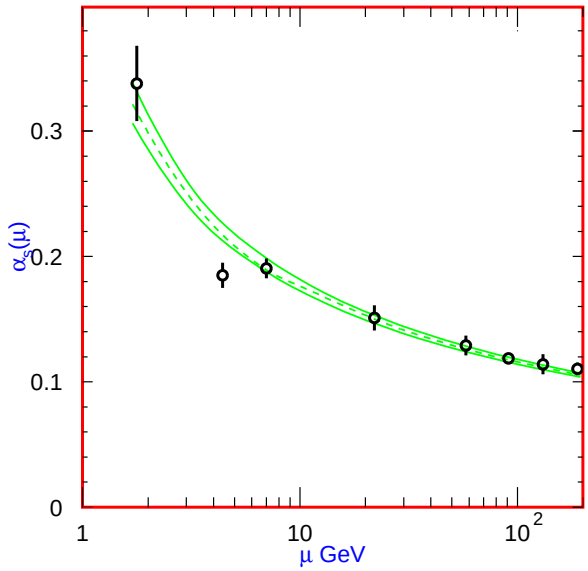

Figure 1.1: The variation of α_s with energy [1].

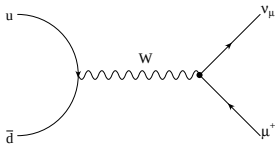

Figure 1.2: The Feynman diagram for the decay of π^+.

be conserved - and are observed to have much longer lifetimes of $(2.6033 \pm 0.0005) \cdot 10^{-8}$ seconds[1]. The longer lifetime of the $\pi^\pm$ with respect to the π^0 indicates that the force responsible for the decay is weaker than the electromagnetic force. This force is creatively known as the weak force.

The weak interaction is quite different from the strong and electromagnetic interactions in that it couples only to left-handed particles. The field Ψ can be decomposed into a left-handed field $\Psi_L = \frac{1}{2}(1-\gamma_5)\Psi$ and a right handed field $\Psi_R = \frac{1}{2}(1+\gamma_5)\Psi$. This $(1-\gamma_5)$ structure is known as the $V-A$ (vector-axial vector) form of the weak current. The weak interaction also couples quarks of different flavors. For example, in the decay $\pi^+ \to \mu^+\nu_\mu$, shown in Figure 1.2 the weak current couples the u to the $\overline{d}$ quark. The weak decay $K^+ \to \mu^+\nu_\mu$ is quite similar with the replacement $\overline{d} \to \overline{s}$. The weak interaction apparently also couples quarks of different generations. Such decays are observed to be suppressed relative to intra-generational decays. For example, the D^0 decays to K^-X, where X is anything, 53% of the time while it decays to K^+X only 3% of the time[1]. These decays $D^0 \to K^\pm\pi^\mp$ are illustrated in Figure 1.3. In the case $D^0 \to K^-\pi^+$ the c quark decays to a s quark (same generation) while for the case $D^0 \to K^+\pi^-$ the c quark decays to a d quark (different generation), accounting for the difference.

There are also weak neutral currents, mediated by the exchange of a Z^0. At low energies,

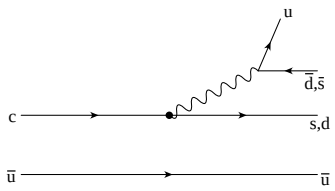

Figure 1.3: The Feynman diagram for the decays $D^0 \to K^{\pm}\pi^{\mp}$.

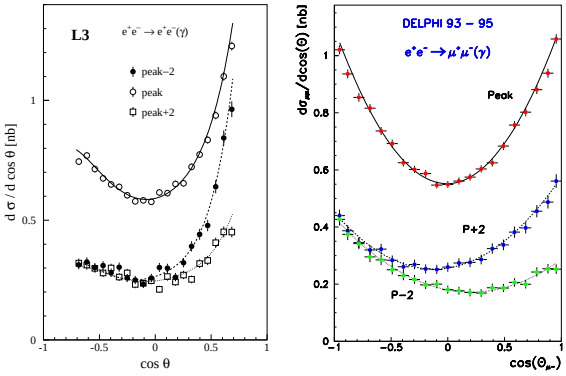

Figure 1.4: The leptonic left-right production cross section asymmetry as measured by two experiments at LEP [5].

much less than M_Z, the electromagnetic current dominates these processes. However, at energies near M_Z these weak neutral current processes become important and the weak neutral current and the electromagnetic currents interfere. This phenomena was extensively studied at the Large Electron-Positron Collider (LEP) and the Stanford Linear Collider (SLC). Figure 1.4 shows the forward-background production asymmetry for the process $e^-e^+ \to \ell^-\ell^+$. A purely electromagnetic process would be totally symmetric, the skewing of the distribution is caused by interference with the Z^0.

Another striking difference between the weak interaction and the electromagnetic or strong interactions is that the field quanta are massive. For the case of QED or QCD the gauge symmetry dictated that the photon and the gluons are massless. Massive gauge bosons suggest that the symmetry of the weak interaction is inexact - that the Lagrangian and the physical vacuum do not obey the same symmetry. This is the case for a spontaneously broken symmetry. Furthermore, the interference of the electromagnetic and neutral current processes suggest a unification of the electromagnetic and weak interactions. This "electroweak" interaction undergoes a spontaneous symmetry breaking to the observed weak interactions and the symmetry of QED.

Spontaneous Symmetry Breaking

The symmetry breaking pattern that is consistent with the observed phenomenology of the weak and electromagnetic interactions is $SU(2)_L \times U(1)_Y \rightarrow U(1)_{EM}$. Before considering this more complex case, I would like to illustrate a spontaneously broken symmetry in two more simple cases.

First I consider a Lagrangian for a doublet of real scalar fields, ϕ:

$$\phi = \begin{pmatrix} \varphi_1 \\ \varphi_2 \end{pmatrix} \tag{1.9}$$

$$\mathcal{L} = \frac{1}{2}(\partial_\mu \phi)^2 - V(\phi) \tag{1.10}$$

with

$$V(\phi) = \frac{1}{2}m^2\phi^2 + \frac{1}{4}\lambda(\phi^2)^2. \tag{1.11}$$

This Lagrangian has a global $SO(2)$ symmetry:

$$\phi = \begin{pmatrix} \varphi_1 \\ \varphi_2 \end{pmatrix} \rightarrow \begin{pmatrix} cos\theta & sin\theta \\ -sin\theta & cos\theta \end{pmatrix} \begin{pmatrix} \varphi_1 \\ \varphi_2 \end{pmatrix}. \tag{1.12}$$

If $m^2 > 0$ the potential $V(\phi)$ is minimized by $\phi_0 = \begin{pmatrix} 0 \\ 0 \end{pmatrix}$. The vacuum remains invariant to $SO(2)$ transformations as in Equation 1.12. However, for the case $m^2 = -\mu^2 < 0$ the potential is minimized by fields that satisfy:

$$\phi_0^2 = \varphi_1^2 + \varphi_2^2 = \mu^2/\lambda = v^2. \tag{1.13}$$

With $m^2 < 0$ the potential has a shape similar to the bottom of a wine bottle. The vacuum now consists of a continuum of states of degenerate energy. By picking a vacuum state:

$$\phi_0 = \begin{pmatrix} 0 \\ v \end{pmatrix} \tag{1.14}$$

and re-defining ϕ in terms of the fields $\pi(x)$ and $\sigma(x)$:

$$\phi_0 = \begin{pmatrix} \pi(x) \\ \sigma(x) + v \end{pmatrix} \tag{1.15}$$

the Lagrangian can we re-written in terms of the new fields π and σ:

$$\mathcal{L} = (\partial_\mu \pi)^2 + (\partial_\mu \sigma)^2 - \mu^2\sigma^2 - \mu\sqrt{\lambda}\pi^2\sigma - \mu\sqrt{\lambda}\sigma^3 - \frac{1}{4}\lambda\pi^4 - \frac{1}{2}\lambda\pi^2\sigma^2 - \frac{1}{4}\lambda\sigma^4 - \frac{1}{4}\mu^4/\lambda \tag{1.16}$$

This Lagrangian is no longer invariant under $SO(2)$ transformations. The symmetry is only apparent in the couplings of the π and σ fields, which depend on only two parameters, μ and λ. Also notice that only the σ field is massive with mass $m_\sigma^2 = 2\mu^2$. The σ field is associated with radial oscillations about the ground state with the massless π field is associated with tangential oscillations. The

massless particle associated with the π is a Goldstone boson.

Goldstone's theorem states that such massless particles result from breaking a continuous symmetry. For a Lagrangian that is symmetric under N-dimensional rotations ($SO(N)$), spontaneous symmetry breaking results in one massive σ field and $N-1$ massless Goldstone bosons – one Goldstone boson for each broken generator.[3] The new Lagrangian is symmetric under $(N-1)$-dimensional rotations ($SO(N-1)$).

Of course the weak interaction is mediated by massive gauge bosons - the $W^{\pm}$ and the Z^0 - while the photon remains massless. According to Goldstone's theorem, this type of particle spectrum can not result from a broken global symmetry. However, the Higgs mechanism for locally invariant gauge theory does supply a phenomenologically viable particle spectrum.

A simple example of the Higgs mechanism can be constructed by modifying the Lagrangian of Equation 1.10, this time for a complex scalar field $\phi(x) = \frac{1}{\sqrt{2}}(\varphi_1 + \imath\varphi_2)$, to be locally gauge invariant:

$$\mathcal{L} = |(\partial_\mu + \imath e A_\mu)\phi|^2 - V(\phi) - \frac{1}{4}F_{\mu\nu}F^{\mu\nu}. \tag{1.17}$$

The Lagrangian is invariant under the $U(1)$ transformations of Equations 1.4 and 1.5. Again when $m^2 = -\mu^2 < 0$ the symmetry will be spontaneously broken. The potential is minimized when:

$$\phi_0^*\phi_0 = \frac{1}{2}\frac{\mu^2}{\lambda} = \frac{v^2}{2}. \tag{1.18}$$

As in the previous example, by picking a vacuum state $\phi_0 = \frac{1}{\sqrt{2}}v$ the field can be redefined in terms of oscillations about this vacuum:

$$\phi(x) = e^{\imath e\theta(x)/v}\frac{1}{\sqrt{2}}(\rho(x) + v). \tag{1.19}$$

With this redefinition the θ field is the massless Goldstone field, corresponding to the one broken generator, and the ρ field has a mass $m_\rho^2 = 2\mu^2$. So far this case is identical to the previous one.

In this case, however, a gauge transformation may be freely made. By choosing $\alpha(x) = -\theta(x)/v$ and transforming according to Equations 1.4 and 1.5 the complex scalar field ϕ becomes:

$$\phi(x) \rightarrow \phi'(x) = \frac{1}{\sqrt{2}}(\rho(x) + v) \tag{1.20}$$

and the gauge field A becomes:

$$A_\mu(x) \rightarrow A'_\mu(x) = A_\mu(x) + \frac{1}{ev}\theta(x). \tag{1.21}$$

The Lagrangian for these transformed fields contains a mass term for both the ρ field and the gauge field A where $m_\rho^2 = 2\mu^2$ as before and $m_A = ev = \frac{e\mu}{\sqrt{\lambda}}$. The freedom of the gauge transformation allows for the undesirable θ field to be gauged away and causes the appearance of a massive gauge boson.

[3] The group $SO(N)$ has $\frac{N(N-1)}{2}$ generators.

Electroweak Unification

The theory of electroweak symmetry breaking with the simplest scalar sector was developed by Glashow, Weinberg and Salam. In this model the initial symmetry is $SU(2)_L \times U(1)$, with four generators and four massless gauge fields.

While in QED and QCD the left- and right-handed fermions transform under the same representation of $U(1)$ and $SU(3)$, respectively, this is not generally required of a gauge theory. To accommodate the observation that the weak interaction couples only to left-handed fermions, the left-handed fermions are grouped into doublets under $SU(2)$. The left- and right-handed fields transform as:

$$\Psi_L \rightarrow exp(\imath g \tau^a \alpha(x)^a + \imath g' Y \beta(x)) \Psi_L \tag{1.22}$$

and

$$\Psi_R \rightarrow exp(\imath g' Y \beta(x)) \Psi_R. \tag{1.23}$$

Where

$$\tau^a = \frac{1}{2}\sigma^a \tag{1.24}$$

are the generators of $SU(2)$ and the σ matrices are the Pauli matrices. The quantity Y is the hyper-charge. The hyper-charge is assigned so that $Q = \tau^3 + \frac{1}{2}Y$ where Q is the electromagnetic charge. The hypercharge assignments of the fermions as summarized in Table 1.3.

$SU(2)$ Representation	Hypercharge
$\begin{pmatrix} u \\ d \end{pmatrix}_L$	$+\frac{1}{6}$
u_R	$+\frac{2}{3}$
d_R	$-\frac{1}{3}$
$\begin{pmatrix} \nu_e \\ e \end{pmatrix}_L$	$-\frac{1}{2}$
ν_R	0
e_R	-1

Table 1.3: Summary of representation of the first generation fermions under $SU(2)$ and their hypercharge. The same holds for the second and third generations.

Then the gauge-invariant Lagrangian is given by:

$$\mathcal{L} = \sum_i \overline{L_i} \imath \gamma^\mu (\partial_\mu - \imath g \tau^a A^a_\mu - \imath g' Y B_\mu) L_i + \sum_j \overline{R_i} \imath \gamma^\mu (\partial_\mu - \imath g' Y B_\mu) R_j - \frac{1}{4} F^A_{\mu\nu} F^{A\mu\nu} - \frac{1}{4} F^B_{\mu\nu} F^{B\mu\nu} \tag{1.25}$$

where

$$L_i = \begin{pmatrix} u \\ d \end{pmatrix}_L, \begin{pmatrix} c \\ s \end{pmatrix}_L, \begin{pmatrix} t \\ b \end{pmatrix}_L, \begin{pmatrix} \nu_e \\ e \end{pmatrix}_L, \begin{pmatrix} \nu_\mu \\ \mu \end{pmatrix}_L, \begin{pmatrix} \nu_\tau \\ \tau \end{pmatrix}_L \tag{1.26}$$

and

$$R_i = u_R, d_R, c_R, s_R, t_R, b_R, \nu_R^e, e, \nu_R^\mu, \mu, \nu_R^\tau, \tau. \tag{1.27}$$

The field tensor $F_{\mu\nu}^A$ contains an additional term, as in Equation 1.8, because the generators of $SU(2)$ do not commute.

At this stage a mass term for the gauge fields is still forbidden by the gauge symmetry. The scalar which breaks the symmetry is a doublet:

$$\phi = \begin{pmatrix} \phi^+ \\ \phi^0 \end{pmatrix} \tag{1.28}$$

where ϕ^+ and ϕ^0 are complex-valued scalar fields. The Lagrangian for the scalar sector has the usual form:

$$\mathcal{L} = (\mathcal{D}_\mu \phi)^\dagger (\mathcal{D}^\mu \phi) - V(\phi^\dagger \phi) \tag{1.29}$$

where $V(\phi^\dagger\phi) = -\frac{1}{2}\mu^2\phi^\dagger\phi + \frac{1}{4}\lambda(\phi^\dagger\phi)^2$ as in Equation 1.11. The symmetry breaking proceeds as before when $\mu^2 > 0$ and the potential is minimized when $\phi^\dagger\phi = \frac{1}{2}\frac{\mu^2}{\lambda} = \frac{1}{2}v$. The field ϕ_0 is chosen as:

$$\phi_0 = \begin{pmatrix} 0 \\ v/\sqrt{2} \end{pmatrix}. \tag{1.30}$$

Now three of the generators are broken: τ^1, τ^2, and the combination $\tau^3 - \frac{1}{2}$. The combination $Q = \tau^3 + \frac{1}{2}Y$ remains unbroken. With the three broken generators come three massless Goldstone bosons. Proceeding as in the previous case for the broken local $U(1)$ symmetry the field ϕ is parameterized as:

$$\phi = \frac{1}{1}(\rho(x) + v) exp(\frac{\imath}{v}[\tau^1\theta_1(x) + \tau^2\theta_2(x) + (\tau^3 - Y)\theta_3(x)]) \begin{pmatrix} 0 \\ 1 \end{pmatrix}. \tag{1.31}$$

The massless θ fields can be gauged away by choosing:

$$\overrightarrow{\alpha} = -\frac{1}{v}(\theta_1, \theta_2, \theta_3) \tag{1.32}$$

and

$$\beta = \frac{1}{v}\theta_3. \tag{1.33}$$

In this gauge the Lagrangian has three massive gauge bosons. The fields A_μ^1 and A_μ^2 have masses $m_{A^{1,2}}^2 = \frac{1}{4}g^2v^2$. The linear combinations:

$$W_\mu^\pm = \frac{1}{\sqrt{2}}(A_\mu^1 \mp \imath A_\mu^2) \tag{1.34}$$

with masses:

$$m_{W^{\pm}}^2 = \frac{1}{4}g^2v^2 \tag{1.35}$$

are identified with the $W^{\pm}$ bosons, the carriers of the weak charged current interaction. The third massive field is:

$$Z_{\mu}^0 = \frac{1}{\sqrt{g^2+g'^2}}(gA_{\mu}^3 - g'B_{\mu}) \tag{1.36}$$

with mass:

$$m_{Z^0}^2 = \frac{1}{4}(g^2+g'^2)v^2 \tag{1.37}$$

and is the Z^0 boson, the carrier of the weak neutral current interaction. The final massless field, the photon field, is orthogonal to the Z^0:

$$A_{\mu} = \frac{1}{\sqrt{g^2+g'^2}}(g'A_{\mu}^3 + gB_{\mu}). \tag{1.38}$$

Equations 1.36 and 1.38 may be written in matrix form as:

$$\begin{pmatrix} Z_{\mu}^0 \\ A_{\mu} \end{pmatrix} = \begin{pmatrix} cos\theta_w & -sin\theta_w \\ sin\theta_w & cos\theta_w \end{pmatrix} \begin{pmatrix} A_{\mu}^3 \\ B_{\mu} \end{pmatrix} \tag{1.39}$$

where:

$$cos\theta_w = \frac{g}{\sqrt{g^2+g'^2}}, sin\theta_w = \frac{g'}{\sqrt{g^2+g'^2}}. \tag{1.40}$$

The angle θ_w is the weak mixing angle. At tree level the masses of the $W^{\pm}$ and Z^0 are related by $m_{W^{\pm}} = m_{Z^0}cos\theta_w$. The covariant derivative of Equation 1.29 may be rewritten in terms of the $W^{\pm}$, Z^0 and A fields as:

$$\mathcal{D}_{\mu} = \partial_{\mu} - \imath\frac{g}{\sqrt{2}}(\tau^+W_{\mu}^+ + \tau^-W_{\mu}^-) - \imath\frac{1}{\sqrt{g^2+g'^2}}(g^2\tau^3 - g'^2Y)Z_{\mu}^0 - \imath\frac{gg'}{\sqrt{g^2+g'^2}}(\tau^3+Y)A_{\mu} \tag{1.41}$$

where $\tau^{\pm} = \tau^1 \pm \imath\tau^2$. The coupling of the photon field of Equation 1.41, $\frac{gg'}{\sqrt{g^2+g'^2}}$, is identical to e.

The Higgs Mechanism

In the Standard Model of the electroweak interactions it is the Higgs field that causes the symmetry breaking - the $\rho(x)$ field in the above section is replaced by the Higgs field $H(x)$- and the Higgs boson is the associated particle. The mass of the Higgs bosons is then $m_H = 2\mu^2 = 2\lambda v^2$. The vacuum expectation value, v, is known to be 247 GeV [1], but the value of λ (the Higgs self-coupling) is not known because the Higgs has not yet been observed.

The Yukawa Interaction

Because the left- and right-handed fermions do not transform under the same representation of $SU(2)$, fermion mass terms of the form $m\overline{\Psi}\Psi = m(\overline{\Psi}_L\Psi_R + \overline{\Psi}_R\Psi_L)$ are forbidden under the electroweak gauge symmetry. Of course, the fermions are in fact massive, with the top quark being very

massive, so the electroweak gauge theory must incorporate massive fermions in some way.

In the Standard Model of the electroweak interactions the mass terms for the fermions arise via the Yukawa interaction, where the Higgs field couples the left and right handed fermions according to:

$$\mathcal{L}_{Yukawa} = -\frac{1}{\sqrt{2}}\lambda_f(H(x)+v)(\overline{F}_R F_L + \overline{F}_L F_R) \tag{1.42}$$

where F is either a lepton or a quark and λ_f is known as the Yukawa coupling for the fermion. Now the mass of each fermion is given by $m_f = \frac{1}{\sqrt{2}}\lambda_f v$. Note that given the known values for v and the fermion masses, that the top quark is the only fermion with the a Yukawa coupling of order one. Why this is so is an open question in the Standard Model - one may suspect that all fermions should have Yukawa couplings of order one. In this way the careful study of the top quark can provide a probe of the physics in the Higgs sector.

The Cabibbo Kobayashi Maskawa (CKM) Mixing Matrix

The Yukawa Lagrangian in Equation 1.42 is gauge invariant under the electroweak gauge transformation but it does not follow from any gauge principle. It is possible to write a Yukawa interaction that is gauge invariant and mixes the generations:

$$\mathcal{L}^{quark}_{Yukawa} = -\frac{1}{\sqrt{2}}\Lambda^u_{ij}(H(x)+v)(\overline{u}^i_R u^i_L + \overline{u}^i_L u^i_R) - \frac{1}{\sqrt{2}}\Lambda^d_{ij}(H(x)+v)(\overline{d}^i_R d^i_L + \overline{d}^i_L d^i_R) \tag{1.43}$$

where u^i is an up-type quark and d^i is a down-type quark. Under the assumption of zero neutrino mass, there is no such Lagrangian for the lepton sector.

The eigen-fields of the Yukawa Lagrangian are fields with definite mass and diagonal mass matrices. These fields are related to the fields of Equation 1.43 by unitary transformations. In other words, there is a change of basis from the eigen-fields of definite mass to the flavor eigen-fields of the weak interaction. The neutral-current interactions remain unchanged by the change of basis. However, now the charged-current interaction couples quarks of different generations, as in the decay $D^0 \to K^+\pi^-$. The mixing is traditionally ascribed to the down-type quarks such that:

$$\begin{pmatrix} d' \\ s' \\ b' \end{pmatrix} = \begin{pmatrix} V_{ud} & V_{us} & V_{ub} \\ V_{cd} & V_{cs} & V_{cb} \\ V_{td} & V_{ts} & V_{tb} \end{pmatrix} \begin{pmatrix} d \\ s \\ b \end{pmatrix} \tag{1.44}$$

where the $d^{i\prime}$ quarks are the flavor eigen-fields. The 3×3 unitary mixing matrix is known as the Cabibbo Kobayashi Maskawa (CKM) matrix. Not all elements of the CKM matrix have been directly probed by experiment. However, the unitarity of the matrix puts constraints on the unmeasured elements (for example, V_{us}). The allowed ranges of the elements, at the 90% confidence level are [1]:

$$\begin{pmatrix} 0.9739 \text{ to } 0.9751 & 0.221 \text{ to } 0.227 & 0.0029 \text{ to } 0.0045 \\ 0.221 \text{ to } 0.227 & 0.9730 \text{ to } 0.9744 & 0.039 \text{ to } 0.044 \\ 0.0048 \text{ to } 0.014 & 0.037 \text{ to } 0.043 & 0.9990 \text{ to } 0.9992 \end{pmatrix}. \tag{1.45}$$

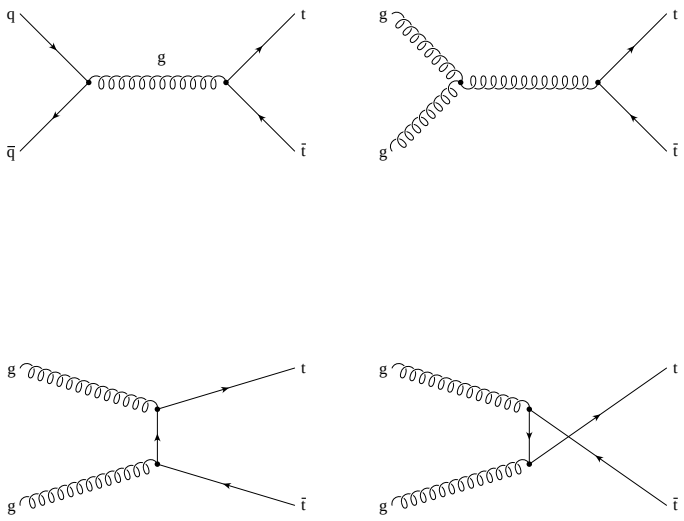

Figure 1.5: The leading order diagrams for $t\bar{t}$ production at the Tevatron.

The matrix is approximately diagonal, as expected by the dominance of same generation charged-current decays over different generation charged-current decays.

1.3 $t\bar{t}$ Production and Decay

1.3.1 $t\bar{t}$ Production at the Tevatron

At the Tevatron protons collide with anti-protons at a center of mass energy of 1.96 TeV. Top quarks are overwhelming produced in strong interactions. The leading order diagrams which contribute to $t\bar{t}$ pair production are shown in Figure 1.5. To quantify the production of $t\bar{t}$ pairs, an experimentalist must measure a quantity that has a sound theoretical interpretation. I will discuss this quantity - the cross section - in detail next.

Collider experiments are fundamentally scattering experiments - two beams of particles collide and then scatter elastically or inelastically, depending on the interaction of the particles. The cross section, which has units of area, measures the "size" of the target. For example, in the hard scattering of two billiard balls the cross section is πR^2, the entire cross sectional area of the balls interact in the collision - nothing happens outside of a radius of R.

The cross section in a $p\overline{p}$ collision is not so intuitive. In a high energy environment such as the Tevatron the protons and anti-protons can scatter inelastically, producing new particles as in $p\overline{p} \to t\bar{t}$, in addition to the elastic scattering $p\overline{p} \to p\overline{p}$. The total inclusive cross section is the sum of all the possible elastic and inelastic scattering processes. The exclusive cross section for a process such as $p\overline{p} \to t\bar{t}$ can be thought of as the probability for a $t\bar{t}$ pair to be produced in a $p\overline{p}$ collision. Figure 1.6 shows the cross sections for many exclusive processes of interest at the Tevatron. So, for example, production of a W is three orders of magnitude more likely than the production of a $t\bar{t}$ pair,

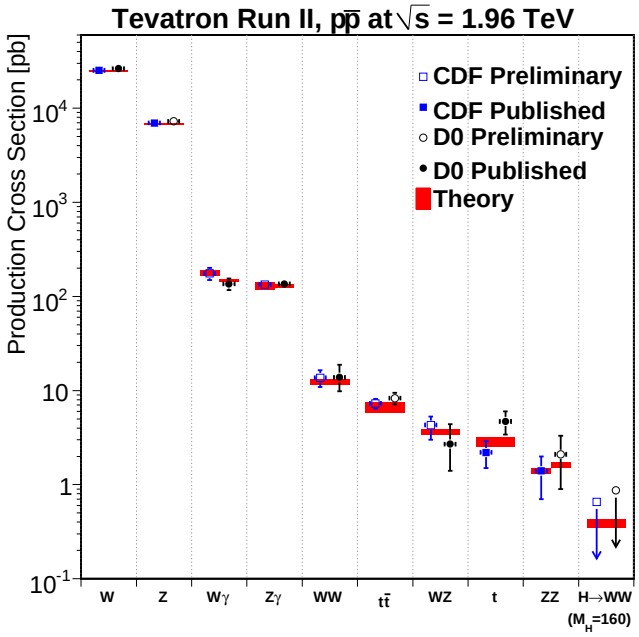

Figure 1.6: The theoretical and measured cross sections for various processes of interest at the Tevatron. Plot courtesy of Mark Neubauer.

while Higgs production, for a Higgs boson mass of 160 GeV/c^2, is about an order of magnitude less likely than $t\bar{t}$ production. I will discuss how the unlikely $t\bar{t}$ events are isolated in detail in Chapter 4.

The cross section for a process is related to the number of events of that type by:

$$\sigma = \frac{N}{\int \mathcal{L} dt} \tag{1.46}$$

where $\int \mathcal{L} dt$ is the integrated luminosity of the experiment.[4] In practice, detectors do not usually offer complete coverage and certain selection cuts are made so the Equation 1.46 is modified to:

$$\sigma = \frac{N}{\varepsilon \int \mathcal{L} dt} \tag{1.47}$$

where ϵ gives the efficiency of the detector and the particle selection cuts that are made. I will return to this factor later in Chapter 4. In high energy experiments cross sections are usually measured in barns. One barn is 10^{-24}cm^2, a unit which is much too large for $t\bar{t}$ production, where the cross section is on the order of picobarns [pb].

[4]Luminosity is measured in 1/[Area] · [Time] so the integrated luminosity has units of 1/[Area].

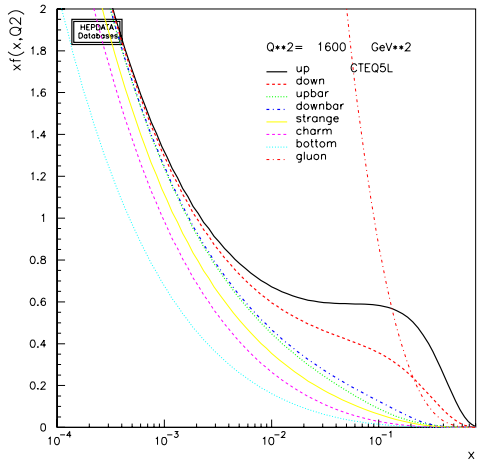

Figure 1.7: The pdf of the proton, as given by the `CTEQ5L` [6] dataset, for a Q^2 of 1600 GeV^2.

The cross section is related in the invariant amplitude for a process, $\mathcal{M}$ by:

$$d\sigma = \frac{\mid \mathcal{M} \mid^2}{F} dQ \tag{1.48}$$

where F is the flux of the particles and dQ is a phase space factor. $\mathcal{M}$ is calculated by following the Feynman rules for the contributing diagrams. I will not reproduce those here. Figure 1.5 gives the diagrams for $q\overline{q} \to t\overline{t}$ and $gg \to t\overline{t}$.

Of course, it is not possible to collide individual quarks and gluons -at the Tevatron protons collide with anti-protons. Because the center of mass energy of the Tevatron is in the regime where the quarks and gluons behave as quasi-free particles, the cross section is factorized into the contribution from $q\overline{q}$ and gg. These cross sections are convoluted with the parton - collectively quarks and gluons are called partons - distribution function (PDF) of the proton and anti-proton. The PDF gives the distribution of the proton's momenta among its constituent particles - the quarks, the gluons which hold them together and the $q\overline{q}$ pairs which pop in and out of the vacuum (the "sea" quarks). PDFs are calculated from the combination of vast amounts of high energy physics data. There are many collaborations dedicated to this endeavor and the exact details are worthy of a dissertation. The PDF of the proton, as calculated by the `CTEQ` collaboration, is given in Figure 1.7. The total cross

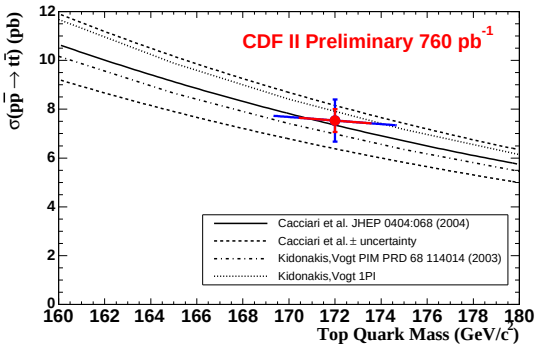

Figure 1.8: The variation of the $t\bar{t}$ production cross section with top mass. The data point indicates the combination of CDF measurements of the top quark mass and $t\bar{t}$ production cross sections.

section for $p\overline{p} \to t\bar{t}$ production is then given by:

$$\sigma_{t\bar{t}} = \sum_{i,j} \int dx_i dx_j f_{i,p}(x_i, Q^2) f_{j,\overline{p}}(x_j, Q^2) \hat{\sigma_{ij}}(ij \to t\bar{t}) \tag{1.49}$$

where x_i is the fraction of momenta carried by the proton, x_j the fraction of the anti-proton, and the hat notation refers to the underlying partonic process.

The total exclusive cross section for $t\bar{t}$ pair production depends on the mass of the top quarks. The reason for this is simple - a heavier top is harder to produce. For a top quark with a mass of 175 GeV/c^2 the theoretical $t\bar{t}$ cross section is about 6.7 pb - with some variation depending on the PDF set and renormalization scale used [7]. The dependence of the cross section with mass is illustrated in Figure 1.8. The cross section changes by ± 1 pb for each ± 5 GeV/c^2 change in the top quark mass.

A differential cross section, such as $d\sigma/dM_{t\bar{t}}$, contains additional important information. The theoretical interpretation is obvious from Equation 1.48. All of phase space is integrated over, except for a region of invariant mass, $dM_{t\bar{t}}$. The experimental interpretation of Equation 1.47 is modified to:

$$\frac{d\sigma^i}{dM_{t\bar{t}}} = \frac{N^i}{\varepsilon^i \Delta^i_{M_{t\bar{t}}} \int \mathcal{L} dt} \tag{1.50}$$

where the superscript i indicates a bin of the $M_{t\bar{t}}$ distribution. If there was a massive particle X that strongly coupled to the top quark it would be seen as a resonance or distortion in $d\sigma/dM_{t\bar{t}}$ in the region of M_X. The exact nature of the resonance or distortion would depend on the mass of particle, its width, coupling to the top, and any interference with the SM. It is possible to imagine a scenario where such a process would not change the integrated cross section to an appreciable degree, only the differential cross section. In this way differential distributions provide a unique window to non-Standard Model physics.

1.3.2 Top Decay

The extremely heavy top quark has very short lifetime of approximately 10^{-24} seconds, which is short enough that it decays before it hadronizes [1]. The top quark is unique in this respect. As free quarks are never found, the top quark supplies the only probe of the behavior of bare quarks.

The top quark decay is dominated by the decay $t \to Wb$ as the CKM element V_{tb} is nearly 1. The b quark will then hadronize to a B meson or baryon. The B hadrons will continue to decay, via a $b \to Xc$ or $b \to Xu$ process. The former decay is preferred, according to CKM matrix. However, V_{cb} is not a diagonal element so the b decay is somewhat suppressed. This contributes to the relatively long lifetimes of the B hadrons, most are approximately 1.5 ps [1]. This characteristic of the B hadrons is exploited to identify them, as I will discuss in detail in Chapter 4. The W daughter of the top decays to either a lepton and its associated anti-neutrino or a qq' pair. $t\bar{t}$ events are classified according to the decays of the two $W^{\pm}$ bosons. When both $W^{\pm}$ bosons decay hadronically the event is an "all jet" event. When both $W^{\pm}$ bosons decay leptonically the event is a "dilepton" event. When one $W^{\pm}$ decays leptonically and the other hardonically the event is a "lepton plus jets" event. I will return to these various classes of events in Chapter 4.

1.4 The Top Quark in Physics Beyond the Standard Model

The Standard Model of electroweak symmetry breaking succeeds in explaining the masses of the $W^{\pm}$ and Z^0 bosons and the generation of fermion masses, but suffers many drawbacks. First, the Higgs sector and the required non-zero vacuum expectation value which breaks the symmetry do not arise from first principles. Second, a great deal of fine tuning is required to maintain the renormalizability of the field theory and stabilize the Higgs boson mass. Third, the theory does not explain in any fundamental way the strength of the Yukawa couplings between the Higgs boson and the fermions - recall that the Yukawa interaction itself does not arise from any gauge principle but rather only obeys the gauge symmetry. Finally, while the Standard Model prefers a light Higgs boson [8], it remains undiscovered. The current best fit Higgs mass, using a global fit to all of the precision electroweak data, is 87^{+36}_{-27} GeV/c^2, as shown in Figure 1.9, which is well within the reach of current experiments.

Because the top quark is the only (known) fermion with a mass near the electroweak scale, it plays a special role in many theories of physics beyond the Standard Model (BSM). A large variety of models exist where the top plays either a direct or indirect role in the generation of the masses of the $W^{\pm}$, Z, and fermions [9]. Here I will only focus on a subset of these models that have been the focus of the most experimental scrutiny.

Just as the symmetry group $SU(2)_L \times U(1)$ is broken to the $U(1)$ symmetry of the QED, leading to the generation of massive gauge bosons, many BSM theories propose that the SM is an effective low energy theory that results from the breaking of extended gauge groups. This leads to additional massive gauge bosons - and additional scalar Higgs bosons. Many of these theories predict a Z^0-like boson called the Z' [10]. For example, in topcolor-assisted technicolor models an additional $U(1)$ group couples preferentially to the third generation quarks. In these technicolor models, the Higgs

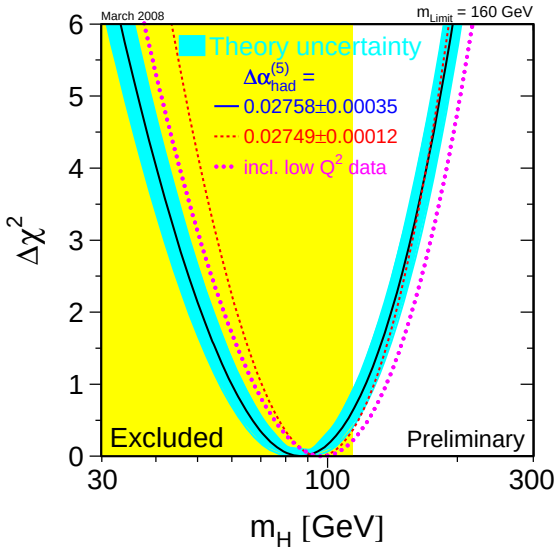

Figure 1.9: The best fit Higgs mass from a global fit to precision electroweak data, assuming the SM theory [8].

doublet which breaks the symmetry is not an elementary scalar field, but rather a condensate of $t\bar{t}$ pairs that dynamically breaks the electroweak symmetry [11]. Regardless of the specifics of the model, a Z' which couples strongly to the top quark will result in a resonance in the invariant mass spectrum of the $t\bar{t}$ pairs. A search in the channel $Z' \to t\bar{t}$ is most sensitive to those Z' bosons which do not have large branching ratios to leptons. Such a Z' is "leptophobic" and is seen as a narrow resonance in the $t\bar{t}$ invariant mass spectrum.

In other models with $t\bar{t}$ condensation the third generation of quarks participates in a new strong gauge interaction [12]. The new extended gauge group is $U(1) \times SU(2)_L \times SU(3)_1 \times SU(3)_2$. The symmetry is broken to the SM group $U(1) \times SU(2)_L \times SU(3)$, leaving a color octet of massive gauge bosons called "colorons." These colorons couple preferentially to top quarks. In contrast to the narrow resonances indicative of a leptophobic Z', the colorons interfere with the SM gluons and produce broad distortions to the invariant mass spectrum of $t\bar{t}$ pairs. Another theory with a new strong coupling is the "chiral color" model [13]. In this model the extended gauge group is $U(1) \times SU(2)_L \times SU(3)_R \times SU(3)_L$. When broken to the SM QCD interaction, a color octet of massive bosons called "axigluons" result. While both colorons and axigluons are spin-1 color octet particles, they have different parity quantum numbers. The processes would be most easily distinguished by studying the forward-background asymmetry in $t\bar{t}$ production [14].

In the ultimate description of the SM as a low-energy effective field theory all of the forces of the SM are unified in a single large gauge group where the strong, electromagnetic and weak forces are indistinguishable. If gravity is to be included, the unification occurs at the Planck scale, M_{Pl},

of $2 \cdot 10^{18}$ GeV. A persistent theoretical puzzle is the large gap between M_{Pl} and the scale of electroweak symmetry breaking - this is the so-called "hierarchy puzzle." Various theories introduce extra dimensions to space-time to solve the hierarchy problem. In the Randall-Sundrum (RS) model a single warped extra dimension accounts for the large hierarchy [15]. In the original RS model the SM fields are confined to a single brane while Kaluza-Klein (KK) gravitons (the quanta of gravity) propagate in the bulk space. These gravitons would be seen in the $t\bar{t}$ invariant mass spectrum as a series of resonances. In extended RS models the SM fields also propagate into the bulk space. In such models the KK excitation of the gluon would couple strongly to top quarks and result in resonances in the $t\bar{t}$ invariant mass spectrum near the mass of the KK-gluon [16].

In summary, a large class of BSM theories predict distortions to the $t\bar{t}$ invariant mass spectrum. The distortions may be narrow resonances such as a Z' or a broad interference as for a coloron. The goal of this analysis is to remain as model-independent as possible when analyzing the $M_{t\bar{t}}$ spectrum. In this way I maintain sensitivity to the many BSM effects which are possible.

Chapter 2

The Fermilab Tevatron and the CDF II Detector

2.1 Introduction

The Fermi National Accelerator Laboratory (FNAL), or Fermilab, has been the home of several great discoveries in particle physics - the bottom quark was discovered at Fermilab in 1977, the top quark in 1994-1995 and the τ neutrino in 2000. Fermilab is home to the Tevatron and the two large collaborations devoted to studying $p\overline{p}$ collisions, the Collider Detector at Fermilab (CDF) and DØ collaborations; two neutrino experiments, MiniBooNE and Minos; and is home for many theoretical physicists. In this chapter I will focus on the Tevatron and the CDF II detector. These are huge and complicated machines that cannot be fully described in a few pages. This chapter is meant to be an overview that highlights the important components for this analysis.

2.2 The Tevatron

The protons and anti-protons are produced and accelerated to their final energies of 980 GeV by a series of accelerators [17]. Figure 2.1 is a diagram of the Fermilab accelerator chain. Proton production begins in the Cockcroft-Walton pre-acclerator. Hydrogen gas is ionized to create H^- ions that are accelerated to an energy of 750 keV. The ions then pass onto the Linac, a linear accelerator about 500 feet long which accelerates the ions to an energy of 400 MeV. The electrons are stripped from the ions by passing the hydrogen through a carbon foil and the resulting protons enter the Booster for further accelerator. The Booster accelerates the protons to 8 GeV before passing them onto the Main Injector.

The Main Injector performs many functions. First, it accelerates protons to 120 GeV and sends them to the Anti-proton Source for anti-proton production. Anti-protons are produced by colliding protons with a nickel target. Anti-protons are collected from the resulting spray of particles by using a lithium lens. It takes about 10^5 protons to make an anti-proton. The anti-protons are sent to the Accumulator for temporary storage before passing to the Recycler Ring in the Main Injector. Once enough anti-protons have been produced they are accelerated to 150 GeV before injection to the Tevatron.

The Tevatron is a superconducing synchrotron accelerator. Protons and anti-protons are injected in bunches, with 36 bunches of about 10^{12} protons each and 36 bunches of about 10^{11} anti-protons in the 4 mile Tevatron ring. The protons and anti-protons are accelerated to 980 GeV by the Tevatron,

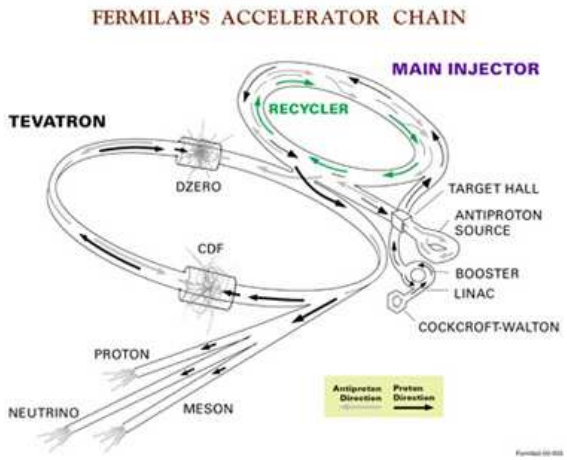

Figure 2.1: The Fermilab Tevatron accelerator chain.

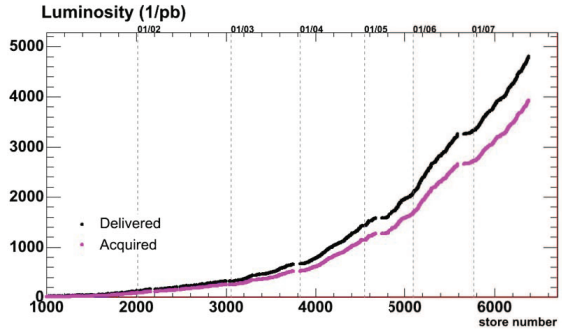

Figure 2.2: The integrated luminosity delivered and recorded by the CDF II detector.

producing collisions with a center of mass energy of 1.96 TeV. The beams collide once every 396 ns at two interactions points - the CDF and DØ detectors. The Tevatron is the only proton-anti-proton collider in the world today. Soon the Tevatron will loose the distinction of also being the world's highest energy collider to the LHC, which will collide protons with protons at a center of mass energy of 14 TeV. Due to many improvements that were made to anti-proton production and storage in Run II of the Tevatron, record-setting instantaneous luminosities of $3 \cdot 10^{32} cm^{-2} s^{-1}$ have been achieved. The total integrated luminosity delivered to, and recorded by, CDF is shown in Figure 2.2. This analysis uses 2.7 fb^{-1} of integrated luminosity, collected between March 2002 and April 2008.

2.3 CDF II Detector

The CDF II Detector is actually a series of many subdetectors that work together to study the $p\overline{p}$ collisions. All together the CDF II detector is about three stories tall and weighs nearly 5000 tons. At the core of the detector is a 1.4 T superconducing solenoid. A precision tracking system

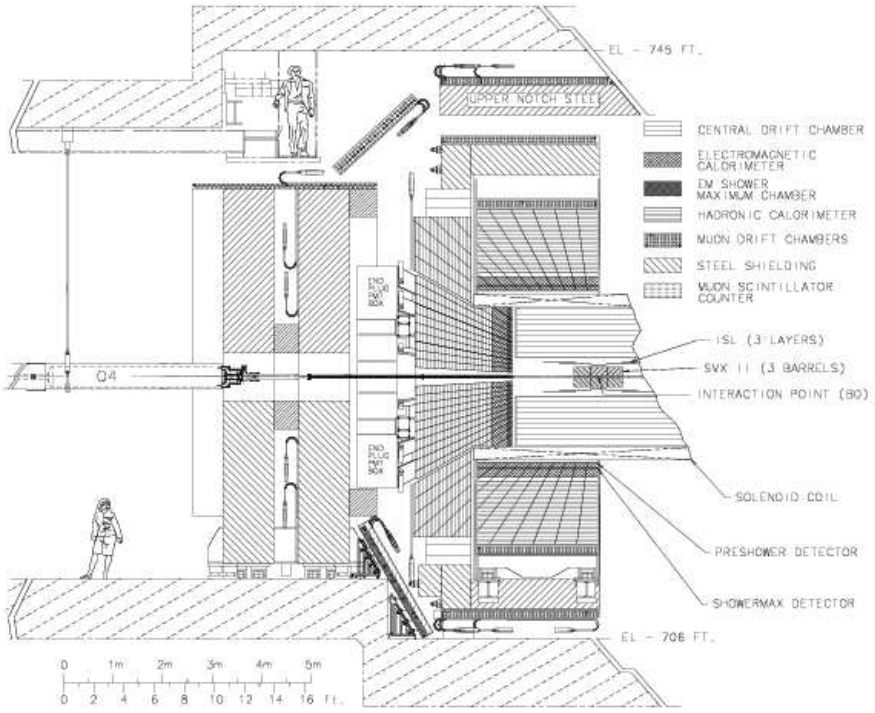

Figure 2.3: An elevation view of the CDF II detector.

is immersed in the magnetic field, providing detailed tracking information for charged particles. Outside the magnetic field a series of calorimeters measure the energies of electrons, photons and hadrons. At the outermost edges of the detector a series of muon detectors are used for muon identification. An elevation view of the CDF II detector is given in Figure 2.3.

The CDF II detector is nearly azimuthally and forward-background symmetric. It is described by a cylindrical coordinate system (z,ϕ,η). The z axis points in the direction of the proton beam. The ϕ angle is the azimuthal angle and the variable η, the pseudorapidity, is related by the polar angle θ by:

$$\eta = -ln(tan(\frac{\theta}{2})) \tag{2.1}$$

For highly relativistic particles η is approximately equal to the rapidity, $Y = tanh^{-1}(p_z/E)$, and they are identical for massless particles. Pseudorapidity transforms linearly under Lorentz boosts - in other words, differences in η are invariant. The CDF II detector is fully described in Reference [18]. I will highlight the most important subsystems for the analysis here.

2.3.1 Tracking Systems

Tracking detectors are key for identifying the charge and momentum of particles created in the $p\overline{p}$ collisions. The tracking detectors, consisting of silicon detectors closest to the beam and a drift chamber immediately outside the silicon detectors, are immersed in the solenoid field. The

solenoid field, B, is a uniform 1.4 T field which runs parallel to the beamline in the z direction. Charged particles traveling in the magnetic field follow helical paths where the curvature of the helix, $C = 1/(2R)$ where R is the radius, is related to the transverse momentum, p_T, of the particle by:

$$p_T = \frac{0.3B}{2C} \tag{2.2}$$

The high precision silicon detectors located closest to the beam allow for the reconstruction of secondary vertices used in the identification of heavy flavor quarks. I use this secondary vertex reconstruction to identify b quarks from top decays in this analysis.

The innermost tracking detectors are silicon strip detectors. The Silicon Vertex Detector (SVX) covers the range $|\eta| < 2.0$ and 1.5 cm $< r <$ 10.7 cm. The strips are arranged in a barrel geometry with 5 layers of strip detectors. The strips are double-sided where one strip provides axial measurements parallel to the beamline while the other side provides stereo measurements. For three of the five layers the stereo layer is at 90° to the beamline while for the remaining two layers have a small stereo angle if 1.5°. The stereo information allows for the extrapolation of the z position of tracks. The Intermediate Silicon Layers (ISL) provide additional coverage out to a radius of 28 cm. The ISL consists of three double-sided layers of strip detectors, where one side provides axial information and other side has a small stereo angle. Two of these layers are located at high η to provide tracking in the forward region. There is an additional layer of silicon strips placed directly on the beamline, called L00. These detectors are specially designed to withstand the high radiation on the beamline.

The silicon detectors are semiconductor devices that detect charged particles when they ionize the detector medium to create electron/hole pairs. The electrons and holes drift to opposite electrodes, inducing a signal. In order to detect the signal over the background of free charge carriers in pure silicon, the silicon is doped to create a charge depletion region that is further enchanced by the application of a reversed bias voltage. The CDF II silicon detectors consist of lightly doped n-type silicon sandwiched between a highly doped n-type electrode and lightly-doped p-region. Silicon detectors achieve excellent spatial resolution because the ionization energy required to induce a signal is relatively low - the spatial resolution of the CDF silicon detectors is about 15 μm [28]. Silicon detectors can also be read-out rapidly, allowing the tracking information to be used in trigger decision. I discuss the CDF II trigger system in detail in Section 2.3.5.

The Central Outer Tracker (COT) is an open-cell drift chamber which provides additional tracking information in the region $|\eta| < 1.0$ and 40 cm $< r <$ 137 cm . The COT consists of gold-plated tungsten sense wires arranged in eight superlayers, which alternate between axial and stereo orientations, where the stereo angle is 2°. The superlayers provide up to 96 measurements of the charged particle position. The superlayers are enclosed in a chamber which is filled with a 50/50 mixture of argon and ethane gasses. An electric field is created by a voltage applied to sense (anode) wires and cathode field panels. Charged particles passing through the detector ionize the gas. The freed electrons create an avalanche of charges when they encounter the high electric field near the sense wires, which is registered as a signal by the wire. The time between the collision and the arrival of the electrons at the wire, the drift time, is converted to a distance of closest approach to the wire. The path of the charged particle in three dimensions is reconstructed from the distance of

closest approach to the axial and stereo wires. The transverse spatial resolution of the COT is approximately 180 μm, with a transverse momentum resolution of $\sigma_{p_T}/p_T^2 = 0.0017$ [GeV/c]$^{-1}$ [28].

2.3.2 Calorimetry

Calorimeters, which measure the transverse energy of jets, electrons and photons, lie outside the solenoid. The calorimeters are also used to calculate the missing transverse momentum associated with neutrinos, which is called the "missing E_T," or $\not\!\!E_T$, because it is derived from calorimeter information. The electromagnetic (EM) calorimeters are the innermost calorimeters. The EM calorimeter is a lead-scintillator sandwich, which is divided between a central ($|\eta| < 1.1$) and forward ($1.1 < |\eta| < 3.6$) region. In this analysis I use only electrons identified with the Central EM (CEM) calorimeter. The CEM is supplemented with a shower maximum detector (CES) which measures transverse shower profiles for finer position resolution. The hadronic (HAD) calorimeter, immediately outside the EM calorimeter, is a steel-scintillator sandwich with a central (CHA) and a forward region. The calorimeters are segmented into towers, where the segmentation varies with position. In the central region each tower covers 0.11 in η and 15° in ϕ.

The EM and HAD calorimeters function using the same basic principle. The lead or steel functions as an absorber and radiator which alternates with layers of scintillator. Electromagnetic or hadronic cascades from the interaction of particles with the absorber material cause the scintillating material to emit light which is collected and measured by photomultiplier tubes. The resolution of the CEM is $14\%/\sqrt{E_T}$ while the CHA has a resolution of $50\%/\sqrt{E}$ [28].

2.3.3 Muon Systems

Muons are characterized by the fact that they are nearly minimum ionizing particles which pass through the detector without losing substantial energy in the calorimeters. Muons are detected by a series of drift chambers which lie along the outer edges of the detector, outside the calorimetry. The detectors are comprised of layers of single wire drift chambers. Muon candidates are detected by the same mechanism described above for charged particle tracking in the COT. The charged candidates ionize a 50/50 mixture of argon and ethane gasses. The ionization electrons move to the sense wire, creating an avalanche that is detected by the wire. The drift time is converted to a drift velocity, giving the distance of closest approach of the muon candidates to the wire.

The Central Muon Detector (CMU) covers the region $|\eta| < 0.6$ immediately outside the hadronic calorimeter. It consists of 4 layers of single wire drift chambers. The CMU provides measurements in the $r - \phi$ plane as well as in the z direction. The Central Muon Upgrade (CMP) is located in the same η region as the CMU, behind additional steel shielding. Like the CMU, the CMP consists of 4 layers of single wire drift chambers. However the CMP does not provide z position measurements. Muon candidates with hits in both the CMU and CMP are called CMUP muons and have lower rates of misidentification than muon candidates without hits in both the CMU and CMP. The Central Muon Extension (CMX) covers the region $0.6 < |\eta| < 1.0$. The CMX consists of between 4 and 8 layers of single wire drift chambers and also provides z position measurements of muon candidates. Muons candidates are identified by matching the track segments in the chambers to tracks in the

COT. Candidates must also deposit energy in the calorimeters that is consistent with a minimum ionizing particle.

2.3.4 Luminosity Measurement

Luminosity is measured using two Cherenkov Luminosity Counters (CLC) positioned at small angles to the beamline in both the proton and anti-proton directions. The CLC detectors are thin conical counters consisting of three concentric layers around the beam pipe filled with isobutane gas. The CLC counters detect the Cherenkov radiation light emitted by the charged particles from the collision as they pass through the isobutane gas.[1] The light is collected and then registered by a photomultiplier tube.

The CLC counters measure the average number of inelastic $p\overline{p}$ interactions per bunch crossing, μ. The instantaneous luminosity, $\mathcal{L}$ is given by:

$$\mathcal{L} = \frac{\mu \cdot f}{\sigma_{in}} \tag{2.3}$$

where f is the rate of $p\overline{p}$ bunch crossings and σ_{in} is the total inelastic $p\overline{p}$ cross section. There is a 6% uncertainty associated with the luminosity measurement, with almost equal contributions coming from the uncertainty associated with the acceptance and operation of the CLC counters and the calculation of the inelastic $p\overline{p}$ cross section.

2.3.5 Trigger

CDF cannot record events at the 2.5 MHz collision rate. Furthermore, many events are uninteresting and not worth recording at a cost of 250 kB per event. CDF uses a three level trigger system which filters events to a rate of about 100 Hz for permanent storage. The system is pipelined to process events in real time with minimal deadtime.

The level 1 trigger consists of dedicated hardware which receives information from the calorimeters, muon detector system and the COT. The level 1 buffer is 14 collisions deep with a decision time of 5.5 μs. After the level 1 decision, the event rate is about 20 kHz. The level 2 trigger again consists of dedicated hardware. The level 2 system receives information from level 1, as well as silicon tracking information and input from the shower maximum detector. Level 2 consists of 4 buffers with a decision time of about 30 μs. After passing level 2, the event rate is about 1 kHz. The level 3 trigger consists of dedicated CPUs which perform a simplified version of the offline event reconstruction. This final stage of the trigger reduces the event rate to about 100 Hz. A schematic of the trigger system is shown in Figure 2.4.

The data used in this analysis were collected using a trigger which looks for a single high p_T electron or muon. The trigger is described in more detail in Chapter 4.

[1] Cherenkov radiation is emitted when a charged particle passes through a medium at a speed greater than the speed of light in that medium.

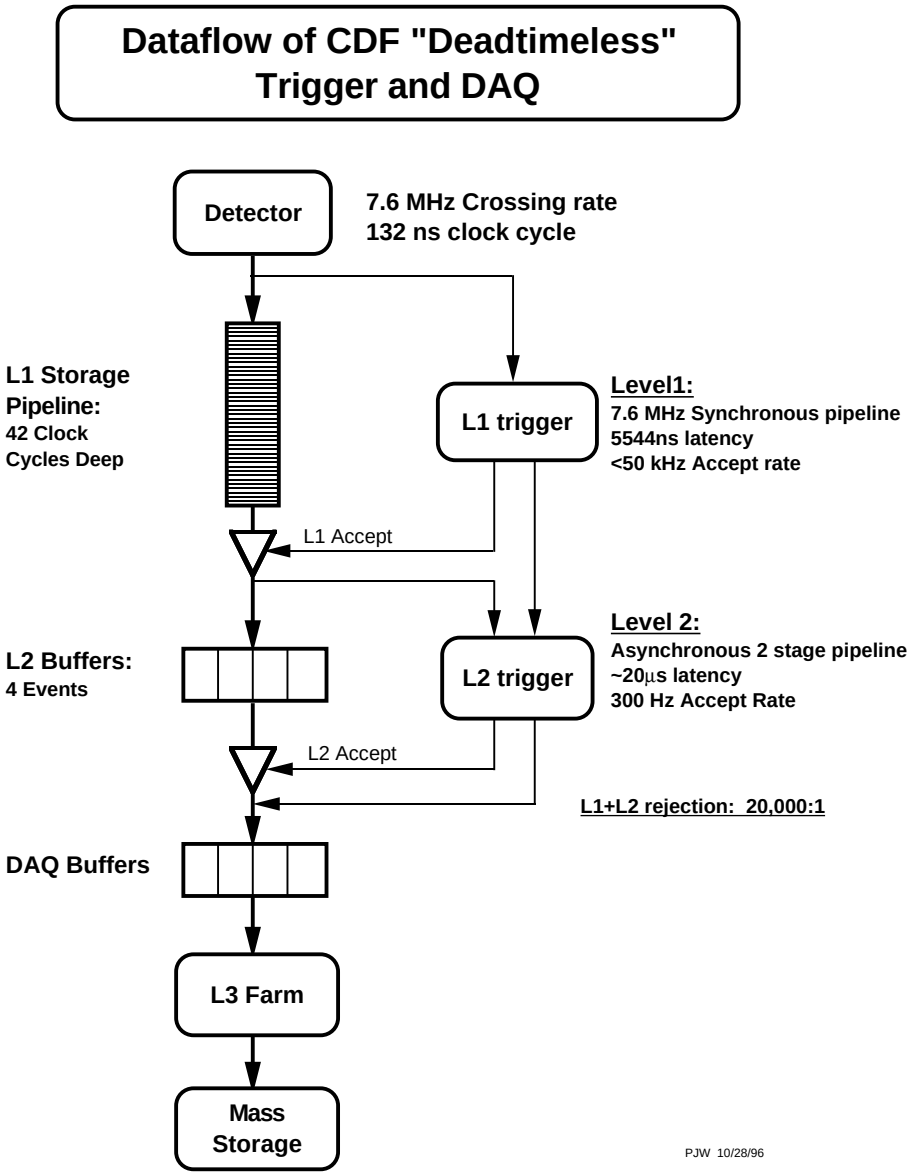

Figure 2.4: A schematic of the CDF II trigger system. The clock cycle shown is 132 ns, but the Tevatron currently operates at 396 ns.

Chapter 3

Monte Carlo Models for Signal and Background

3.1 Introduction

The importance of Monte Carlo event generation and detector simulation in high energy physics experiment cannot be overstated. As soon as QCD reaches a non-perturbative regime - for example, when quarks hadronize into jets - analytical calculations become impossible. Leptons also emit bremsstrauhlung radiation, which can become tedious to calculate. Furthermore, the response of the detector to particles cannot be calculated and must be modeled by simulation programs. In this chapter I will describe the various Monte Carlo event generators and detector simulations programs used in this analysis.

3.2 Monte Carlo Event Generation

All of the Monte Carlo event generators used in this analysis are leading-order generators. The problem of event generation can be factorized into several pieces [20, 19]. First there is the generation of the hard process, for example $q\overline{q} \to t\bar{t}$. These processes can be calculated exactly to lowest order in perturbation theory because QCD is still in the regime where the quarks and gluons can be treated as quasi-free particles. Second there is the emission of initial and final state radiation in the form of extra gluons radiated by the incoming or outgoing partons. Such processes depend largely on the momentum transfer of the process and can be treated probabilistically. Third there is the decay of heavy objects in the event, such as heavy quarks and the electroweak bosons. Whether or not this happens on a time scale shorter than that for QCD hadronization determines the complexity of the process. Finally there is the hadronization of the final state partons. Here perturbative QCD is of no help so only phenomological models apply. The exact details of the model for hadronization vary depending upon the Monte Carlo generator used. I will not go into the details here, but only point out that comparing the output of different models is an important systematic check for any analysis which relies upon Monte Carlo event generation. Some Monte Carlo generators are capable of the simulation of the hard process, initial and final state radiation, heavy object decay and hadronization. Other Monte Carlo programs generate only the hard process - the "matrix-element" generators - and need other programs to perform the remaining steps.

3.2.1 Signal Event Generation

The primary $t\bar{t}$ event sample is generated with the PYTHIA program [19], version 6.216. The CTEQ5L parton distribution function [6] is used for the incoming protons and anti-protons. The PYTHIA implementation produces stable heavy (b and c) quarks which are decayed with EvtGen [23]. When I refer to PYTHIA this implies that EvtGen and CTEQ5L have been used for the heavy quark decay and parton distribution functions, respectively. An alternative sample is generated with the HERWIG program [20], version 6.510, in place of PYTHIA for systematic studies of the effect of the hadronization model. This sample also uses EvtGen and CTEQ5L parton distribution functions.

3.2.2 Background Event Generation

The Monte Carlo programs used to model various background processes are summarized in Table 3.1. Both ALPGEN [22] and MadEvent [21] are leading order matrix element generators. They are used to generate the hard process, which is then passed to PYTHIA for decay and hadronization. The ALPGEN version used is 2.10′, with PYTHIA version 6.325 for decay and hadronization. The MadEvent version used is version 4.

Process	Monte Carlo Event Generator
Diboson	PYTHIA
W+jets	ALPGEN+PYTHIA
Z+jets	ALPGEN+PYTHIA
Single top	MadEvent+PYTHIA

Table 3.1: Summary of Monte Carlo programs used to generate events for different classes of background events.

The proper generation of the W and Z plus jets background events requires extra care. The following samples are generated with ALPGEN:

- $W + Np$, N=0,1,2,3,4
- $Wb\bar{b} + Np$, N=0,1,2
- $Wc\bar{c} + Np$, N=0,1,2
- $Wc + Np$, N=0,1,2,3

where Np refers to the number of additional partons in the final state.

There is an overlap in phase space between events that are generated as, for example, $W + Np$ and radiate an extra jet with hadronization to produce $N + 1$ jets and events that are generated as $W + (N + 1)p$. The same holds for events which hadronize with 2 extra jets and events generated as $W + (N + 2)p$, *etc.* This overlap is removed during generation by requiring that every parton is matched to a jet and that the number of jets equals the number of partons. Events with the highest generated parton multiplicites are allowed to have extra jets. There is a second overlap in heavy flavor content which must also be removed. For example the 2 partons in a $W + 2p$ event may be $b\bar{b}$,

which overlaps with the $Wb\bar{b}$ sample. This overlap is removed after event generation by requiring that events have the proper heavy flavor content. To model the W or Z plus jets data, the samples are combined according to a luminosity weighted average. The integrated luminosity of a sample i is given by n^i_{gen}/σ^i_{Gen} where σ^i_{Gen} is the cross section generated by `ALPGEN` and n^i_{gen} is the number of events generated for sample i. Each sample is weighted by σ^i_{Gen}/n^i_{gen} to give the same luminosity for each and then added together.

3.3 CDF Detector Simulation

The CDF detector simulation is described in [24]. The simulation uses the `GARFIELD` [26] program for modeling of the COT, the `GFLASH` program [27] for modeling of the calorimeters and the `GEANT3` program [25] for modeling of the remaining detector subsystems. The simulation is run-dependent - it takes into account those periods (run numbers of data) where certain subsystems of the detector were not used and the acceptance of the silicon detectors changed. After detector simulation the events are passed through the same offline software as real data.

Chapter 4

$t\bar{t}$ Event Selection

4.1 Introduction

As I discussed in Chapter 1 the top quark decays via $t \to W^+ b$ nearly 100% of the time. For $t\bar{t}$ pairs, then, the daughters are $W^+ b W^- \bar{b}$. The $W^\pm$ decays to electrons, muons and taus with a branching ratio of $10.68 \pm 0.12\%$ (for each lepton flavor) and decays hadronically with a branching ratio of $67.96 \pm 0.35\%$ [1]. The possible final states of the two W bosons are summarized in Table 4.1.

	$e^\pm\nu$	$\mu^\pm\nu$	$\tau^\pm\nu$	hadrons
$e^\mp\nu$	1.14	1.14	1.14	7.25
$\mu^\mp\nu$	1.14	1.14	1.14	7.25
$\tau^\mp\nu$	1.14	1.14	1.14	7.25
hadrons	7.25	7.25	7.25	46.18

Table 4.1: Possible final states of W^+ and W^- $t\bar{t}$ daughters. The numbers are the percentage of the decays with that final state.

The final state of the $t\bar{t}$ decay always has at least two jets, from the hadronization of the the b and $\bar{b}$ quarks. Depending on the decays of the W bosons, there are between zero and four additional jets. The number of leptons in the final state varies from zero in the all-hadronic case to two leptons and their associated neutrinos in the dilepton case. Each decay channel has distinct physics backgrounds with the all-hadronic channel having very large SM backgrounds from generic QCD jet production and the dilepton channel having small SM backgrounds. At the same time, the all-hadronic decay is the most likely while the dilepton decay is the least likely. The compromise, where one W decays leptonically and other decays hadronically, with final state $b\bar{b}\ell\overline{\nu}_\ell q\overline{q}'$ is the "lepton+jets" channel. The final state consists of a lepton, neutrino and four jets, two of which are b-jets. The lepton+jets channel has long been the "golden channel" for $t\bar{t}$ physics, and most precision results come from this channel. As is customary, I do not consider events where the lepton is a τ because τ-leptons are difficult objects experimentally, although there is some small acceptance for τ decays to electrons and muons. For the remainder of this dissertation the symbol ℓ indicates only the charged leptons of the first two generations and ν_ℓ refers to their associated neutrinos.

4.2 Event Selection

The event signature for the lepton+jets decay of a $t\bar{t}$ pair is four energetic jets, a lepton with large transverse momentum and a large transverse momentum imbalance from the undetected neutrino. Extra jets may appear in the event due to initial or final state radiation, and I allow for extra jets in my selection[1]. To enhance the purity of the sample, jets from heavy flavor decays are identified, or "tagged." My event selection criteria are summarized in Table 4.2. For the calculation of $d\sigma/dM_{t\bar{t}}$, as defined in Equation 1.50, the data is binned according to the value of $M_{t\bar{t}}$ in each event. I choose bins with widths approximately equal to the resolution of the CDF detector. The resolution depends on the value of $M_{t\bar{t}}$ but is on average 50 GeV/c^2. In the leading edge and tails of the distribution the bins are wider to account for the smaller number of expected events in those bins. The binning of $M_{t\bar{t}}$ used in this analysis is given in Table 4.3. In the next section I describe the trigger that is used in the collection of data and follow with a discussion of the reconstruction of each physics object in the event.

Jets	≥ 4 with $E_T > 20$ GeV and $\|\eta\| < 2$
Lepton	CEM, CMUP or CMX lepton with $E_T > 20$ GeV
$\not\!\!E_T$	> 20 GeV
B-tagging	≥ 1 tight `SecVtx` tag

Table 4.2: Summary of event selection used in this analysis.

Bin	$M_{t\bar{t}}$ [GeV/c^2]
1	0 - 350
2	350 - 400
3	400 - 450
4	450 - 500
5	500 - 550
6	550 - 600
7	600 - 700
8	700 - 800
9	800 - 1400

Table 4.3: Binning of $M_{t\bar{t}}$ used in this analysis.

4.2.1 Trigger

The selection of events in data begins with the trigger. The CDF trigger system was described in Chapter 2. The triggers used in this analysis require an electron or muon with high transverse momentum [28]. The trigger requirements for the electron path are:

Level 1 An XFT track with $p_T > 8$ GeV/c matched to a trigger tower in the CEM with $E_T > 8$ GeV and the ratio of hadronic to electromagnetic energy is less than 0.125.

[1] Also it is possible that jets may be lost due to geometric or kinematic requirements, but I do not allow for fewer than four jets in this analysis

Level 2 The energy of neighboring trigger towers with $E_T > 7.5$ GeV is added to the single trigger tower at level 1. The total transverse energy deposit must be greater than 16 GeV.

Level 3 A track with $p_T > 9$ GeV/c matched to an energy cluster in three adjacent towers with $E_T > 18$ GeV with ratio of hadronic to electromagnetic energy less than 0.125. Also the lateral shower profile of the cluster must be less than 0.4 and the distance between the extrapolated track position and the CES measurement in the z-direction must be less than 10 cm.

The trigger requirements for the muon path are:

Level 1 An XFT track with $p_T > 4$ GeV/c matches to a muon track segment with $p_T > 6$ GeV/c for CMUP muons, or a track with $p_T > 8$ GeV/c matched to a segment with $p_T > 6$ GeV/c for CMX muons.

Level 2 There are no additional requirements at level 2.

Level 3 A track with $p_T > 18$ GeV/c matched to a track segment in the muon chambers within 18 cm in $r - \phi$ for all muon types and within 20 cm in z for CMUP muons only.

The efficiency of the triggers is measured in data [29]. A high purity sample of $Z^0 \to \ell^-\ell^+$ events are selected. One lepton is required to be the trigger lepton, the other lepton is the "probe lepton" and it must have the opposite charge of the trigger lepton. The invariant mass of the two leptons must be within the Z^0 mass window. The efficiency of the trigger is the ratio of the probe leptons which pass the trigger to the total number of probe leptons. The efficiencies of the triggers for the various lepton types are given in Table 4.4. The quoted efficiencies are a luminosity-weighted average of the efficiencies measured for various run periods for the complete 2.7 fb^{-1} of data analyzed here.

CEM Electrons	CMUP Muons	CMX Muons
0.964 ± 0.005	0.888 ± 0.008	0.912 ± 0.010

Table 4.4: Efficiencies of the various triggers used in this analysis.

4.2.2 Lepton Identification

Offline lepton identification imposes tighter requirements on the electron or muon. More information on these requirements can be found in Reference [28]. The requirements for electron identification are summarized in Table 4.5. The electron must have a COT track with $p_T > 9$ GeV/c pointing to a cluster of energy in three adjacent towers in pseudorapidity in the CEM with $E_T > 20$ GeV. The ratio of hadronic to electromagnetic energy in the cluster, E_{had}/E_{em}, must be small. The lateral shower profile L_{shr} - the distribution of energy in adjacent CEM towers - must be consistent with electron test beam data. Likewise the CES shower profile in the z view must be consistent with test beam data, as quantified by χ^2_{strip}. The values Δx and Δz are the distances between the extrapolated COT track and the CES shower profile in the $r - \phi$ and z views, respectively. The requirement on Δx is signed to allow for breamsstrahlung photons that are emitted as the lepton passes through

the detector. These distances are required to be small. The ratio of electron's energy to momentum, E/p, which should be close to one, must be less than 2, except for very high p_T electrons. These high momentum electrons lose momentum by emitting collinear photons. The electrons must also be well isolated. The quantity isolation is defined as the ratio of additional transverse energy in a cone of radius $R = \sqrt{(\delta\eta)^2 + (\eta\phi)^2} = 0.4$ around the cluster to the energy of the cluster. Photon conversions are explicitly vetoed by looking for two oppositely charged tracks with a small opening angle between them.

Property	Requirement
E_T	≥ 20 GeV
E_{had}/E_{em}	$\leq 0.055 + 0.00045 \cdot$E(GeV)
L_{shr}	≤ 0.2
χ^2_{strip}	≤ 10
$\lvert\Delta z\rvert$	≤ 3.0 cm
$Q \cdot \Delta x$	≥ -3.0 cm, ≤ 1.5 cm
E/p	≤ 2.0 or $p_T > 50$ GeV/c
Isolation	≤ 0.1
Photon Conversion	Veto

Table 4.5: Requirements for electron identification.

The efficiency of these electron identification requirements is measured in $Z \rightarrow e^- e^+$ data using the trigger and probe lepton technique of the trigger efficiency measurement. The efficiency is 0.789 ± 0.004. For this analysis systematic differences between lepton identification in data and Monte Carlo simulation are important as they alter the efficiency of the event selection. These differences are corrected for by a scale factor, the ratio of the identification efficiency in data to Monte Carlo simulation, which is measured to be 0.981 ± 0.005. The efficiency of the conversion veto, not accounted for in these numbers, is 1.00 ± 0.014.

The offline muon identification requirements are summarized in Table 4.6. Muons must have COT track with $p_T \geq 20$ GeV/c that extrapolates to a track segment in the muons chambers. The energy in the hadronic and electromagnetic calorimeters must be consistent with the energy deposition of minimum ionizing particles. The distances in x - the drift direction - between the extrapolated COT track and the track segment in the the muon chambers must be small. Muons with segments in the CMU must also have segments in the CMP, and vice versa, these muons are called CMUP muons. The distance of closest approach of the track to the beam line in the transverse direction, d_0, must be small. This requirement rejects hadrons which decay in flight and muons from cosmic rays. Isolation is defined similarly to the electron case - the ratio of transverse energy in cone of radius 0.4 around the track to the muon transverse momentum - and it must be small. Cosmic ray muons are explicitly vetoed by using timing information from the COT. Events where a charged particle track travels toward instead of away from the center of the detector are rejected. The efficiency of these muon identification cuts is 0.829 ± 10116 for CMUP muons and 0.893 ± 0.006 for CMX muons. Again a scale factor must be applied to account for differences muon identification in data and Monte Carlo simulation. This scale factor is measured to be 0.921 ± 0.007 for CMUP

muons and 0.966 ± 0.011 for CMX muons. The efficiency of the cosmic ray veto, not included, is 1.00 ± 0.010.

Property	Requirement
p_T	≥ 20 GeV
E_{had}	$\leq$ max$(6, 6 + 0.0280(p - 100))$ GeV
E_{em}	$\leq$ max$(2, 2 + 0.0115(p - 100))$ GeV
CMU$\lvert\Delta x\rvert$	≤ 3.0 cm
CMP$\lvert\Delta x\rvert$	≤ 5.0 cm
CMX$\lvert\Delta x\rvert$	≤ 6.0 cm
$\lvert d_0\rvert$	$\leq 0.02(0.2)$ cm with (without) silicon tracking
Isolation	≤ 0.1
Cosmic Ray	Veto

Table 4.6: Requirements for muon identification.

To remove backgrounds from diboson (WW, WZ and ZZ) production in association with jets events exactly one high p_T lepton is required. To further reduce the background from Z decays, any event where the high p_T lepton and a second softer lepton (with less stringent identification requirements) form an invariant mass within the Z mass window is removed.

4.2.3 Track and Primary Vertex Reconstruction

For all lepton candidates, the COT track must pass certain quality requirements. The track must have at least three axial and three stereo COT superlayer track segments. Each segment must have at least seven attached hits out of a possible total of twelve hits. Additionally, the track is constrained to the beam position in the transverse plane.

The z position of event is determined by the z position of the primary vertex. I discuss vertex reconstruction in more detail in Section 4.3. Events are required to have a z position within 60 cm of the center of the detector. However, the luminosity is measured for the entire luminous region. A correction factor, measured in data to be 0.967 ± 0.003, is applied to account for the different regions for the measured luminosity and the accepted events.

4.2.4 Jet Reconstruction and Uncertainties

A jet is seen in the detector as a large number of tracks pointing to a deposition of energy in the calorimeters. The four-momenta of jets measured by the calorimeters, p^{jet}, must be corrected for various detector and physics effects. This correction determines the "jet energy scale." The procedure used by CDF to correct jets is described in detail in Reference [30]. The transverse momenta of the underlying partons, p_T^{parton}, is related p_T^{jet} through a series of corrections:

$$p_T^{parton} = (p_T^{jet} \times C_\eta - C_{MI}) \times C_{Abs} - C_{UE} + C_{OOC} = p_T^{particle} - C_{UE} + C_{OOC}. \quad (4.1)$$

The corrections are:

C_η is an η-dependent correction which makes the calorimeter response uniform with respect to the polar angle.

C_{MI} corrects for multiple interactions - when more than one $p\overline{p}$ interaction occurs per bunch crossing.

C_{Abs} is an absolute scale correction to the momentum of a particle jet from the calorimeter momentum. The momentum of the particle jet is the sum of the momenta of all hadrons, leptons and photons within the jet cone. A particle jet is independent of the CDF detector and can be compared to theory.

C_{UE} corrects for the underlying event - contributions to the jet energy which are not related to the parent parton. These contributions include interactions with the non-interacting (spectator) partons of the proton/anti-proton and initial state radiation.

C_{OOC} corrects for energy that falls outside the jet cone.

The correction is derived according to the transverse momenta of the jet, but is applied to all components of the jet four-momenta.

Jets are clustered by applying an iterative cone algorithm. The cone size, R, is defined as:

$$R = \sqrt{(\eta^{tower} - \eta^{jet})^2 + (\phi^{tower} - \phi^{jet})^2} \tag{4.2}$$

where the center of the jet is (η^{jet}, ϕ^{jet}) and $(\eta^{tower}, \phi^{tower})$ refer to the calorimeter towers. Towers with $E_T > 1$ GeV form seed towers. Additional towers are added, up to the maximum radius R. The clustering is iterated, merging and splitting jets, until the jets are stable - meaning a single tower does not contribute to more than one jet and the list of towers in a jet does not change. The jet corrections and their associated uncertainties depend on the size of the cone. In this analysis I use jets with $R = 0.4$.

η Dependent Corrections

The central region of the calorimeter is better understood and instrumented than the forward regions. This correction scales the energy of jets outside the region $0.2 < |\eta| < 0.6$ to jets inside this region. The correction is derived by balancing the transverse momentum of jets in dijet events. The transverse momentum of a "trigger jet" in the central region is balanced with a random "probe jet." The ratio of probe to trigger jet p_T, β, is shown in Figure 4.1. The η-dependent corrections are then $1/\beta$. The quantity β is calculated in different jet p_T bins and applied according to jet p_T and η.

The deviation of the dijet balance from one is taken as an uncertainty on the correction. Further uncertainties are assessed by varying the selection of dijet events and the fitting procedure. The uncertainty as a function of jet η for various jet p_T bins is shown in Figure 4.2.

Corrections for Multiple Interactions

For events with more than one $p\overline{p}$ interaction per bunch crossing, extra energy not associated with the primary interaction is included with the reconstructed jet energy if the final states overlap.

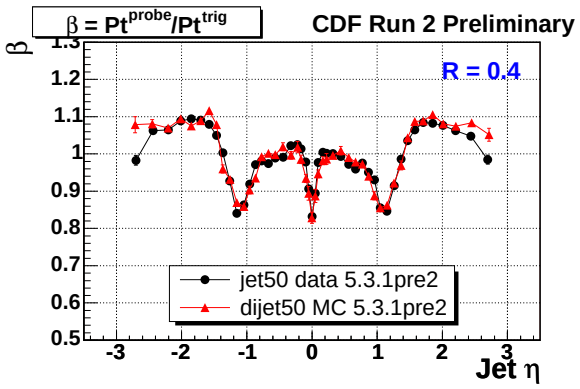

Figure 4.1: The ratio of probe to trigger jet p_T [31].

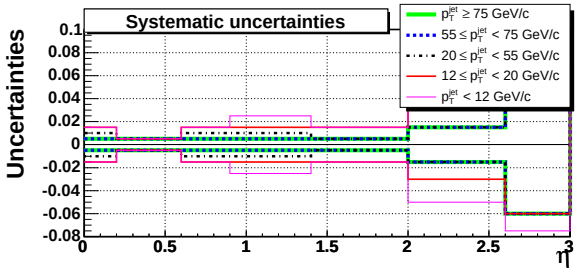

Figure 4.2: The uncertainties on the η-dependent jet corrections in various jet p_T bins [31].

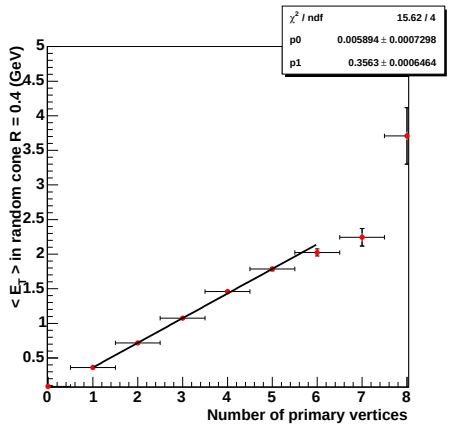

Figure 4.3: The average transverse energy in a cone of radius R=0.4 in a minimum bias data sample [31].

This energy is subtracted from the measured jet energy. The correction is derived as a function of the the number of vertices reconstructed in the event in data taken with a minimum bias trigger. The minimum bias trigger's only requirement is that an inelastic $p\overline{p}$ interaction has occurred. The correction is made by subtracting the average transverse energy in a random cone of size R in the data from the jet transverse energy. The value of this correction is shown in Figure 4.3.

The correction is cross-checked in samples with different topologies. The uncertainty is dominated by the limited statistics of the samples, and is taken to be 15%. The fractional uncertainty as a function of jet p_T is shown in Figure 4.4.

Absolute Energy Scale Corrections

The absolute correction is the final correction needed to transform a calorimeter jet to a particle jet. The particle jet consists of all particles - hadrons, leptons and photons - within the jet cone. The correction is derived entirely from Monte Carlo simulation and is limited by the accuracy of the simulation. For a distribution of jet transverse momenta associated with a fixed value of $p_T^{particle}$, the absolute jet energy is defined as the most probable value of p_T^{jet}. The absolute scale is the difference between the energy of the particle jet and the corrected jet energy. The scale applied, along with the uncertainty, is shown in Figure 4.5.

Underlying Event and Out of Cone Corrections

In order to reconstruct the parton momentum, further corrections to $p_T^{particle}$ are needed. The first correction, for the underlying event, removes energy associated with particles in the hard interaction that are not the parent parton, such as initial state radiation. The out of cone corrections accounts for energy losses due to the finite size of the jet cone. These corrections are derived entirely from Monte Carlo simulation, using the same method as the absolute energy scale correction. The uncertainties are assessed by varying parameters in the simulation. The correction and uncertainties for the

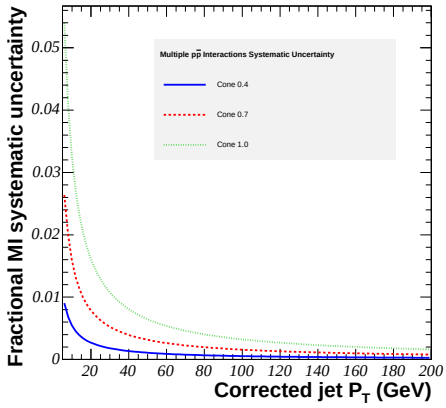

Figure 4.4: The uncertainty of the multiple interaction correction as function of jet p_T [31].

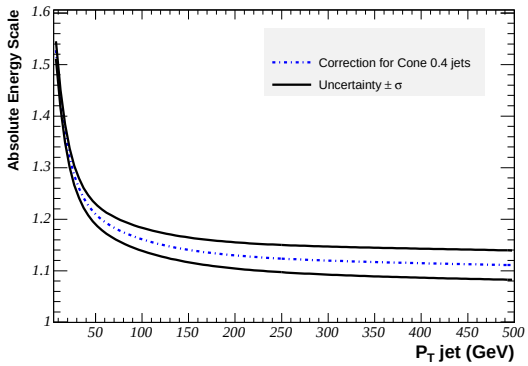

Figure 4.5: The absolute jet energy scale correction with uncertainties are a function of jet p_T [31].

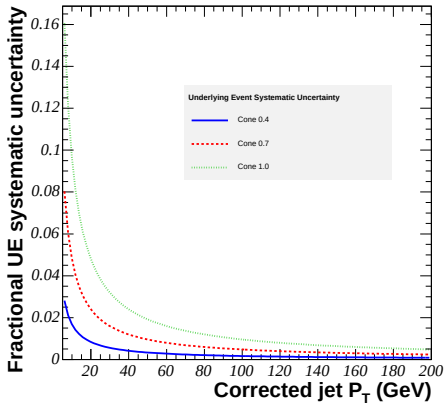

Figure 4.6: The underlying event jet energy scale correction with uncertainties are a function of jet p_T [31].

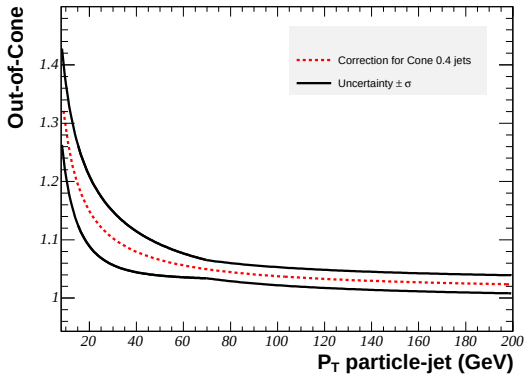

Figure 4.7: The out of cone jet energy scale correction with uncertainties are a function of jet p_T [31].

underlying event is shown in Figure 4.6 and for the out of cone correction is shown in Figure 4.7.

In practice the out of cone and underlying event corrections are not usually applied, and are only used for the evaluation of systematic uncertainties. These corrections are derived from generic dijet Monte Carlo simulation, in other words, no particular physics process is assumed. If the energy of the parent parton is needed, process specific corrections are usually applied. This is the approach that I take. I select jets which have been corrected for η-dependence, multiple interactions and the absolute energy scale. The corrected transverse energy of these jets must be greater that 20 GeV.

The total uncertainty on the jet energy scale as a function of jet p_T is shown in Figure 4.8. The fractional uncertainty on the jet energy scale is smallest at high jet p_T, approximately 3%, and largest a low jet p_T, approximately 10%. For an analysis that relies as heavily on jet quantities as mine, the uncertainty on the jet energy scale is a dominant source of uncertainty in the final analysis. However, this uncertainty can be reduced by using the well-known W mass to constrain

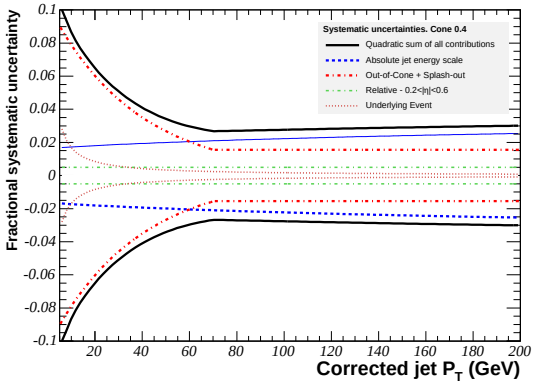

Figure 4.8: The total uncertainty on the jet energy scale as a function of jet p_T [31].

the jet energy scale in hadronic W decays. This technique was first used in [40] as a way to reduce the uncertainty on the top quark mass from the jet energy scale.

4.2.5 Missing Transverse Energy Reconstruction

The missing transverse energy, $\not\!\!E_T$, is associated with the undetected neutrino in the lepton+jets event. It is defined as the magnitude of the vector $-\sum_i (E_{T,i} cos\phi_i, E_{Ti} sin\phi_i)$ where the sum runs over calorimeter towers. For events with muons, the missing energy is corrected for the small amount of energy that the muon deposits in the calorimeter towers. The $\not\!\!E_T$ vector is also corrected for the effects of the jet energy scale corrections applied to the jets. My event selection requires events with $\not\!\!E_T > 20$ GeV.

4.3 Heavy Flavor Tagging

The data selected according to the event selection criteria described above will be contaminated by non-$t\bar{t}$ processes. The largest background is $W^{\pm}$ bosons produced in association with jets. I will discuss in detail the composition of the data sample in the next chapter. Generally the $t\bar{t}$ signal can be distinguished from the background processes by the heavy flavor in the final state. There are several techniques that can be used to identify heavy flavor content in jets. As I discussed in Chapter 1, the b-hadrons have long lifetimes, on the order of picoseconds. The b-hadrons then travel several millimeters in the detector before decaying. The secondary vertex (`SecVtx`) tagging algorithm looks for displaced secondary vertices, with respect to the primary event vertex, to identify the long-lived hadrons [32]. Another technique that can used to identify heavy flavor content is to tag the semileptonic decays of the b-hadrons. This technique is called soft lepton tagging (`SLT`). `SLT` tagging with muons is described in detail in [34]. The `SecVtx` method, which I use, has the highest efficiency for tagging $t\bar{t}$ events of the commonly used algorithms. In the lepton+jets channel, requiring at least one `SecVtx` tag reduces the background contamination of the data sample by about

95% while reducing the amount of $t\bar{t}$ signal by less than half.

Accurate reconstruction of secondary vertices requires precise reconstruction of the event primary vertex, the origin of all prompt tracks in the event. Vertices are reconstructed from only well measured COT and silicon tracks. For events with more than one identified vertex, the vertex that is closest to the high momentum lepton is the primary vertex. The transverse position of the primary vertex is resolved to $10 - 32\mu$m, depending on the exact event topology.

The `SecVtx` algorithm works on a per-jet basis. Good tracks within the jet cone are selected according to the quality of the silicon tracking information and the reduced χ^2 of the track fit. Jets with at least two good tracks are considered "taggable" and are analyzed by the `SecVtx` algorithm. The algorithm uses two passes to find secondary vertices in the taggable jets. The first pass looks for at least three tracks with $p_T > 0.5$ GeV/c and $d_0/\sigma_{d_0} > 2.5$, one of which must have $p_T > 1$ GeV/c, and attempts to reconstruct a vertex. If the first pass fails the second pass attempts to reconstruct a two track vertex of tracks with $p_T > 1$ GeV/c and $d_0/\sigma_{d_0} > 3$.

If a secondary vertex is found, the two-dimensional decay length of the secondary vertex, L_{xy}, is calculated. L_{xy} is the projection of a vector which points from the primary vertex to the secondary vertex onto the jet axis in the $r-\phi$ view. A cartoon of a displaced secondary vertex and the distance L_{xy} is shown in Figure 4.9. L_{xy} is signed relative to the jet direction. If the absolute difference in ϕ between the jet axis and secondary vertex vector is less than 90° the tag is positive, if the difference is more than 90° the tag is negative. The jet is tagged if $|L_{xy}/\sigma_{L_{xy}}| > 3$ ("tight" `SecVtx` tags). For reference, the "loose" SecVtx tags require $|L_{xy}/\sigma_{L_{xy}}| > 7$. The uncertainty on the measured L_{xy}, $\sigma_{L_{xy}}$, is typically 190 μm. Secondary vertices from heavy flavor generally decays have positive tags. Secondary vertices which result from mis-measured tracks tend to have negative tags. My event selection requires at least one jet with a positive `SecVtx` tag.

The efficiency to tag b-jets as a function of jet E_T in a Monte Carlo simulation of $t\bar{t}$ events is shown in Figure 4.10. A correction factor is applied to account for differences in tagging in data and Monte Carlo simulation. This factor is measured to be 0.95 ± 0.05.

4.4 $t\bar{t}$ Signal

I reconstruct the invariant mass of the $t\bar{t}$ event, $M_{t\bar{t}}$, by combining the four-momenta of the lepton, jets and missing transverse energy (the z-component is set to zero). I use an unfolding technique, which I will describe in Chapter 7, to correct $M_{t\bar{t}}$ to the true (partonic) $t\bar{t}$ invariant mass, $M_{t\bar{t}}^{true}$. The differential cross section, as given in Equation 1.50, is then calculated in bins of $M_{t\bar{t}}^{true}$.

4.4.1 Acceptance

The event selection described above is applied to a `PYTHIA` simulation of $t\bar{t}$ events. The efficiency of the selection is needed in each bin of $M_{t\bar{t}}^{true}$ for the calculation of $d\sigma/dM_{t\bar{t}}$. The acceptance in each bin, $\mathcal{A}_i$, is given by the ratio $\frac{N_{sel}^i}{N_{gen}^i}$. The acceptance in each bin of $M_{t\bar{t}}^{true}$ is given for each lepton type in Table 4.7. The quoted uncertainties reflect the statistical uncertainty from the finite size of the simulated event sample. This raw acceptance needs to be corrected for many effects to obtain

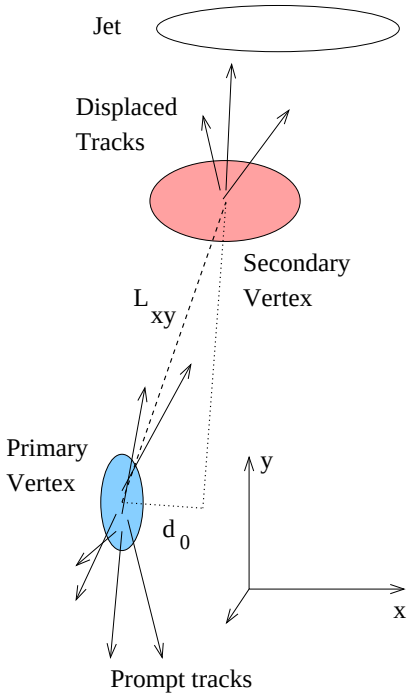

Figure 4.9: A cartoon jet with a displaced secondary vertex [35].

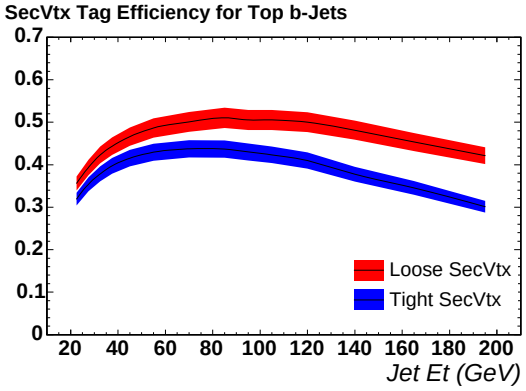

Figure 4.10: `SecVtx` b-tagging efficiency for $t\bar{t}$ events as a function of jet E_T. [35].

the event selection efficiency:

1. There is no trigger in the Monte Carlo simulation. The value of $\mathcal{A}_i$ in each bin is multiplied by the appropriate trigger efficiency for the lepton type, as given in Table 4.4.

2. Likewise the $\mathcal{A}_i$ must be multiplied by the efficiencies of the cosmic and conversion vetoes, as given in Section 4.2.2 because there are not applied in the Monte Carlo simulation.

3. The value of $\mathcal{A}_i$ must be corrected for differences in lepton identification efficiency in data and Monte Carlo. $\mathcal{A}_i$ is multiplied by the appropriate lepton identification scale factors given in Section 4.2.2.

4. The acceptance is corrected for the requirement that that $|z| < 60$ cm. The scale factor is given in Section 4.2.3.

5. The acceptance is also corrected for the difference in tagging efficiency in data and Monte Carlo as given in Section 4.3.

Bin Number	all	1	2	3	4	5	6	7	8	9
CEM Leptons										
$\mathcal{A}_i$	0.017	0.010	0.015	0.017	0.018	0.019	0.019	0.019	0.020	0.015
$\sigma_{\mathcal{A}_i}$	3e-08	2e-06	8e-08	1e-07	2e-07	3e-07	6e-07	7e-07	2e-06	5e-06
CMUP Leptons										
$\mathcal{A}_i$	0.010	0.0068	0.0093	0.010	0.011	0.012	0.012	0.012	0.011	0.0091
$\sigma_{\mathcal{A}_i}$	2e-08	1e-06	7e-08	8e-08	1e-07	3e-07	5e-07	6e-07	2e-06	4e-06
CMX Leptons										
$\mathcal{A}_i$	0.0046	0.0029	0.0043	0.0047	0.0048	0.0052	0.0052	0.0054	0.0051	0.004
$\sigma_{\mathcal{A}_i}$	2e-08	8e-07	4e-08	5e-08	9e-08	2e-07	3e-07	4e-07	1e-06	3e-06

Table 4.7: Acceptances for events with CEM, CMUP and CMX leptons which pass the event selection. The bins are defined in Table 4.3.

After the raw acceptance has been corrected the efficiency of the selection in each bin, ε_i, is the sum of the corrected acceptances for each lepton type. The values of ε_i are given in Table 4.8. The selection efficiency is approximately 3%. The efficiency is lower in the very low and very high bins of $M_{t\bar{t}}$.

Bin Number	all	1	2	3	4	5	6	7	8	9
CEM Leptons										
ε_i	0.015	0.0088	0.013	0.015	0.015	0.016	0.017	0.017	0.017	0.013
σ_{ε_i}	8e-04	5e-04	7e-04	8e-04	8e-04	9e-04	9e-04	9e-04	9e-04	7e-04
CMUP Leptons										
ε_i	0.0078	0.0051	0.0070	0.0078	0.0084	0.0088	0.0090	0.0090	0.0085	0.0068
σ_{ε_i}	5e-04	3e-04	4e-04	5e-04	5e-04	5e-04	6e-04	5e-04	5e-04	4e-04
CMX Leptons										
ε_i	0.0037	0.0023	0.0034	0.0038	0.0039	0.0042	0.0041	0.0044	0.0041	0.0032
σ_{ε_i}	2e-04	1e-04	2e-04	2e-04	2e-04	2e-04	2e-04	3e-04	2e-04	2e-04
All Leptons										
ε_i	0.026	0.016	0.023	0.026	0.027	0.029	0.030	0.030	0.030	0.023
σ_{ε_i}	9e-04	6e-04	8e-04	9e-04	1e-03	1e-03	1e-03	1e-03	1e-03	9e-04

Table 4.8: Event selection efficiency for events which pass the event selection according to lepton type and $M_{t\bar{t}}$ bin. The bins are defined in Table 4.3.

4.4.2 Reconstruction of $t\bar{t}$ Events

For analyses that require complete kinematic information about the $t\bar{t}$ system, the reconstruction of the top and anti-top four-momenta from the lepton, missing transverse energy, and jet four-momenta in a lepton plus jets event presents challenges. This includes not only analyses of the $M_{t\bar{t}}$ spectrum in $t\bar{t}$ events but also measurements of the top quark mass, the helicity of the $W^{\pm}$, and the forward-background asymmetry in $t\bar{t}$ production. This is true even in the absence of background. The difficulties include:

The energy and momentum of the quarks must be inferred The b-quark daughters of the $t\bar{t}$ pair and the light quark daughters of the hadronically decaying W are seen as jets in the detector. The four-momenta of the quarks must be inferred from the four-momenta of the jets, with large uncertainties, as I discussed in Section 4.2.4.

The z-component of the neutrino momentum is not measured The neutrino from the leptonic W decay is detected as an imbalance in the transverse momentum measured in the detector. The momentum imbalance in the z-direction, which points along the beam, cannot be measured.

Missing energy resolution is generally poor The x and y components of the neutrino momentum are identified with the x and y components of the missing transverse momentum. The resolution of the missing transverse momentum suffers the same shortcomings of the jet energy resolution. The resolution is also worsened by cracks in the calorimetry and non-instrumented regions of the detector.

Extra jets not from top Jets in the event which do not originate from the $t\bar{t}$ pair are also problematic. For instance, the momentum of a jet radiated by the colliding quarks or gluons should not be included in the momentum of the $t\bar{t}$ final state.

Loss of jets from top Likewise, the kinematic requirements on the jets can result in jets from top being lost. For example, for a very energetic $t\bar{t}$ pair the jets will be highly boosted and may merge. In this case less than four jets will be counted and the event is lost.

Also, though it is not required in an $M_{t\bar{t}}$ analysis[2] the assignment of jets to quarks in a $t\bar{t}$ event is ambiguous. If you assume that jets with b-tags have been identified correctly, there are six (two) ways to assign the jets to quarks for events with one (two) b-tags. This presents an extra challenge for cases where the assignment is required by the analysis technique. In this analysis I avoid the combinatoric issue by calculating the event invariant mass.

[2]In a measurement of, for example, the top quark mass, it is necessary to identify which top decays to a b and the leptonic $W^{\pm}$ and which top decays to a b and the hadronically decaying $W^{\pm}$ because the top and anti-top four-momenta must be distinguished. In an $M_{t\bar{t}}$ analysis it is not necessary to distinguish the four-momenta of the top and anti-top. However, the resolution of the measurement can often be improved when the four-momenta are separated because the invariant masses of the top and anti-top can constrain the invariant masses of their respective decay daughters.

4.5 Data Sample

This analysis uses 2.7 fb^{-1} of data collected between February 2002 and April 2008. The number of events passing the event selection, divided according to lepton type and jet bin, is shown in Table 4.9.

Lepton Type	1-jet	2-jets	3-jets	4-jets	$\geq$ 5-jets
CEM	2208	1161	513	279	85
CMUP	1061	503	203	148	45
CMX	636	232	97	67	26
All	3905	1926	813	494	156

Table 4.9: The event counts after event selection according to lepton trigger type and jet bin. The signal region is $\geq$ 4-jets, for a total of 650 events in 2.7 fb^{-1} of data.

Chapter 5

Standard Model $t\bar{t}$ Backgrounds

5.1 Introduction

Non-$t\bar{t}$ processes which result in a final state similar to the lepton+jets state are backgrounds and must be removed from the data sample in order to calculate $d\sigma/dM_{t\bar{t}}$. For the b-tagged final state the dominant background is W boson production in association with jets which have heavy flavor content. The next largest background is W boson production is association with jets that do not have heavy flavor content, but have nonetheless been tagged. Such tags are called "mistags." The final large background is events that do not have a real W bosons. In these events the isolated high p_T lepton and large $\not\!\!E_T$ signature from the leptonically decaying W has been faked by a mismeasurement or a heavy flavor quark which decays semi-leptonically. These events are referred to as "non-W" or QCD backgrounds. Finally there are many smaller backgrounds from electroweak (EW) diboson production and single-top production.

Ideally the theoretical cross section for each of these processes would be calculated to a high degree of precision and verified experimentally. Then the number of events for process X could be obtained by inverting Equation 1.47:

$$N_X = \sigma_X \cdot \varepsilon \cdot \int \mathcal{L} dt. \tag{5.1}$$

In reality the theoretical cross section for the largest W+jets backgrounds are only known to lowest order in QCD. These lowest order calculations suffer from large uncertainties and cannot be used the constrain the normalization of the W+jets backgrounds. Furthermore, tagging rates in Monte Carlo simulation do not agree with tagging rates in data. Recall that a scale factor was needed to correct the efficiency of the event selection for the tag rate difference in data and Monte Carlo simulation. In Monte Carlo simulation the tagging rate is too high, so this factor was less than one. At the same time, the rate of mistags in simulation tends to be too low so an alternative approach is needed for this background as well. The non-W background presents its own challenges. It is not clear how these events, where the leptonic W has been faked, should be modeled in Monte Carlo simulation. Again an alternative approach is needed.

The technique used by CDF to calculate the $t\bar{t}$ backgrounds in the `SecVtx` tagged lepon+jets sample is described in [32]. In this chapter I will review the method used to calculate the normalizations of each background. These results were obtained for the integrated $t\bar{t}$ cross section in 2.7 fb^{-1} of data [36]. I will conclude with a description of the $M_{t\bar{t}}$ distribution of the backgrounds.

5.2 Normalization of the Backgrounds

The strategy of this background estimate is to use well-known quantities to constrain the W+heavy flavor and mistag backgrounds. While the leading order QCD prediction for the normalization of the W+heavy flavor production is largely uncertain, the fraction of W+heavy flavor events in the W+jets sample, F_{hf}, is better modeled to leading order (by taking the ratio, many uncertainties cancel). The number of tagged W+heavy flavor events is then:

$$N_{tag}^{W+hf} = N_{pretag}^{W+jets} \cdot F_{hf} \cdot \epsilon_{tag} = N_{pretag}^{W+hf} \cdot \epsilon_{tag} \tag{5.2}$$

where ϵ_{tag} is the tagging efficiency:

$$\epsilon_{tag} = \frac{N_{tag}}{N_{pretag}} \tag{5.3}$$

and N_{pretag}^{W+jets} is the number of W+jets events in the sample before tagging ("pretag"). The pretag sample has passed all event selection requirements except for the requirement for at least one tight `SecVtx` tag. The number of mistags in data is, to first order, equal to the number of negative `SecVtx` tags, N_-. Then the number of mistags in the W+jets sample is given by the mistag rate, $\frac{N_-}{N_{pretag}}$, times the number of W+lf events:

$$N_{tag}^{W+lf} = \frac{N_-}{N_{pretag}} \cdot (N_{pretag}^{W+jets} - N_{pretag}^{W+hf}) \tag{5.4}$$

The missing piece in the above equation is the W+jets component of the pretag sample. N_{pretag}^{W+jets} is determined by removing from the total pretag sample the contributions from $t\bar{t}$, electroweak processes and non-W production:

$$N_{pretag}^{W+jets} = N_{pretag} - (N_{pretag}^{t\bar{t}} + N_{pretag}^{non-W} + N_{pretag}^{EW}). \tag{5.5}$$

The background estimate proceeds by a sequential process as follows:

- The number of pretag events from electroweak processes is calculated according to the theoretical cross section for each process.
- The number of $t\bar{t}$ events present in the pretag sample is calculated according to the theoretical cross section for a 175 GeV/c^2 top quark mass.
- The fraction of non-W events, $F_{\text{non}-W}$ is measured, as I will described in Section 5.2.3, and the number of non-W events in the pretag sample is given by $F_{\text{non}-W} \cdot N^{pretag}$.
- The W plus heavy flavor content of the tagged sample is determined as described above.
- The mistag background is determined.
- The predictions for the electroweak, $t\bar{t}$, and non-W backgrounds at tag level are determined by adjusting the pretag predictions by the tagging efficiency for each process.

The estimates are derived separately for each type of trigger lepton - CEM, CMUP or CMX - and for different numbers of jets in the event. The one and two jet bins are background dominated and serve as a control region for the background estimate. The integrated cross section measurement is performed with events with ≥ 3 jets, while I select only events with ≥ 4 jets.

5.2.1 Electroweak and Monte Carlo Derived Backgrounds

Processes that result in the production of pairs of W and Z mimic the $t\bar{t}$ process when the one boson decays to leptons and the over decays to jets. The third and fourth jets in the event are provided by gluon radiation from the initial or final state quarks. These processes include WW, WZ, and ZZ[1] production, and are mostly rejected by the requirement of exactly one high p_T charged lepton. There is also a small amount of background from electroweak production of single top quarks. These processes have well-known theoretical cross sections and the normalizations are calculated according to Equation 5.1 where ε is the efficiency of the pretag event selection. The background from Z plus jets production, where the Z decays to a pair of charged leptons, is included in these Monte-Carlo derived backgrounds as well. This background is quite small as the events are required to pass a Z veto, so the large uncertainty has little effect. The theoretical cross sections for each of these processes are given in Table 5.1. I will collectively refer to all of these processes as electroweak processes, with N^{EW}_{pretag} events in the pretag sample and N^{EW}_{tag} events in the tag sample.

Process	Cross Section [pb]
t-channel single top	1.98 ± 0.08
s-channel single top	0.88 ± 0.05
WW	12.4 ± 0.25
WZ	3.96 ± 0.06
ZZ	1.58 ± 0.02
Z+jets	787.4 ± 50

Table 5.1: Cross sections used in calculation of Monte Carlo derived backgrounds. [33]

5.2.2 $t\bar{t}$ in the Pretag W+jets Sample

The pretag W+jets sample has a non-negligible $t\bar{t}$ component. For a 175 GeV/c^2 top quark with a theoretical cross section of 6.7 pb approximately one third of the ≥ 4 jets sample is comprised of $t\bar{t}$ events. This creates a complication for the normalization of the W+heavy flavor and mistag backgrounds as they depend on the composition of the pretag sample. A significantly different $t\bar{t}$ cross section would alter the normalizations of these backgrounds. However this is a second-order effect and my analysis is just not sensitive enough for this to be a concern. [2]

[1] In the case of ZZ production either the $\not\!\!E_T$ is faked for $ZZ \to \ell^+\ell^- jj$ or a jet in the event is misidentified as a lepton for $ZZ \to \nu\bar{\nu}jj$.

[2] The current CDF combination of measurements of the integrated $t\bar{t}$ production cross section is 7.02 ± 0.63 pb [37], consistent with the theoretical expectation used in the background calculation.

5.2.3 Non-W Background Production

Events which pass the event selection but that do not have a real W-boson will, on average, have lower $\not\!\!E_T$ because there is no real neutrino. In order to determine N_{pretag}^{non-W}, the $\not\!\!E_T$ distribution in data (with no $\not\!\!E_T$ cut) is fit for the fraction of non-W events so that the number of non-W events in the high $\not\!\!E_T$ signal region can be extrapolated from the number of non-W events in the low $\not\!\!E_T$ region. The pretag $\not\!\!E_T$ distribution is modeled by templates for each contributing process. The $t\bar{t}$, W+jets, and electroweak processes are modeled by the Monte Carlo simulations described in Chapter 3. The non-W template is constructed from a sample of "anti-electron" events. Anti-electrons are electron candidates which pass all kinematic cuts but fail two of the five non-kinematic cuts in Table 4.5. These events retain the kinematic properties of the real W events but are enriched in QCD production.

5.2.4 W+heavy flavor Production

With the above pieces in place the W+jets content of the pretag sample is known. The fraction of heavy flavor events in the W+jets sample is calculated from the `Alpgen` plus `PYTHIA` simulation described in Section 3.2.2. The heavy flavor fractions are calculated separately for events with one or two b-jets and one or two c-jets. The heavy flavor fractions and tagging efficiencies are given in Table 5.2.

Jet Multiplicity	1-jet	2-jets	3-jets	4-jets	$\geq$ 5-jets
Heavy Flavor Fractions [%]					
1b	0.75	1.56	2.57	3.37	3.97
2b	0	0.94	1.88	3.01	4.36
1c	5.98	9.57	11.71	12.56	12.66
2c	0	1.55	3.43	5.73	8.08
Tagging Efficiencies					
1b	30.8	33.2	35.1	36.4	40.6
2b	0	54.5	56.1	56.7	57.1
1c	6.9	8.2	9.4	11.0	13.3
2c	0	13.6	14.9	16.8	18.3

Table 5.2: Fraction of W+jets events with heavy flavor content (in percents), and the tagging efficiency for the events.

The heavy flavor fractions measured in Monte Carlo simulation are corrected by a scale factor for the difference in heavy flavor in data and Monte Carlo. The scale factor is measured in W+1-jet data and extrapolated to the $t\bar{t}$ enriched signal region. There is a systematic uncertainty associated with the extrapolation to the signal region. The heavy flavor content of the data is measured using a neural network which discriminates between heavy and light flavor jets by combining the power of several variables which differ in heavy and light flavor jets into one variable - the neural network output. The variables include, for example, the mass and transverse momentum of the secondary vertex and the significance of the L_{xy} measurement. The neural network output of the data is compared to the output for light and heavy flavor jets in Monte Carlo simulation in Figure 5.1. The

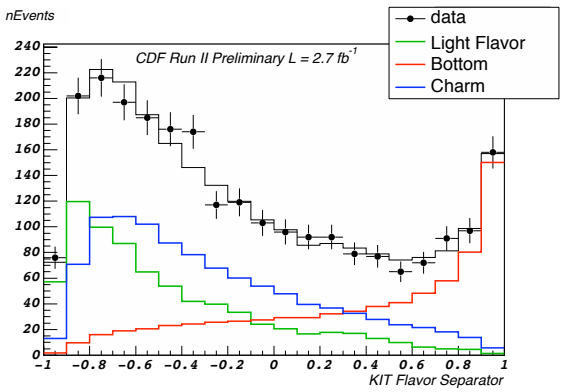

Figure 5.1: The output of the neural network used to calculate the fraction of heavy flavor in data [36]

fraction of heavy flavor is calculated by fitting the data based on these templates. The scale factor is measured to be 1.5 ± 0.3 using this technique, meaning that the heavy flavor content of data is underestimated by the Monte Carlo simulation by approximately 50%. Most likely this is due to higher order effects that are not modeled in the leading order Monte Carlo simulation.

5.2.5 Mistag Production

The rate of negative `SecVtx` tags is parameterized by five jet variables:

- jet E_T
- number of good `SecVtx` tracks
- jet η
- jet ϕ
- sum of all jet E_T in the event.

This parameterization is derived is a high statistics sample of jet data and is cross-checked in various jet samples. There is a small correction to the mistag rate for an asymmetry in the signed decay length of the secondary vertices. The combined effect of long-lived light flavor jets with positive tags and real heavy flavor jets with negative tags is an excess of positive tags. The correction factor is 1.2 ± 0.1. The mistag rate as a function of jet E_T is shown in Figure 5.2. The mistag rate is between 1 and 2%, depending on jet E_T. Because the mistag rate is so low it is extremely unlikely that more than one jet in an event will be mistagged. Therefore the corrected number of negative tags is a good estimate for the number of mistagged events.

5.2.6 Tagged Electroweak and non-W Backgrounds

The prediction for the tagged electroweak backgrounds is calculated according to Equation 5.1 where ε is the efficiency of the tagged event selection. The tagged non-W prediction is obtained by fitting

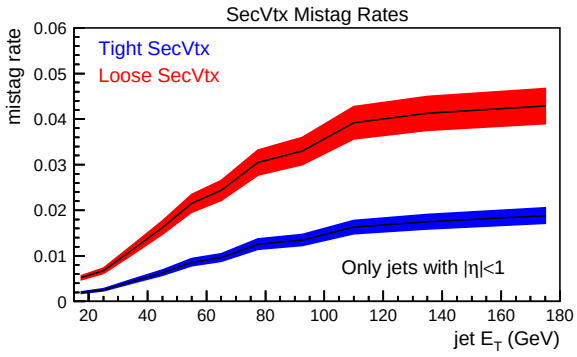

Figure 5.2: The mistag rate of the tight `SecVtx` tagger. [35]

Process	1-jet	2-jets	3-jets	4-jets	$\geq$ 5-jets
Pre-tag Data	272347	44868	7605	1686	383
Wbb	802.3 $\pm$ 244.6	498.0 $\pm$ 154.5	136.9 $\pm$ 43.3	32.3 $\pm$ 10.5	6.5 $\pm$ 2.5
Wcc	431.4 $\pm$ 135.2	219.6 $\pm$ 69.6	64.3 $\pm$ 20.7	16.8 $\pm$ 5.6	3.6 $\pm$ 1.4
Wc	1002.9 $\pm$ 314.4	260.0 $\pm$ 82.5	48.8 $\pm$ 15.7	8.9 $\pm$ 2.9	1.5 $\pm$ 0.6
Mistags	946.7 $\pm$ 143.6	310.2 $\pm$ 53.9	83.5 $\pm$ 17.2	18.9 $\pm$ 4.8	3.5 $\pm$ 1.6
Non-W	487.9 $\pm$ 146.4	356.4 $\pm$ 106.9	102.2 $\pm$ 30.6	20.9 $\pm$ 17.5	6.4 $\pm$ 6.0
WW	17.7 $\pm$ 2.3	44.1 $\pm$ 5.7	14.0 $\pm$ 1.8	3.5 $\pm$ 0.5	1.0 $\pm$ 0.1
WZ	9.0 $\pm$ 1.0	19.2 $\pm$ 2.2	5.1 $\pm$ 0.6	1.2 $\pm$ 0.1	0.3 $\pm$ 0.0
ZZ	0.7 $\pm$ 0.1	1.9 $\pm$ 0.3	1.0 $\pm$ 0.1	0.3 $\pm$ 0.0	0.1 $\pm$ 0.0
Z+jets	48.7 $\pm$ 6.7	36.3 $\pm$ 4.6	13.6 $\pm$ 1.7	3.3 $\pm$ 0.4	0.7 $\pm$ 0.1
Single Top (s-channel)	11.4 $\pm$ 1.2	42.0 $\pm$ 4.1	13.1 $\pm$ 1.3	2.8 $\pm$ 0.3	0.6 $\pm$ 0.1
Single Top (t-channel)	37.6 $\pm$ 3.3	52.4 $\pm$ 4.6	14.3 $\pm$ 1.2	2.8 $\pm$ 0.2	0.4 $\pm$ 0.0
$t\bar{t}$ (6.7pb)	19.2 $\pm$ 2.7	154.9 $\pm$ 21.6	345.4 $\pm$ 48.0	358.6 $\pm$ 49.7	121.5 $\pm$ 16.8
Total Prediction	3815.5 $\pm$ 720.1	1995.1 $\pm$ 325.3	842.0 $\pm$ 99.1	470.3 $\pm$ 56.5	145.9 $\pm$ 18.5
Observed	3906	1926	813	494	156

Table 5.3: Predicted sample composition in each jet bin for 2.7 fb^{-1} of data. [36]

.

the tagged $\not\!\!E_T$ distribution, using a tagged anti-electron template for the non-W modeling.

5.3 Data Sample Composition

The final estimate for the sample composition in each jet bin is given in Table 5.3. The prediction agrees well within the uncertainties in the control 1- and 2-jet bins. In the signal region, the observed number of events is consistent with the predicted backgrounds along with a $t\bar{t}$ signal with a total integrated cross section of 6.7 pb.

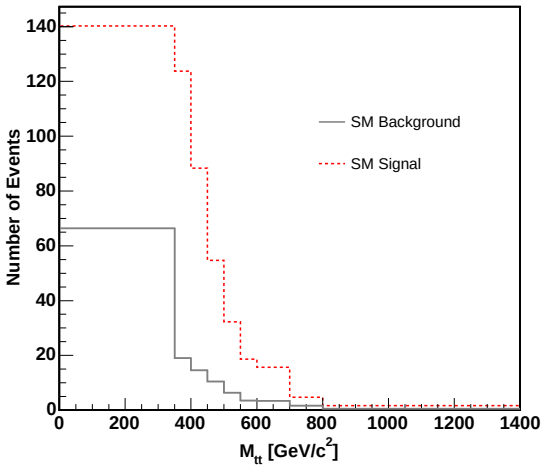

Figure 5.3: The expected $M_{t\bar{t}}$ distribution of the backgrounds. The signal distribution is shown for reference.

5.4 $M_{t\bar{t}}$ Distribution of the Backgrounds

To reconstruct the $M_{t\bar{t}}$ distribution of the backgrounds, I use the same Monte Carlo simulations, or data in the case of the non-W estimate, used to calculate the normalizations of the backgrounds. Each process is normalized according to the expectation from Table 5.3. The resulting $M_{t\bar{t}}$ distribution, binned according to Table 4.3, is shown in Figure 5.3. For comparison I also show the expected $t\bar{t}$ distribution on the same plot, normalized to the expectation in Table 5.3. The background $M_{t\bar{t}}$ distribution is softer than the signal distribution, with nearly half of the background events in the first bin of $M_{t\bar{t}}$. In the presence of background, Equation 1.50 is modified to:

$$\frac{d\sigma^i}{dM_{t\bar{t}}} = \frac{N^i_{data} - N^i_{bkg}}{\varepsilon^i \Delta^i_{M_{t\bar{t}}} \int \mathcal{L} dt} \tag{5.6}$$

where N^i_{bkg} is the expectation for the number of background events in bin i. The uncertainty on the background normalization will be taken as a systematic uncertainty on $d\sigma/dM_{t\bar{t}}$.

Chapter 6

A Review of Previous Results

6.1 Introduction

Both the CDF and DØ collaborations have studied the $M_{t\bar{t}}$ distribution for signs of new physics. In this chapter I will give an overview of the results from Run 2 of the Tevatron. These results also highlight the various techniques that can be used to study the $M_{t\bar{t}}$ spectrum. As I discussed in Section 4.4.2, the kinematic reconstruction of $t\bar{t}$ events is complicated by many effects that ultimately lessen the resolution on $M_{t\bar{t}}$.

6.2 Searches for Narrow Resonances

The CDF collaboration has completed two complementary searches for narrow resonances in the $M_{t\bar{t}}$ spectrum, using a maximum of 1 fb^{-1} of data. The searches are conducted in the lepton plus jets decay channel of the $t\bar{t}$ pair. In each case the search is optimized for a narrow leptophobic Z' - which I discussed in Section 1.4 - with width $\Gamma_{Z'} = 0.012 M_{Z'}$. Limits are set by using a binned maximum likelihood technique, where the likelihood is a Poisson function for the number of events in each bin of the $M_{t\bar{t}}$ distribution.

The first search uses the technique described in [38] which was originally developed for the measurement of the top quark mass. The result, using 680 pb^{-1} of integrated luminosity, was published in 2008 [39]. The invariant mass of the $t\bar{t}$ system is described by a probability distribution for $M_{t\bar{t}}$, given the set of measured three-momenta $\{\overrightarrow{k}\}$:

$$P(M_{t\bar{t}} \mid \{\overrightarrow{k}\}) = \int P(\{\overrightarrow{p}\} \mid \{\overrightarrow{k}\}) \delta(M_{t\bar{t}} - M_{t\bar{t}}^{true}(\{\overrightarrow{p}\})) d\{\overrightarrow{p}\} \tag{6.1}$$

where $\{\overrightarrow{p}\}$ represents the three-momenta of the final state partons in the process $p\overline{p} \rightarrow t\bar{t} \rightarrow W^+ b W^- \overline{b} \rightarrow q\overline{q'} b \ell \overline{\nu_\ell} \overline{b}$ and $P(\{\overrightarrow{p}\} \mid \{\overrightarrow{k}\})$ is the probability density which relates the measured quantities $\{\overrightarrow{k}\}$ to the parton quantities $\{\overrightarrow{p}\}$. $P(\{\overrightarrow{p}\} \mid \{\overrightarrow{k}\})$ is given by:

$$P(\{\overrightarrow{p}\} \mid \{\overrightarrow{k}\}) = \pi(\{\overrightarrow{p}\}) T(\overrightarrow{j_1} \mid \overrightarrow{p_1}) T(\overrightarrow{j_2} \mid \overrightarrow{p_2}) T(\overrightarrow{j_3} \mid \overrightarrow{p_3}) T(\overrightarrow{j_4} \mid \overrightarrow{p_4}) \tag{6.2}$$

where $T(\overrightarrow{k_i} \mid \overrightarrow{p_i})$ are transfer functions which relate the measured momentum of jet i, $\overrightarrow{k_i}$, to the momentum of parton i, $\overrightarrow{p_i}$, and $\pi(\{\overrightarrow{p}\})$ is the probability for observing a given $t\bar{t}$ parton-level final state. Note that there is no transfer function for the lepton as the uncertainty on the lepton

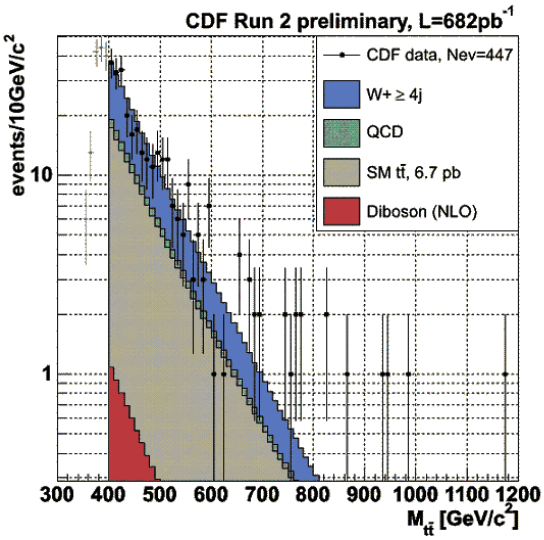

Figure 6.1: The distribution of $M_{t\bar{t}}$ obtained using the matrix element technique [39].

momentum is negligible compared to the uncertainty on the jet momentum. The unknown neutrino momentum is integrated out of the probability distribution, with no transfer function between missing energy and the neutrino momenta. $\pi(\{\overrightarrow{p}\})$ is given by:

$$\pi(\{\overrightarrow{p}\})d^3\overrightarrow{p_1}d^3\overrightarrow{p_2}d^3\overrightarrow{p_3}d^3\overrightarrow{p_4} = \frac{1}{\sigma}\int\int dx_i dx_j f_{i,p}(x_i,Q^2)f_{j,\overline{p}}(x_j,Q^2)d\hat{\sigma}_{ij}(ij \to t\bar{t}). \qquad (6.3)$$

$\pi(\{\overrightarrow{p}\})$ is a normalized differential cross section where the differential cross section is given by a convolution of the PDFs of the proton and anti-proton with the differential cross section of the underlying process, as discussed in Chapter 1. The cross section, and thus the probability for a particular final state, is given by the Standard Model matrix element for $t\bar{t}$ production and its subsequent decay, so this technique is known as a "matrix element" method.

This technique requires that jets be assigned to the underlying partons as the quantity $\pi(\{\overrightarrow{p}\})$ depends on the final state. All possible final state assignments to jets are computed, and the final probability distribution $P(M_{t\bar{t}} \mid \{\overrightarrow{k}\})$ is the sum of the probability distributions for each final state assignment. This distribution peaks near the true (partonic) value of $M_{t\bar{t}}$. The mean of the distribution is taken to be the reconstructed value of $M_{t\bar{t}}$ for the event. The resolution achieved is approximately 25 GeV/c^2 when the correct final state assignment is chosen.

With this technique for reconstructing $M_{t\bar{t}}$ for each event, distributions of $M_{t\bar{t}}$ for the Z' signal and Standard Model backgrounds, including $t\bar{t}$, are made from Monte Carlo simulations of the various processes. These distributions, or "templates," are compared to the distribution of $M_{t\bar{t}}$ in data. The data, along with the templates, is shown in Figure 6.1. The distribution is consistent with the SM expectation so limits are set on the cross section for Z' production as a function of Z' mass.

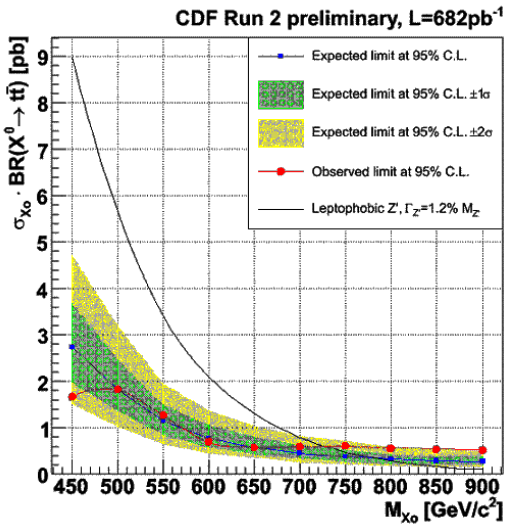

Figure 6.2: The observed and expected limits on Z' production obtained using the matrix element technique [39].

The probability that the data agrees with a Z' signal with cross section $\sigma_{Z'}$ is assessed using a likelihood technique. The likelihood, $\mathcal{L}(\overrightarrow{n} \mid \sigma_{Z'})$, is given by:

$$\mathcal{L}(\overrightarrow{n} \mid \sigma_{Z'}) = \prod_i \frac{e^{-\mu^i} \mu_i^{n_i}}{n_i!} \tag{6.4}$$

where

$$\mu_i = \sigma_{Z'} A_{Z'} T_{Z'i} + \sum_j N_j T_{ji}. \tag{6.5}$$

The subscript i runs over the bins; the subscript j runs over the SM backgrounds. $A_{Z'}$ gives the acceptance for the Z' signal and $T_{Z'i}$ (T_{ji}) is the content in the i^{th} bin of the normalized template for the Z' signal (SM backgrounds). With a flat prior for the signal cross section, $\mathcal{L}(\overrightarrow{n} \mid \sigma_{Z'})$ is the probability density for $\sigma_{Z'}$. Cross section limits are calculated at the 95% confidence level by integrating the likelihood up to 95% of the total area. The result is shown in Figure 6.2. Z' production is excluded at the 95% confidence level for leptophobic Z' with masses up to 725 GeV/c^2.

The second result from the CDF collaboration, using 955 pb^{-1} of integrated luminosity, was also published in 2008 [41]. Again the analysis method is based upon a technique developed for the top quark mass measurement [40].

The kinematics of the $t\bar{t}$ system are constrained to the SM decay $t\bar{t} \to W^+ b W^- \bar{b} \to q\overline{q'} b \ell \nu_\ell \bar{b}$ by

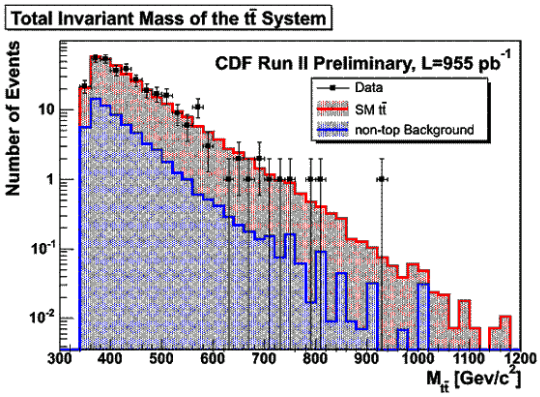

Figure 6.3: The distribution of $M_{t\bar{t}}$ obtained using the χ^2 reconstruction technique [41].

a χ^2 minimization. The χ^2 function is given by:

$$\chi^2 = \sum_i \frac{(p_T^{i,fit} - p_T^{i,meas})^2}{\sigma_i^2} + \frac{(M_{\ell\nu} - M_W)^2}{\Gamma_W^2} + \frac{(M_{jj} - M_W)^2}{\Gamma_W^2} + \frac{(M_{b\ell\nu} - M_{top})^2}{\Gamma_{top}^2} + \frac{(M_{bjj} - M_{top})^2}{\Gamma_{top}^2} \tag{6.6}$$

The quantity i runs over the physics objects in the events - the tight lepton, leading 4 jets, and the unclustered energy, a quantity that is related to the missing transverse energy. Their momenta are allowed to float within their measurement resolution. The invariant masses of the two W's are constrained to the invariant mass of the leptonic and hadronic decay products. The z-component of the neutrino momentum is a free parameter in the fit. The initial value of p_z^ν is set by solving the quadratic equation $M_W^2 = (p_\ell + p_\nu)^2$. A minimization is performed for each solution to the equation. The invariant masses of the two top quarks are constrained to the invariant mass of the Wb where the W decays either leptonically or hadronically. The χ^2 is minimized for each possible final state assignment of jets to quarks and each initial value of p_z^ν. In the analysis of M_{top}, the top mass is a free parameter in the fit. For the reconstruction of the invariant mass spectrum the top quark mass is constrained to 175 GeV/c^2. The invariant mass of the $t\bar{t}$ system is reconstructed from the four-momenta of the jets, leptons, and neutrino returned by the fit.

Using the above procedure to reconstruct $M_{t\bar{t}}$, templates are made for the Z' signal, and Standard Model and background processes. The $M_{t\bar{t}}$ distribution in data is compared to these templates in Figure 6.3. Again no significant discrepancy with the SM expectation is found, so limits are set on the Z' production cross section. The limits are set in the same manner as the matrix element analysis. The expected and observed limits are shown in Figure 6.4. A narrow leptophobic Z' is excluded at 95% confidence level for masses up to 720 GeV/c^2.

The DØ collaboration has also searched for narrow resonances in the $t\bar{t}$ lepton plus jets final state. The result has been submitted for publication with 1 fb^{-1} of data [42] and updated with 2 fb^{-1} of data [43].

The invariant mass reconstruction technique is much simpler in this case. Events with at least 3 tight jets are selected, where at least one jet has been identified by a b-tagging algorithm. The

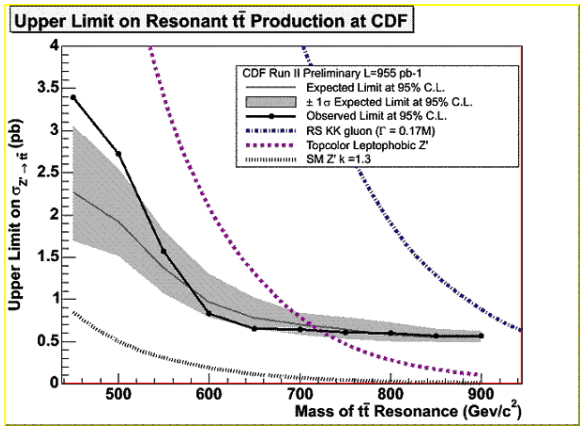

Figure 6.4: The observed and expected limits for a narrow Z'-like resonance obtained using the χ^2 reconstruction technique [41].

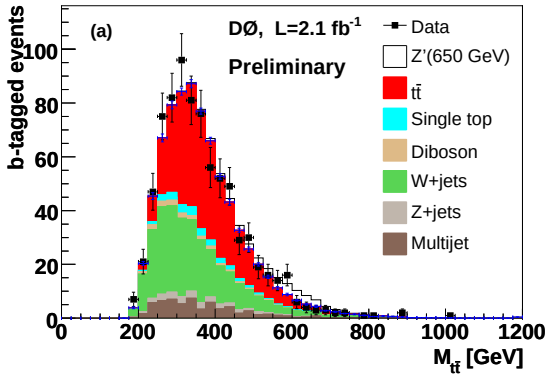

Figure 6.5: The distribution of $M_{t\bar{t}}$ obtained from reconstructed objects in events with 3 jets [43].

transverse momentum of the neutrino is given by the missing transverse energy in the event. The z-component of the neutrino momentum is given by the solution to the quadratic equation $M_W^2 = (p_\ell + p_\nu)^2$ which gives the smallest absolute value of p_z^ν. The $t\bar{t}$ invariant mass is given by the invariant mass of the lead jets (up to 4), the lepton and the neutrino. The $M_{t\bar{t}}$ distribution in data is compared to templates for a 650 GeV/c^2 narrow Z', $t\bar{t}$ and SM $t\bar{t}$ backgrounds for events with 3 jets and ≥ 4 jets in Figures 6.5 and 6.6, respectively.

No significant excess is observed in the 2.1 fb^{-1} of data analyzed so limits are set of Z' production. The limit-setting procedure is identical to the CDF analyses. A narrow leptophobic Z' is excluded at 95% confidence level for masses up to 760 GeV/c^2.

In summary, the CDF and DØ collaborations have performed searches for a narrow Z'-like resonance in the $t\bar{t}$ final state with up to 2 fb^{-1} of data. No significant discrepancy with SM $t\bar{t}$ production has been observed. A narrow Z'-like state with masses up to 760 GeV/c^2 is excluded at the 95% confidence level.

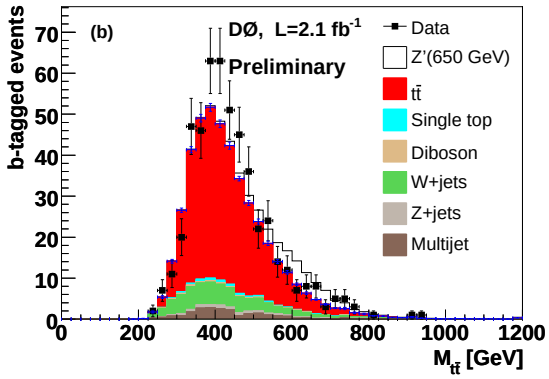

Figure 6.6: The distribution of $M_{t\bar{t}}$ obtained from reconstructed objects in events with 4 or more jets [43].

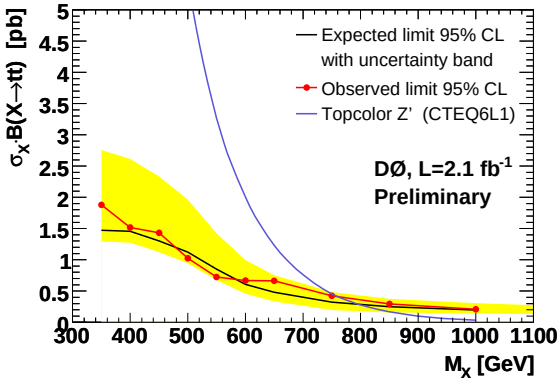

Figure 6.7: The observed and expected limits for a narrow Z'-like resonance obtained using reconstructed objects for $M_{t\bar{t}}$ [41].

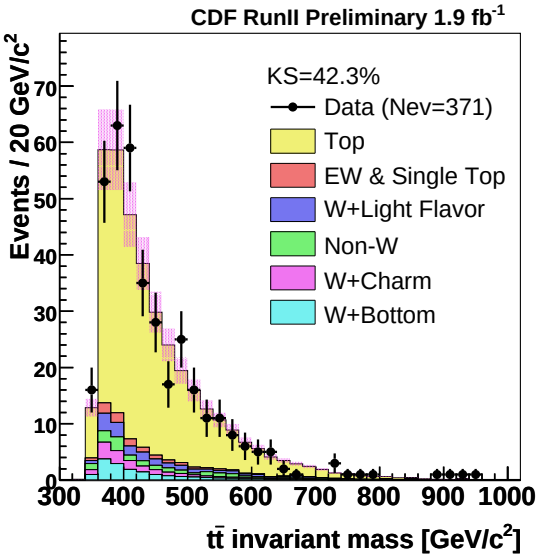

Figure 6.8: The distribution of $M_{t\bar{t}}$ obtained using a modified matrix element technique [44].

6.3 Search for Massive Gluons

For a signal which interferes with the Standard Model process, producing potentially broad resonances and distortions, the limits described above for narrow width resonances do not apply because the Poisson binned likelihood is not sensitive to excesses or deficits which are spread over a large number of bins.

CDF has completed a search for a massive color octet resonance - for example, a coloron or massive gluon as described in Section 1.4 - in 1.9 fb^{-1} of data [44]. The search included resonances with masses from 400 to 800 GeV/c^2 and widths of $0.05 \cdot M$ to $0.50 \cdot M$. The invariant mass reconstruction scheme is based on the matrix element technique used in [39] and [38]. However, the constraint to the $t\bar{t}$ matrix element was released to maximize sensitivity to beyond the Standard Model physics processes. In other words, the term $\pi(\{\overrightarrow{p}\})$ in Equation 6.2 is set equal to one. The measured invariant using this reconstruction technique is compared to the SM expectation in Figure 6.8.

An unbinned likelihood is used to compare the reconstructed $M_{t\bar{t}}$ distribution in data to the templates for the SM $t\bar{t}$ and background processes and color octet resonances with various couplings to quarks. The likelihood function is given by:

$$\mathcal{L} = \mathcal{L}_{shape} \times \mathcal{L}_{Nevts} \times \mathcal{L}_{Bkg}. \tag{6.7}$$

Most of the information comes from the term $\mathcal{L}_{shape}$:

$$\mathcal{L}_{shape} = \prod_{n=1}^{N} \frac{n_{sig} P_{sig}(M_{t\bar{t}}; \lambda) + n_{bkg} P_{bkg}(M_{t\bar{t}})}{n_{sig} + n_{bkg}} \tag{6.8}$$

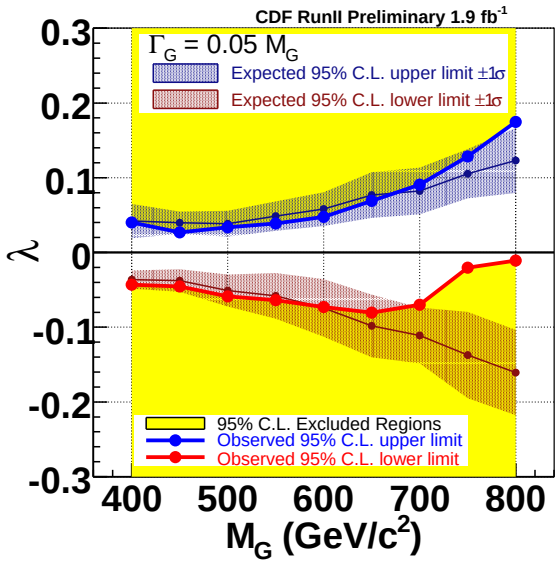

Figure 6.9: The 95% confidence level limits for narrow color octet resonances [44].

where λ is the color octet resonance coupling. This term gives the probability that an event comes from either a resonance or SM background. The term $\mathcal{L}_{Nevts}$ is a Poisson term:

$$\mathcal{L}_{Nevts} = \frac{e^{-(n_{sig}+n_{bkg})}(n_{sig}+n_{bkg})^N}{N!}. \tag{6.9}$$

The term $\mathcal{L}_{Bkg}$ constrains the background (including $t\bar{t}$) to the SM expectation, n_{bkg}^{SM}, with uncertainty σ_{SM}:

$$\mathcal{L}_{Bkg} = exp(-\frac{(n_{bkg}-n_{bkg}^{SM})^2}{2\sigma_{SM}^2}). \tag{6.10}$$

The fitted value of λ is consistent with the SM expectation of zero for the entire region of resonance masses and widths explored. Limits are set by assuming a flat prior distribution for λ and integrating the likelihood to 95% of the area. The resulting limits as a function of mass for a narrow resonance are shown in Figure 6.9 and for a wide resonance in Figure 6.10.

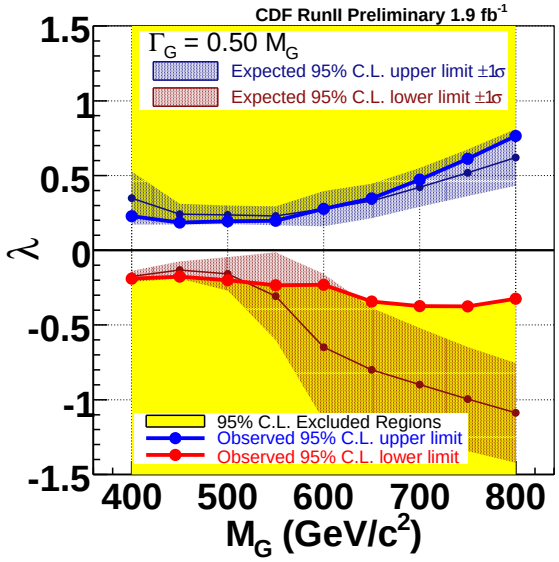

Figure 6.10: The 95% confidence level limits for wide color octet resonances [44].

Chapter 7

Analysis Method

7.1 Introduction

In Chapter 6 I reviewed the various techniques that have been utilized to study the $M_{t\bar{t}}$ spectrum. Most of these techniques were borrowed from analyses of the top quark mass. These methods achieve high resolution by constraining the kinematics of the final state to the kinematics of the lepton+jets decay of the $t\bar{t}$ pair. While a higher resolution on $M_{t\bar{t}}$ lends to stricter limits on physics beyond the SM, it is important to not over-constrain the system with an algorithm that makes every input look like the SM. Over-constraining also depends somewhat on the model of interest - a more subtle distortion to the SM from a massive gluon, for instance, requires more consideration than a strong peak from a Z'. For example, the search for a massive color octet resonance described in Section 6.3 did not employ the constraint to the SM matrix element that the narrow resonance search based on the same technique used.

At the same time that over-constraining the $t\bar{t}$ system is a concern, it is also important to consider the interpretation of results. In general the raw $M_{t\bar{t}}$ distribution that is obtained from the four-momenta of the physics objects of the event is detector-dependent in the sense that the resolution of objects is detector-specific. Especially if a significant distortion to the expected $M_{t\bar{t}}$ spectrum is found, a detector-dependent $M_{t\bar{t}}$ spectrum will be very difficult to interpret theoretically [45]. For example, Figure 7.1 shows a 2-dimensional histogram of $M_{t\bar{t}}^{true}$ versus the reconstructed $M_{t\bar{t}}$ as defined in Section 4.4. Generally values of $M_{t\bar{t}}$ correspond to values near $M_{t\bar{t}}^{true}$, but there is also significant spread. If a resonance is found in the region of $M_{t\bar{t}} = 600$ GeV/c^2, it could be coming from values of $M_{t\bar{t}}^{true}$ from 400 to 950 GeV/c^2. The quality of jet reconstruction and missing energy reconstruction in particular determine the degree of migration from $M_{t\bar{t}}^{true}$ to $M_{t\bar{t}}$, and those quantities are detector-dependent.

The challenge of $M_{t\bar{t}}$ reconstruction is to balance the need for a meaningful partonic-level measurement with the desire to maintain sensitivity to physics beyond the SM. I use an unfolding technique which constrains the $t\bar{t}$ system to the extent that the bin migration from $M_{t\bar{t}}^{true}$ true bin j to $M_{t\bar{t}}$ bin i in the Monte Carlo simulation is assumed to be accurate and the true underlying distribution does not differ wildly from the SM distribution. This technique is complementary to those described in Chapter 6. The $M_{t\bar{t}}$ distribution is corrected to $M_{t\bar{t}}^{true}$, so the results can be easily compared to theoretical predictions for various beyond the SM physics processes.

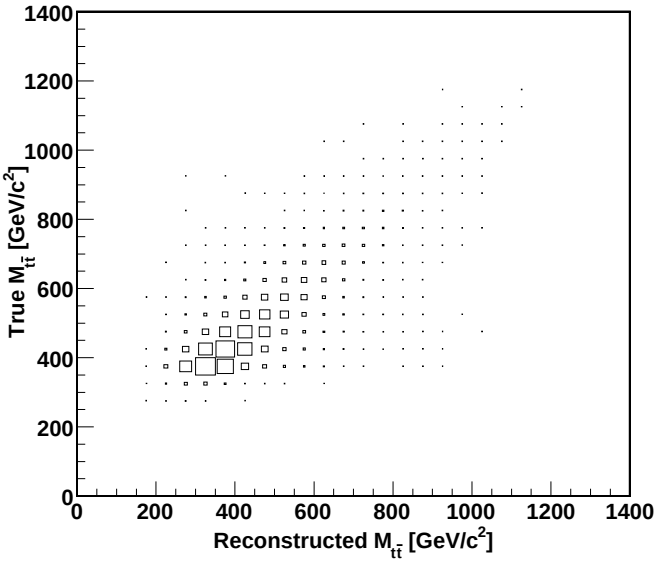

Figure 7.1: True $M_{t\bar{t}}$ versus reconstructed $M_{t\bar{t}}$ in $t\bar{t}$ Monte Carlo simulation.

7.2 Unfolding

The reconstructed $M_{t\bar{t}}$ distribution, $g(M_{t\bar{t}})$, can be expressed as the convolution of $M_{t\bar{t}}^{true}$ with a detector response function, $\mathcal{A}(M_{t\bar{t}}, M_{t\bar{t}}^{true})$:

$$g(M_{t\bar{t}}) = \int dM_{t\bar{t}}^{true}\ \mathcal{A}(M_{t\bar{t}}, M_{t\bar{t}}^{true}) f(M_{t\bar{t}}^{true}). \tag{7.1}$$

The goal of unfolding is to invert the function $\mathcal{A}(M_{t\bar{t}}, M_{t\bar{t}}^{true})$ in order to obtain $f(M_{t\bar{t}}^{true})$ from $g(M_{t\bar{t}})$. Because I observe discrete events in various bins of $M_{t\bar{t}}$, the problem is better formulated in terms of these discrete values. This formulation is taken from Reference [48]. Let x represent a vector of $M_{t\bar{t}}^{true}$ values in n_x bins with bin boundaries $M_{t\bar{t}}^{true,j}, j = 1, ..., n_x - 1$. The components x_j are given by:

$$x_j = \int_{M_{t\bar{t}}^{true,j-1}}^{M_{t\bar{t}}^{true,j}} dM_{t\bar{t}}^{true}\ f(M_{t\bar{t}}^{true}). \tag{7.2}$$

Similarly, let b represent a vector of $M_{t\bar{t}}$ values in n_b bins with boundaries $M_{t\bar{t}}^{j}, j = 1, ..., n_b - 1$. The components of b_j are given by:

$$b_j = \int_{M_{t\bar{t}}^{j-1}}^{M_{t\bar{t}}^{j}} dM_{t\bar{t}}\ g(M_{t\bar{t}}). \tag{7.3}$$

The detector response function $\mathcal{A}(M_{t\bar{t}}, M_{t\bar{t}}^{true})$ relates the true and measured distributions:

$$g(M_{t\bar{t}}) = \int_{M_{t\bar{t}}^{true,0}}^{M_{t\bar{t}}^{true,n_x}} dM_{t\bar{t}}^{true} \mathcal{A}(M_{t\bar{t}}, M_{t\bar{t}}^{true}) f(M_{t\bar{t}}^{true}). \tag{7.4}$$

From Equation 7.4 it follows that a response matrix A with entries A_{ij} may be written as:

$$A_{ij} = \frac{\int_{M_{t\bar{t}}^{i-1}}^{M_{t\bar{t}}^{i}} dM_{t\bar{t}} \int_{M_{t\bar{t}}^{true,j-1}}^{M_{t\bar{t}}^{true,j}} dM_{t\bar{t}}^{true}\ \mathcal{A}(M_{t\bar{t}}, M_{t\bar{t}}^{true}) f(M_{t\bar{t}}^{true})}{\int_{M_{t\bar{t}}^{true,j-1}}^{M_{t\bar{t}}^{true,j}} dM_{t\bar{t}}^{true}\ f(M_{t\bar{t}}^{true})}. \tag{7.5}$$

Now the problem I wish to solve is the matrix equation:

$$Ax = b. \tag{7.6}$$

Equation 7.6 is easily solved if the matrix A may be inverted. However, there is no guarantee that A can be inverted, and, furthermore, that the inversion will make sense - *i.e.* lead to a sensible vector x with non-negative values. The problems of the inversion can be traced to the inevitable statistical fluctuations present in both the measured vector b and the Monte Carlo model used to produce A. There are many techniques available to suppress these fluctuations [48, 49, 50]. I choose the Singular Value Decomposition (SVD) method [48] of data unfolding because the algorithm is linear and easy to implement. The example in Section 7.2.1 and the algorithm description follow Reference [48].

7.2.1 A Simple Example

The SVD of a real $m \times n$ matrix A is a factorization of the form:

$$A = USV^T \tag{7.7}$$

where U is an $m \times m$ orthogonal matrix, V is an $n \times n$ orthogonal matrix, and S is an $m \times n$ diagonal matrix with non-negative entries. The diagonal entries of S, s_i, are the "singular values" of S. For a degenerate matrix, at least one singular value will be zero and the number of non-zero singular values is equal to the rank of the system. When some singular values of A are small in comparison with others, the system becomes ill-behaved and must be "regularized" in order to obtain a sensible solution.

The following simple example with a 2×2 detector response matrix illustrates both how SVD is used for unfolding and the need for regularization.

The response matrix A has the form:

$$A = \frac{1}{2} \begin{pmatrix} 1+\epsilon & 1-\epsilon \\ 1-\epsilon & 1+\epsilon \end{pmatrix} \tag{7.8}$$

where $0 \leq \epsilon \leq 1$. A perfect detector would have $\epsilon = 1$ while a very poor detector would have $\epsilon \ll 1$ - the extreme case of $\epsilon = 0$ would indicate a detector which cannot distinguish between events in the two bins. The vector of measured events, b, is given by:

$$b = \begin{pmatrix} b_1 \\ b_2 \end{pmatrix}. \tag{7.9}$$

The vector b has only statistical uncertainties so its covariance matrix, B, is given by:

$$B = \begin{pmatrix} b_1 & 0 \\ 0 & b_2 \end{pmatrix}. \tag{7.10}$$

The vector of true events, x, is given by:

$$x = \begin{pmatrix} x_1 \\ x_2 \end{pmatrix}. \tag{7.11}$$

Performing an SVD decomposition, Equation 7.7, on A leads to the following U and V matrices:

$$U = V = \frac{1}{\sqrt{2}} \begin{pmatrix} 1 & 1 \\ 1 & -1 \end{pmatrix} \tag{7.12}$$

and matrix S, with singular values 1 and ϵ:

$$S = \begin{pmatrix} 1 & 0 \\ 0 & \epsilon \end{pmatrix}. \tag{7.13}$$

Now Equation 7.4 can be rewritten in terms of the U,V, and S matrices as:

$$USV^T x = b. \tag{7.14}$$

Equation 7.14 may be diagonalized by multiplying on the left by U^T to give:

$$Sz = d \tag{7.15}$$

where

$$z \equiv V^T x = \frac{1}{\sqrt{2}} \begin{pmatrix} x_1 + x_2 \\ x_1 - x_2 \end{pmatrix}, d \equiv U^T b = \frac{1}{\sqrt{2}} \begin{pmatrix} b_1 + b_2 \\ b_1 - b_2 \end{pmatrix}. \tag{7.16}$$

Note that the matrix S is trivially inverted by replacing the diagonal entries s_i with $1/s_i$. Now we have:

$$z = V^T x = S^{-1} d. \tag{7.17}$$

Multiplying on the left by V leads to the solution:

$$x = Vz = VS^{-1}d = VS^{-1}U^T b = A^{-1}b = \frac{b_1 - b_2}{2\epsilon}\begin{pmatrix} 1 \\ -1 \end{pmatrix} + \frac{b_1 + b_2}{2}\begin{pmatrix} 1 \\ 1 \end{pmatrix}. \tag{7.18}$$

The original matrix equation $Ax = b$ has been solved by rotating both the left and right side to form a diagonal system, Equation 7.15, with a matrix S that can be easily inverted.

7.2.2 The Need for Regularization

The solution given in Equation 7.18 is reasonable if ϵ is not too small and all elements of d, given by Equation 7.16 are statistically significant. The covariance matrix for d is given by:

$$D = U^T BU = \frac{1}{2}\begin{pmatrix} b_1 + b_2 & b_1 - b_2 \\ b_1 - b_2 & b_1 + b_2 \end{pmatrix}. \tag{7.19}$$

Now if $b_1 - b_2$ is not statistically significant - $(b_1 - b_2)^2 \leq b_1 + b_2$ - the covariance matrix D is approximately diagonal. Equation 7.15 gives:

$$1 \cdot z_1 = \frac{b_1 + b_2}{2} \pm \sqrt{\frac{b_1 + b_2}{2}} \tag{7.20}$$

and

$$\epsilon \cdot z_2 = \frac{b_1 - b_2}{2} \pm \sqrt{\frac{b_1 + b_2}{2}} \tag{7.21}$$

where the uncertainty on the right hand side is from the covariance matrix D. Equation 7.21 simply does not make sense when ϵ is small and the difference $b_1 - b_2$ is statistically insignificant. Furthermore, the rotation of z back to the desired vector x according to Equation 7.18 causes the problematic z_2 term to contribute large spurious terms to both components of x. Again, this has occurred because ϵ is small and the vector b is subject to large uncertainties. In this case the matrix A has insufficient rank and the system of equations is over-determined.

Suppressing the fluctuation caused by z_2 is called "regularization" of the solution. In order to do this, z_2 must be determined from some *a priori* condition. A reasonable *a priori* condition here is that $\|x\|^2$ - the Euclidean norm of the vector x - is minimized. This is achieved by setting z_2=0, leading to the following regularized solution for x:

$$x^{reg} = \frac{b_1 + b_2}{2}\begin{pmatrix} 1 \\ 1 \end{pmatrix} \tag{7.22}$$

7.2.3 Regularized Unfolding

The solution or the matrix equation $Ax = b$ is also the solution to the following least squares problem:

$$(b - Ax)^T(b - Ax) \equiv \|r\|^2 = min. \tag{7.23}$$

In regularizing the solution I seek to reduce the number of vectors x which minimize the norm of the residual vector r to eliminate unphysical or unreasonable solutions to the problem. There are many techniques utilized to address this problem [51]. Regardless of the approach taken, it is necessary to have in hand some *a priori* condition which defines what constitutes a reasonable solution. My *a priori* condition will be that the the $M_{t\bar{t}}^{true}$ spectrum is well-described by the Monte Carlo simulation.

In order to impose this condition Equation 7.6 is recast in the following form:

$$A'w = b. \tag{7.24}$$

The elements of the new detector response matrix A' are given by:

$$A'_{ij} = N_{events}^{ij} \tag{7.25}$$

where N_{events}^{ij} represents the number of events generated in bin j that are measured in bin i. The elements of this matrix are easily generated from Monte Carlo events by forming the 2-dimensional distribution of true versus measured quantities, in this analysis $M_{t\bar{t}}$. The new unknown vector w is given by:

$$w_j = \frac{x_j}{x_j^{ini}}. \tag{7.26}$$

This vector measures the deviation from the input true distribution, generated from Monte Carlo events. The unfolding procedure will solve for the vector w, from which the desired vector x can be found simply according to:

$$x_j = w_j x_j^{ini}. \tag{7.27}$$

The *a priori* condition is that the vector w is reasonably smooth.

Recasting A in the form of A' is also beneficial for determining the effective rank of the system. Again, the elements A'_{ij} are determined by producing a 2-D distribution of $M_{t\bar{t}}^{true}$ versus $M_{t\bar{t}}$. Bins in the tails of this distribution are poorly populated and subject to large statistical fluctuations. For the probability detector response matrix A, that could lead to an entry $A_{ij} = 1$ with a very large statistical uncertainty - 100% if the bin contained only one entry. Conversely, well-populated bins would have entries $A_{ij} < 1$ with small uncertainties. The equations with the largest statistical uncertainty would be given the largest weight, which leads to the same problems as the small ϵ discussed above - over-determined equations from a matrix with insufficient rank.

It is also useful to transform the least squares problem of Equation 7.23 to the weighted least squares problem:

$$(b - A'w)B^{-1}(b - A'w) \equiv \|\widetilde{r}\|^2 = min. \tag{7.28}$$

By rescaling each equation in the system by the uncertainty on the vector b, each equation will have equal importance. If the covariance matrix B is not diagonal a rotation is first performed on the left and right hand sides of Equation 7.24. The procedure is as follows:

- Perform an SVD on the covariance matrix B. The SVD on the covariance matrix B yields[1]:

$$B = QRQ^T, R_{ii} \equiv r_i^2 \neq 0, R_{ij} = 0, i \neq j. \tag{7.29}$$

- Rotate and rescale the matrix A' and vector b of Equation 7.24 to the new matrix $\widetilde{A}$ and $\widetilde{b}$ defined by:

$$\widetilde{A}_{ij} = \frac{1}{r_i} \sum_m Q_{im} A_{mj}, \widetilde{b}_i = \frac{1}{r_i} \sum_m Q_{im} b_m. \tag{7.30}$$

Now the equation to be solved is:

$$\widetilde{A}w = \widetilde{b}, \tag{7.31}$$

or equivalently:

$$(b - \widetilde{A}w)^T (b - \widetilde{A}w) = min. \tag{7.32}$$

Regularization is achieved by adding a regularization term, τ, to the weighted least squares Equation 7.32:

$$(b - \widetilde{A}w)(b - \widetilde{A}w) + \tau (Cw)^T Cw = min. \tag{7.33}$$

The matrix C enforces the *a priori* condition on w, with an adjustable strength given by the value of τ. To enforce the smoothness of w the matrix C is a minimum curvature matrix, with the curvature of w given by the sum of squares of its the second derivatives:

$$\sum_i [(w_{i+1} - w_i) - (w_i - w_{i-1})]^2 \tag{7.34}$$

with the form:

$$C = \begin{pmatrix} -1+\xi & 1 & 0 & 0 & ... \\ 1 & -2+\xi & 1 & 0 & ... \\ 0 & 1 & -2+\xi & 1 & ... \\ ... & 0 & 1 & -2+\xi & 1 \\ ... & ... & 0 & 1 & -1+\xi \end{pmatrix} \tag{7.35}$$

where ξ is a small - $\sim 10^{-3}$ - term which insures that C may be inverted. Now the problem may be formulated in terms of a damped least squares problem:

$$\begin{pmatrix} \widetilde{A}C^{-1} \\ \sqrt{\tau} I \end{pmatrix} Cw = \begin{pmatrix} \widetilde{b} \\ 0 \end{pmatrix}. \tag{7.36}$$

For the case $\tau = 0$, or no regularization, the problem is solved as in Section 7.2.1 with the substitutions $A \rightarrow \widetilde{A}C^{-1}$ and $x \rightarrow Cw$ in Equation 7.6. An SVD is performed on the product $\widetilde{A}C^{-1}$ to give:

$$\widetilde{A}C^{-1} = USV^T, S_{ii} = s_i, S_{ij} = 0, i \neq j. \tag{7.37}$$

[1]The SVD of B has this form because it is a positive definite, symmetric matrix

Now the diagonal system, Equation 7.15, is solved with:

$$d \equiv U^T \widetilde{b},\ z \equiv V^T C w \tag{7.38}$$

to give:

$$z_i = d_i / s_i. \tag{7.39}$$

Finally, the vector w is found by multiplying Equation 7.38 on the left by the product $C^{-1}V$:

$$w = C^{-1} V z \tag{7.40}$$

and w and the underlying distribution vector x are related according to Equation 7.27.

For $\tau > 0$ the solution is found by multiplying Equation 7.36 by Givens rotation matrices [51]. The vectors d and z of Equation 7.38 are replaced by regularized vectors d^τ and z^τ, defined by:

$$d_i^\tau \equiv d_i \frac{s_i^2}{s_i^2 + \tau}, z_i^\tau \equiv \frac{d_i s_i}{s_i^2 + \tau}. \tag{7.41}$$

Equation 7.40 becomes:

$$w^\tau = C^{-1} V z^\tau. \tag{7.42}$$

The regularized x vector is given by:

$$x^\tau = x_i^{ini} w_i^\tau. \tag{7.43}$$

The covariance matrices for w^τ, z^τ and x^τ - W^τ, Z^τ and X^τ, respectively - are given by:

$$W^\tau = C^{-1} V Z^\tau V^T C^{T-1}, \tag{7.44}$$

$$Z_{ik}^\tau = \frac{s_i^2}{(s_i^2 + \tau)^2} \delta_{ik}, \tag{7.45}$$

and

$$X_{ik}^\tau = x_i^{ini} W_{ik}^\tau x_k^{ini}. \tag{7.46}$$

7.2.4 Choosing the Regularization Parameter

In Section 7.2.2 I showed how regularization is needed if not all elements of d are statistically significant. It follows then that the regularization parameter can be determined by examining the values of d_i as given by Equation 7.38. In particular, plotting d_i, or $log(d_i)$ versus i will show some values of d_i for $i < k$ are large and statistically significant, while for $i > k$ the values are small and randomly distributed. This indicates that the system has only k statistically significant equations, or in other words, that the effective rank of the detector response matrix, A, is k. The regularization parameter τ is set to the square of the k^{th} singular value of the matrix $\widetilde{A}C^{-1}$ (see Equation 7.37):

$$\tau = s_k^2. \tag{7.47}$$

7.2.5 Algorithm Summary

In summary, the algorithm for SVD unfolding proceeds in a series of steps with no loop:

1. Define the number of bins and bin boundaries for the distribution. I set the number of bins in the true and reconstructed distributions to be equal, $n_b = n_x = n$.
2. Build the second derivative matrix C, according to Equation 7.35 and calculate its inverse.
3. Build the detector response matrix A' according to Equation 7.25 and the vector x^{ini}, the input true distribution, from a Monte Carlo simulation.
4. Determine the vector b and its associated covariance matrix B from the data.
5. Rotate and rescale the matrix A' and the vector b according to Equations 7.29 and 7.30.
6. Perform an SVD on the product $\widetilde{A}C^{-1}$ according to Equation 7.37.
7. Rotate the vector $\widetilde{b}$ to the vector d according to Equation 7.38.
8. Determine the effective rank of the system from a plot of $log|d_i|$ versus i.
9. Set the regularization parameter τ according to Equation 7.47.
10. Calculate the vectors z^τ, w^τ and their covariances matrices according to Equations 7.41, 7.44 and 7.45.
11. Finally calculate the unfolded x^τ vector according to Equation 7.43 and its covariance matrix according to Equation 7.46.

7.2.6 Implementing the Algorithm

I follow the algorithm as outlined in Section 7.2.5 to write a `C++` implementation of the SVD unfolding algorithm. The algorithm is meant to function inside of `ROOT` and uses the `ROOT` library `TDecompSVD` in order to perform the singular value decomposition of the relevant matrices. The code is publicly available [52].

7.2.7 Unfolding the $M_{t\bar{t}}$ Distribution

I first test the unfolding of the $M_{t\bar{t}}$ distribution in the absence of background. I create a pseudo-data distribution of reconstructed $t\bar{t}$ invariant masses by fluctuating the reconstructed distribution in the Monte Carlo simulation. The $t\bar{t}$ content is normalized to that observed in the data. I then proceed with the steps outlined in Section 7.2.5.

The effective rank of the system is set by examining the logarithm of elements of the vector d versus i as shown in Figure 7.2. Based on Figure 7.2 the effective rank of the system, k, is set to 4. The choice of 4 is somewhat arbitrary - choosing $k = 3$ or $k = 5$ will produce similar results. However, choosing k much too small or much too large will cause over- or under-regularization. The unfolded distribution with $k = 4$ compared to the truth information, is shown in Figure 7.3. If I set

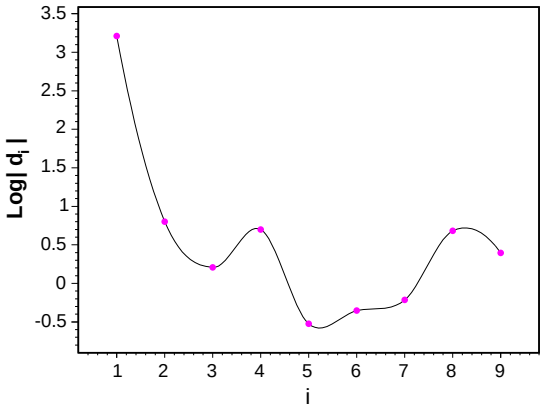

Figure 7.2: The logarithm of the elements of d, as defined in Equation 7.38 versus i.

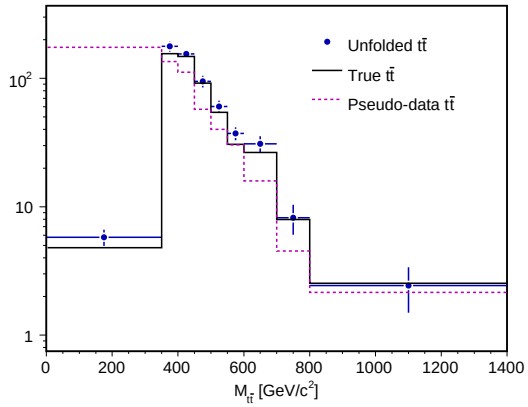

Figure 7.3: The unfolded distribution, with $k = 4$, as compared to the true distribution.

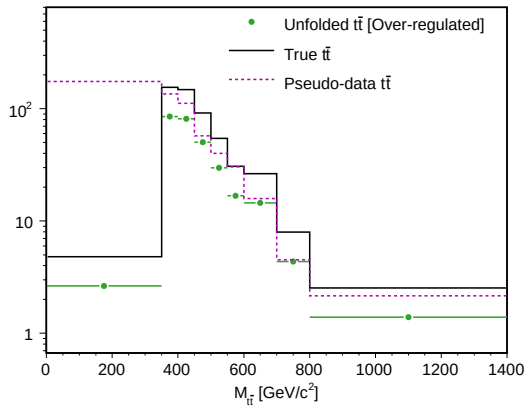

Figure 7.4: The unfolded distribution, with $k = 1$, as compared to the true distribution. The solution is over-regulated.

$k = 1$ the system is over-regularized. This distribution is shown in Figure 7.4. Over-regularization forces the solution to be the input Monte Carlo truth distribution times an overall constant regardless of the shape of the data. If I set the effective rank of the system too high the system will be under-regulated. The resulting unfolded distribution is compared to the true distribution in Figure 7.5. If this case the elements of the vector w vary wildly, where some elements are negative. This is the type of solution that would result from using no regularization.

In order to further test the procedure, I perform several thousand pseudo-experiments, fluctuating to a new pseudo-data set each time and checking the accuracy of the unfolded distributions. For each pseudo-experiment, the regularization is set by $k = 4$. I form the pull distribution in each of the 9 bins of $M_{t\bar{t}}$:

$$pull = (N^i_{unfold} - N^i_{true})/\sigma_{N^i_{unfold}} \tag{7.48}$$

where N^i_{unfold} is the number of events in each bin i after unfolding, N^i_{true} is the number of events in the true Monte Carlo distribution and $\sigma_{N^i_{unfold}}$ is the uncertainty on N^i_{unfold} from the covariance matrix of the unfolded vector of events.[2] If the procedure is unbiased and the uncertainties are accurate the pull should be a unit Gaussian with mean 0 and width 1. The mean and width of the pulls in each bin are given in Table 7.1. The means and widths are consistent with 0 and 1, within $2 \cdot \sigma$ of the their respective uncertainties, in each bin of $M_{t\bar{t}}$. So the unfolding procedure, at least with signal-only, is unbiased and returns accurate uncertainties.

7.3 Calculating $d\sigma/dM_{t\bar{t}}$

The differential cross section, as given in Equation 5.6, is calculated as follows:

1. Subtract from the data in each bin of the measured $M_{t\bar{t}}$ distribution the expected number of

[2]The uncertainty for bin i is given by the square root of the ii element (diagonal element of row i) of the matrix.

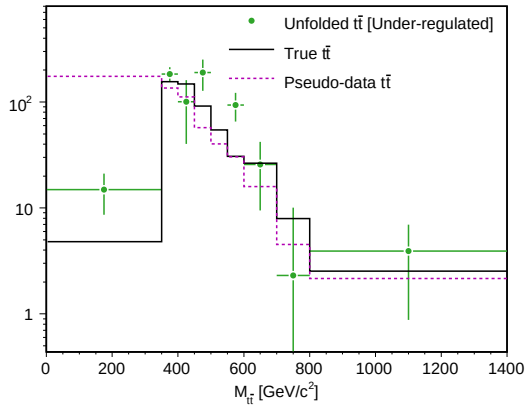

Figure 7.5: The unfolded distribution, with $k = 8$, as compared to the true distribution. The solution is under-regulated.

$M_{t\bar{t}}$ [GeV/c^2]	Pull Mean	Pull Width
0-350	0.02 ± 0.02	0.98 ± 0.01
350-400	0.02 ± 0.02	0.99 ± 0.01
400-450	0.02 ± 0.02	0.99 ± 0.01
450-500	-0.02 ± 0.02	0.99 ± 0.01
500-500	-0.03 ± 0.02	1.00 ± 0.01
550-600	-0.02 ± 0.02	1.02 ± 0.01
600-700	0.00 ± 0.02	1.01 ± 0.01
700-800	0.01 ± 0.02	0.99 ± 0.01
800-1400	0.01 ± 0.02	0.99 ± 0.01

Table 7.1: The mean and widths of the pull for the number of unfolded events in each bin, as defined in Equation 7.48, for pseudo-experiments constructed with $t\bar{t}$ signal only.

background events, N^i_{bkg} according to the $M_{t\bar{t}}$ distribution of the SM background processes, as in Table 5.3 and Figure 5.3.

2. Feed the vector of $t\bar{t}$ events reconstructed in each bin to the unfolding algorithm.

3. Divide the number of events in each bin after unfolding, N^i_{unfold}, by the appropriate denominator to obtain $d\sigma/dM_{t\bar{t}}$. The denominator in each bin is the product of the selection efficiencies in Table 4.8 with the integrated luminosity and the bin width. The complete denominators are given in Table 7.2.

$M_{t\bar{t}}$ [GeV/c^2]	CEM	CMUP	CMX	ALL
Denominator without bin width [pb^{-1}]				
$\leq$ 350	23.55 ± 1.49	13.64 ± 1.00	6.10 ± 0.42	43.30 ± 1.84
350-400	35.06 ± 2.22	18.74 ± 1.37	9.03 ± 0.62	62.83 ± 2.69
400-450	39.23 ± 2.49	20.99 ± 1.54	9.87 ± 0.68	70.10 ± 3.00
450-500	41.11 ± 2.61	22.41 ± 1.64	10.15 ± 0.70	73.66 ± 3.16
500-550	43.41 ± 2.75	23.51 ± 1.72	11.03 ± 0.76	77.95 ± 3.33
550-600	44.30 ± 2.81	24.13 ± 1.77	10.95 ± 0.76	79.37 ± 3.40
600-700	44.64 ± 2.83	23.94 ± 1.75	11.52 ± 0.79	80.10 ± 3.42
700-800	45.35 ± 2.87	22.83 ± 1.67	10.83 ± 0.75	79.02 ± 3.41
800-1400	35.91 ± 2.28	18.27 ± 1.34	8.46 ± 0.58	62.64 ± 2.70
All bins	38.88 ± 2.46	20.91 ± 1.53	9.83 ± 0.68	69.61 ± 2.98
Final Denominator with bin width[GeV/c^2pb^{-1}]				
$\leq$ 350	8243.09 ± 522.54	4773.64 ± 349.50	2136.74 ± 147.46	15153.47 ± 645.71
350-400	1752.87 ± 111.12	937.03 ± 68.60	451.74 ± 31.17	3141.64 ± 134.26
400-450	1961.66 ± 124.35	1049.43 ± 76.83	493.72 ± 34.07	3504.81 ± 150.09
450-500	2055.31 ± 130.29	1120.29 ± 82.02	507.39 ± 35.01	3682.99 ± 157.89
500-550	2170.41 ± 137.58	1175.41 ± 86.06	551.59 ± 38.06	3897.41 ± 166.69
550-600	2215.06 ± 140.41	1206.40 ± 88.33	547.28 ± 37.77	3968.73 ± 170.13
600-700	4463.80 ± 282.96	2393.89 ± 175.27	1151.88 ± 79.49	8009.58 ± 342.21
700-800	4535.28 ± 287.50	2283.35 ± 167.17	1083.06 ± 74.74	7901.69 ± 340.86
800-1400	21545.67 ± 1365.82	10959.70 ± 802.42	5077.75 ± 350.43	37583.12 ± 1622.38

Table 7.2: Denominator in bins of $M_{t\bar{t}}$, assuming 2.7 fb^{-1} of data.

I check this full procedure by again performing pseudo-experiments, where the pseudo-data distribution is formed for each experiment by fluctuating both the expected signal and background distributions from Monte Carlo simulation. In each experiment, I perform the steps outlined above. First, the expected background in each bin is subtracted from the pseudo-data $M_{t\bar{t}}$ distribution. Next, I unfold with regularization set by $k = 4$. Now the input covariance matrix for the unfolding procedure includes both the uncertainty on the background content in each bin in addition to the Poisson uncertainty on the number of events reconstructed in each bin.[3] I again check the pull distribution in each bin - the results are given in Table 7.3. The pull widths that are less than 1 in several bin indicate that there is a slight over-estimation of the uncertainty in those bins. However, this is about a 5% effect and I do not correct for it. The pull means are shifted from zero by greater than $2 \cdot \sigma$ in several bins. This would be a cause for concern if the shift would cause a significant

[3]The input covariance matrix is diagonal. The ii element is given by the quadrature sum of uncertainty on the number of background events in bin i and the Poisson uncertainty on the reconstructed events in each bin.

difference in the value of $d\sigma/dM_{t\bar{t}}$ in that bin. However, this is not case - with a large number of events expected in most bins the effect on the final cross section is negligible with respect to the statistical uncertainty. The exception is in the last two bins, where less than 10 events are expected in each bin. However this shift is explained by the positive tail on the Poisson distribution for a number of events with a small mean.

$M_{t\bar{t}}$ [GeV/c^2]	Pull Mean	Pull Width
0-350	-0.01 ± 0.02	0.93 ± 0.01
350-400	0.03 ± 0.02	0.96 ± 0.01
400-450	0.04 ± 0.02	1.01 ± 0.01
450-500	0.05 ± 0.02	0.95 ± 0.01
500-550	-0.02 ± 0.02	0.98 ± 0.01
550-600	-0.06 ± 0.02	1.02 ± 0.01
600-700	-0.03 ± 0.02	1.03 ± 0.01
700-800	0.05 ± 0.02	0.99 ± 0.01
800-1400	0.09 ± 0.02	0.97 ± 0.01

Table 7.3: The mean and widths of the pull for the number of unfolded events in each bin, as defined in Equation 7.48, for pseudo-experiments constructed with both signal and background events.

The results from data will be given in Chapter 10. First, I will discuss the various systematic uncertainties which affect the result and how these are evaluated in the next chapter.

Chapter 8

Systematic Uncertainties

8.1 Introduction

Systematic uncertainties arise from uncertainties in the Monte Carlo modeling of the $M_{t\bar{t}}$ shape in signal and background, modeling of the acceptance, the estimation of the data sample composition and the uncertainty on the integrated luminosity of the data sample. The effect of these uncertainties on the cross section measurement is assessed by varying the Monte Carlo model in pseudo-experiments.

8.2 Sources of Uncertainty

Most uncertainties affect both the shape of the reconstructed $M_{t\bar{t}}$ distribution and the 2-dimensional distribution of $M_{t\bar{t}}^{true}$ versus $M_{t\bar{t}}$ used to derive the detector response matrix (see Figure 7.1) as well as the acceptance in each bin (see Section 4.4.1). I will point out the exceptions as I describe them below. Roughly in order of largest to smallest effects, the systematic effects I consider include:

1. The uncertainties on the jet energy scale described in Section 4.2.4 primarily effect the shape of the reconstructed $M_{t\bar{t}}$ distribution, especially the leading edge of the distribution. In general a $\pm 1 \cdot \sigma$ shift in the jet energy scale causes a ± 5 GeV/c^2 shift in the mean of the reconstructed $M_{t\bar{t}}$ distribution. The jet energy scale does not affect the truth level quantities (the top and anti-top 4-momenta) but it does cause migrations in the jets passing the $E_T > 20$ GeV requirement in the event selection. This migration of jets above and below threshold causes shifts in the acceptance on the order of a few percent.

2. The PDF's which describe the distribution of the proton and anti-proton momenta among the constituent quarks and gluons carry uncertainties due to the uncertainties associated with the underlying experimental measurements used to calculate the PDF's. An additional source of uncertainty is the set of assumptions and methods used to calculate the PDF's, which vary by calculation. The tail of the $M_{t\bar{t}}$ distribution is highly sensitive to the choice of PDF at both the truth and reconstruction levels, so all aspects of the differential cross section are effected. I consider three different variations to the PDF set used for the signal Monte Carlo simulation. The first variation is to compare the measured $d\sigma/dM_{t\bar{t}}$ using the default `CTEQ5L` PDF to the `MRST72` PDF [54]. The second change uses variations in the next to leading order `CTEQ` PDF

CTEQ6L. The CTEQ6L PDF set is described by 20 independent eigenvectors. A 90% confidence interval for each eigenvector is provided. The difference in the measured $d\sigma/dM_{t\bar{t}}$ between the maximum and minimum value and the central value is computed.[1] Finally the difference between the MRST72 and MRST75 PDF's is considered. These two MRST PDF's [54] use different values of α_s. The final PDF uncertainty is the quadrature sum of the largest of the first two effects with the comparison of different α_s values.

3. The uncertainty on the normalization of the $t\bar{t}$ backgrounds propagates to $d\sigma/dM_{t\bar{t}}$ as an uncertainty on the $t\bar{t}$ content in each bin.

4. As I discussed in Section 3.2 the exact details of the model used for quark hadronization to jets varies among Monte Carlo event generators. I assess an uncertainty on the Monte Carlo event generator by comparing the measured $d\sigma/dM_{t\bar{t}}$ with the default generator (PYTHIA) to an alternate generator, HERWIG.

5. The uncertainty on the acceptance includes a small statistical uncertainty due to the size of the sample used to calculate the acceptance and the uncertainties on the various corrections factors that are applied to the raw acceptance (see Section 4.4.1).

6. Gluons radiated by the initial quarks or gluons and/or the final state $t\bar{t}$ pair cause extra jets in the event not from top. Because I allow greater than 4 jets in my event selection, I am largely insensitive to the effects of final state radiation (FSR), but jets due to initial state radiation (ISR) that are incorrectly attributed to the $t\bar{t}$ pair alter the shape of the $M_{t\bar{t}}$ distribution and the acceptance in each bin. The amount of ISR and FSR are tunable parameters in the Monte Carlo simulation. A systematic uncertainty is assessed by putting more or less ISR and FSR in the simulation and comparing the measured $d\sigma/dM_{t\bar{t}}$ to the default. The allowed variation is based on a study of ISR in Drell-Yan events in data and Monte Carlo simulations. The same variation is applied to the ISR and FSR simultaneously.

7. The $M_{t\bar{t}}$ distribution of the SM $t\bar{t}$ backgrounds is taken from Monte Carlo simulations of the various background processes, as described in Section 5.4. A systematic uncertainty on the largest background shape, that from W+jets events, is assessed by varying the Q^2 scale of the hard scatter process in the ALPGEN Monte Carlo simulation and comparing the measured $d\sigma/dM_{t\bar{t}}$. The default is compared to Monte Carlo events generated with one half and twice the Q^2 scale. I also assess a systematic on the shape of the non-W background by using an alternate data model for the non-W events.

8. The measurement of the luminosity carries an irreducible 6% uncertainty due to the uncertainty of the acceptance of the CLC detectors and the calculation of the total inelastic $p\overline{p}$ cross section.

[1] I do not use 40 different signal Monte Carlo simulations to evaluate the uncertainty. The default signal Monte Carlo sample is re-weighted to account for differences between CTEQ5L and the CTEQ6 eigenvectors.

8.3 Evaluating Systematic Uncertainties

I evaluate the effect on the measured $d\sigma/dM_{t\bar{t}}$ of the systematic uncertainties listed in the previous section by using a pseudo-experiment approach. In each pseudo-experiment I vary the pseudo-data by using the various samples I describe above instead of the default models. For example, to evaluate the jet energy scale uncertainty, the pseudo-data is drawn from $M_{t\bar{t}}$ distributions of signal and background with the jet energy scale shifted by $\pm 1 \cdot \sigma_{JES}$. I perform the analysis as I would in data with the default unfolding procedure and acceptances in each bin and calculate $d\sigma/dM_{t\bar{t}}$. In this way I model the effect of using the wrong unfolding model and acceptance in the data. For the uncertainties related to the background normalization and the acceptance, the pseudo-data does not change. To evaluate the background normalization systematic uncertainty I subtract the background distribution normalized to the central value of the prediction plus or minus $1 \cdot \sigma_{Bkg}$, as given in Table 5.3. To evaluate the uncertainty on the acceptance I divide by the denominator shifted by plus or minus $1 \cdot \sigma_{\mathcal{A}_i}$ uncertainty, as given in Table 7.2.

The final systematic uncertainty on $d\sigma/dM_{t\bar{t}}$ is assessed per-bin by comparing the mean measured differential cross section in each bin from pseudo-experiments with the variations to pseudo-experiments using the default models. For those variations with a well-defined $\pm 1 \cdot \sigma$ variation - for example, the jet energy scale - the systematic uncertainty in each bin is one half the difference between the $+1 \cdot \sigma$ variation and $-1 \cdot \sigma$ variation. For those systematic uncertainties which are evaluated via a comparison of two models - for example, the Monte Carlo event generator systematic - the systematic uncertainty in each bin is the absolute value of the difference between the variation and the default.

8.4 Expected Sensitivity of the Analysis

The final systematic uncertainties for each bin are given in Table 8.4. The total systematic uncertainty in each bin is the quadrature sum of all of the individual uncertainties in each bin. The total does not include the 6% uncertainty due to luminosity in each bin.

Bin Number	1	2	3	4	5	6	7	8	9
MC Gen.	11.7	7.6	0.2	4.6	5.5	6.6	10.8	15.5	18.1
ISR/FSR	4.2	2.5	0.8	2.4	1.7	1.1	0.9	1.1	1.9
JES	22.3	10.6	11.1	21.1	21.3	20.8	22.8	25.3	26.3
Back. Shape	0.4	0.1	0.3	0.4	0.9	1.4	1.4	0.8	0.6
Back. Norm.	11.1	7.8	2.1	1.1	2.6	3.8	4.3	4.7	4.7
Acceptance	4.5	4.4	4.3	4.4	4.7	5.1	5.2	4.8	4.5
PDF Set	7.4	5.6	2.2	1.2	5.2	10.1	14.8	18.0	18.7
Total	29.1	17.0	12.3	22.2	23.3	24.9	30.1	35.3	37.6

Table 8.1: Summary of systematic uncertainties on $d\sigma/dM_{t\bar{t}}$ in each bin. All uncertainties are given as percentages. The bins are defined in Table 4.3.

The total sensitivity of the analysis is determined by the sum of the statistical and systematic uncertainties. The breakdown of the total uncertainties in each bin is given in Table 8.2.

$M_{t\bar{t}}$ [GeV/c^2]	Stat.	Sum Syst.	Total
0-350	22.4	29.1	36.8
350-400	14.2	17.0	22.2
400-450	9.5	12.3	15.5
450-500	12.5	22.2	25.5
500-550	14.4	23.3	27.4
550-600	16.2	24.9	29.7
600-700	19.7	30.1	35.9
700-800	31.1	35.3	47.0
800-1400	42.1	37.6	56.5

Table 8.2: Summary of total expected uncertainties. All uncertainties are given as percentages.

The systematic uncertainties in each bin are of the same order of magnitude as the statistical uncertainties and are dominated by the uncertainty on the jet energy scale and the uncertainty due to the choice of PDF. The uncertainty due to the PDF reflects the real sensitivity of the $M_{t\bar{t}}$ tail to the momentum of the $t\bar{t}$ system. A significant reduction in the PDF uncertainty would require the use of NLO PDF's with NLO Monte Carlo simulation. Unfortunately, NLO Monte Carlo simulations are not widely used due to technical problems with their implementation. However, a reduction in the jet energy scale uncertainty is possible by constraining the jet energy scale by using the event kinematics. The well-known W mass is used to constrain the jet energy scale of the jets from the hadronically decaying W. This technique was originally used and developed to reduce the jet energy scale uncertainty in a measurement of the top quark mass [55]. I will discuss how I apply this technique for this analysis in the next chapter.

Chapter 9

Reducing the Systematic Uncertainties

9.1 Introduction

I completed a version of this analysis using the method described in Chapter 7 using 1.9 fb^{-1} of data [56]. For the analysis with 2.7 fb^{-1} of data described here the jet energy scale uncertainty is reduced using an *in-situ* calibration of the jet energy scale using the kinematics of the hadronically decaying W in lepton+jets events. In this chapter I will describe how the *in-situ* calibration is used along with the unfolding technique to measure $d\sigma/dM_{t\bar{t}}$. This technique reduces the systematic uncertainties, presented in Table 8.4, by approximately 50% and the total statistical plus systematic uncertainty by about 20% with respect to the analysis with no *in-situ* jet energy scale calibration. I refer to the analysis without the *in-situ* jet energy scale calibration as the "baseline" analysis and the analysis with the calibration as the "improved" analysis.

The nominal jet energy scale is defined by the jet corrections described in Section 4.2.4. I will measure the quantity Δ_{JES}, which is the deviation from the nominal jet energy scale, defined by $\Delta_{JES} = 0$, in units of the total systematic uncertainty on the jet energy scale, σ_{JES}, as shown in Figure 4.8. The procedure is as follows: I reconstruct the invariant mass of the hadronic W daughters - the "dijet" invariant mass, M_{jj}. Then I use an unbinned maximum likelihood fit to compare the dijet invariant mass distribution in data to templates derived from Monte Carlo simulation with known values of Δ_{JES}. I then use the detector response matrix at Δ_{JES}^{data}, the value of Δ_{JES} that I fit in the data, to unfold the distribution and divide by the acceptance measured using Δ_{JES}^{data} to obtain $d\sigma/dM_{t\bar{t}}$. The next three sections are devoted to each of these steps:

1. Fit the dijet distribution in data to obtain Δ_{JES}^{data}.
2. Parameterize the detector response matrix and obtain the matrix at Δ_{JES}^{data}.
3. Parameterize the acceptance and obtain the denominator in each bin at Δ_{JES}^{data}.

9.2 Measurement of Δ_{JES} from the Dijet Invariant Mass Distribution

In order to reconstruct the dijet mass distribution the jets from the decay of the W must be distinguished from the other jets in the event. Because I assume that the 4 most energetic jets in the

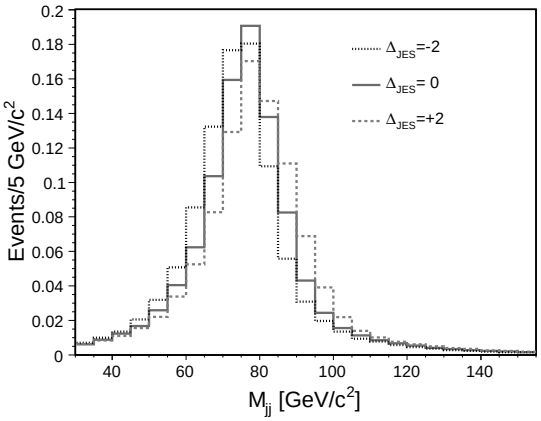

Figure 9.1: The reconstructed M_{jj} signal distribution in Monte Carlo events at various values of Δ_{JES}.

event are from the decay of the $t\bar{t}$ pair the problem is to identify which 2 of these 4 jets are W daughters and which 2 are b-jets. For events with 2 `SecVtx` b-tags in the leading 4 jets I identify the 2 untagged jets with the W daughters. For events with only 1 b-tag in the leading 4 jets I identify the W daughters by looking for the combination of untagged jets that have an invariant mass closest to the W mass. Because I do not apply the full set of jet corrections described in Section 4.2.4 the distribution of M_{jj} peaks somewhat lower than 80.4 GeV/c^2 due to the loss of energy outside the jet cone, for which I do not correct. For events in the signal Monte Carlo simulation passing my event selection where the jets have been matched to light quarks from the W in a cone of $R < 0.4$ the distribution peaks at 76.5 GeV/c^2. So for events with only 1 b-tag I find the combination of untagged jets with an invariant mass closest to 76.5 GeV/c^2.

I reconstruct the M_{jj} distribution, as described above, for the signal and background models for $\Delta_{JES} = \{-2, -1, 0, 1, 2\} \cdot \sigma_{JES}$. The M_{jj} signal distribution at three different Δ_{JES} points is shown in Figure 9.1. The distribution is harder for larger values of Δ_{JES}, as expected. The mean of the distributions increases by approximately 1.5 GeV/c^2 with each unit of Δ_{JES}. The width also changes slightly, getting wider at higher values of σ_{JES}. The M_{jj} distribution of the $t\bar{t}$ backgrounds at the same Δ_{JES} points in shown in Figure 9.2. The shapes do not vary appreciably with Δ_{JES}. Because the jet spectrum of the background processes is relatively soft there is significant migration of jets above and below the jet E_T threshold when the jet energy scale changes. The primary effect of changing the jet energy scale is to change the number of events in the template. This effect is constrained by the uncertainty on the normalization of the background events. Therefore, I assume a background shape that is constant with respect to variation in Δ_{JES}.

I fit these templates at various Δ_{JES} points to obtain probability density functions for the signal and background. The probability density function for the signal depends both on M_{jj} and Δ_{JES} but the background probability density function depends only on M_{jj} because the M_{jj} shape is constant with respect to variations in Δ_{JES}. The bulk of the M_{jj} probability distribution function is modeled by a Landau function which is convoluted with a Gaussian. An extra Gaussian term is

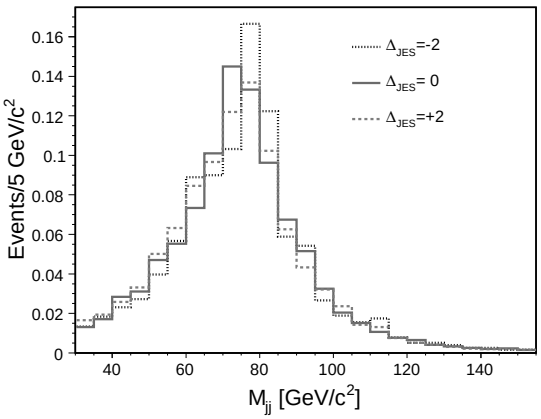

Figure 9.2: The reconstructed M_{jj} background distribution at various values of Δ_{JES}.

added to account for the shoulder in the low mass region. The Landau and Gaussian convolution has 4 parameters:

α_0 Width of Landau density

α_1 Most probable parameter of Landau density

α_2 Normalization

α_3 Width of convoluted Gaussian

The second Gaussian has 3 parameters:

α_4 Normalization

α_5 Mean

α_6 Width

The probability density function for the signal is given by:

$$P_{sig}(M_{jj};\Delta_{JES}) = \text{LandauGaussian}(M_{jj};\Delta_{JES}) + \text{Gaussian}(M_{jj};\Delta_{JES}) \tag{9.1}$$

where each parameter α_i depends quadratically on Δ_{JES}:

$$\alpha_i(\Delta_{JES}) = p_i + \Delta_{JES}\cdot p_{i+7} + \Delta^2_{JES}\cdot p_{i+14}. \tag{9.2}$$

A total of 21 parameters then define the signal probability distribution function. I use `Minuit` [57] to perform a binned maximum likelihood fit for the 21 parameters. Figure 9.3 shows the fit overlayed with the histograms of Figure 9.1. The probability distribution function for the background is given by:

$$P_{bkg}(M_{jj}) = \text{LandauGaussian}(M_{jj}) + \text{Gaussian}(M_{jj}) \tag{9.3}$$

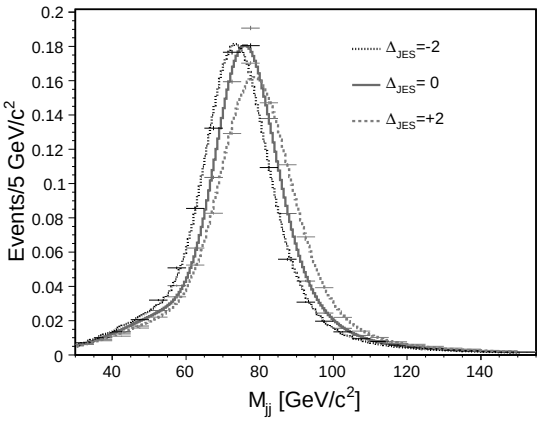

Figure 9.3: The reconstructed M_{jj} signal distribution at various values of Δ_{JES}, along with the fitted probability distribution functions.

The constant background probability density function is defined by 7 total parameters. The fit is compared to the background template in Figure 9.4.

The likelihood function to be maximized is:

$$\mathcal{L}_{M_{jj}} = \mathcal{L}_{shape} \times \mathcal{L}_{Nevts} \times \mathcal{L}_{Bkg}. \tag{9.4}$$

Most of the information comes from the term $\mathcal{L}_{shape}$:

$$\mathcal{L}_{shape} = \prod_{n=1}^{N} \frac{N_{sig}P_{sig}(M_{jj};\Delta_{JES}) + N_{bkg}P_{bkg}(M_{jj})}{N_{sig}+N_{bkg}} \tag{9.5}$$

which gives the probability for an event n that M_{jj} comes from background or signal. The number of signal events is given by N_{sig} and the number of background events by N_{bkg}. The product runs over N events in the range 30 GeV/$c^2 \leq M_{jj} \leq$ 150 GeV/c^2. The term $\mathcal{L}_{Nevts}$ is a simple Poisson:

$$\mathcal{L}_{Nevts} = \frac{e^{-(N_{sig}+N_{bkg})}(N_{sig}+N_{bkg})^N}{N!}. \tag{9.6}$$

The term $\mathcal{L}_{Bkg}$ constrains the normalization of the background to the expectation in Table 5.3:

$$\mathcal{L}_{Bkg} = exp(-\frac{(N_{bkg}-N_{bkg}^{exp})^2}{2\sigma_{exp}^2}). \tag{9.7}$$

I use `Minuit` to minimize $-ln\mathcal{L}_{M_{jj}}$.

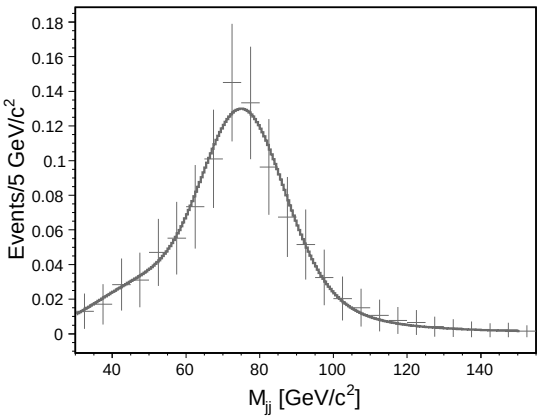

Figure 9.4: The reconstructed M_{jj} background distribution (at $\Delta_{JES} = 0$) along with the fitted probability density function.

9.3 Parameterizing the Response Matrix

Figure 9.5 shows the shape of the reconstructed $M_{t\bar{t}}$ distributions at $\Delta_{JES} = \{-2, 0, 2\} \cdot \sigma_{JES}$ for events with $M_{t\bar{t}}^{true}$ in each bin of $M_{t\bar{t}}^{true}$. The variation of the $M_{t\bar{t}}$ distributions is well-behaved as a function of Δ_{JES} - the distributions become harder as Δ_{JES} increases, as expected. For the detector response matrix derived from the distribution of $M_{t\bar{t}}^{true}$ versus $M_{t\bar{t}}$ the entries vary in a mostly monotonic fashion as a function of Δ_{JES}. I fit each bin of the matrix as a quadratic function of Δ_{JES}.

9.4 Parameterizing the Acceptance

The acceptance varies linearly with Δ_{JES} in each bin. I parameterize the denominator in each bin (without the bin width, as in Table 7.2) as a linear function of Δ_{JES}, as shown in Figure 9.6.

9.5 Tests of Analysis Procedure with *in-situ* Jet Energy Scale Calibration

I test this new procedure by performing pseudo-experiments. The procedure is similar to that described in Section 7.3. The number of signal and background events for each pseudo-experiment is given by a fluctuation of the expectation for the 2.7 fb^{-1} dataset. The M_{jj} and $M_{t\bar{t}}$ distributions for each pseudo-experiment are drawn at random from a 2-dimensional distribution of M_{jj} versus $M_{t\bar{t}}$ in the Monte Carlo simulations for signal and background. By drawing from this 2-dimensional distribution, the small correlations between M_{jj} and $M_{t\bar{t}}$ are modeled in the pseudo-experiments. I fit the M_{jj} distribution to obtain Δ_{JES}, then unfold the reconstructed $M_{t\bar{t}}$ distribution with the appropriate detector response matrix and divide by the appropriate acceptance to obtain $d\sigma/dM_{t\bar{t}}$.

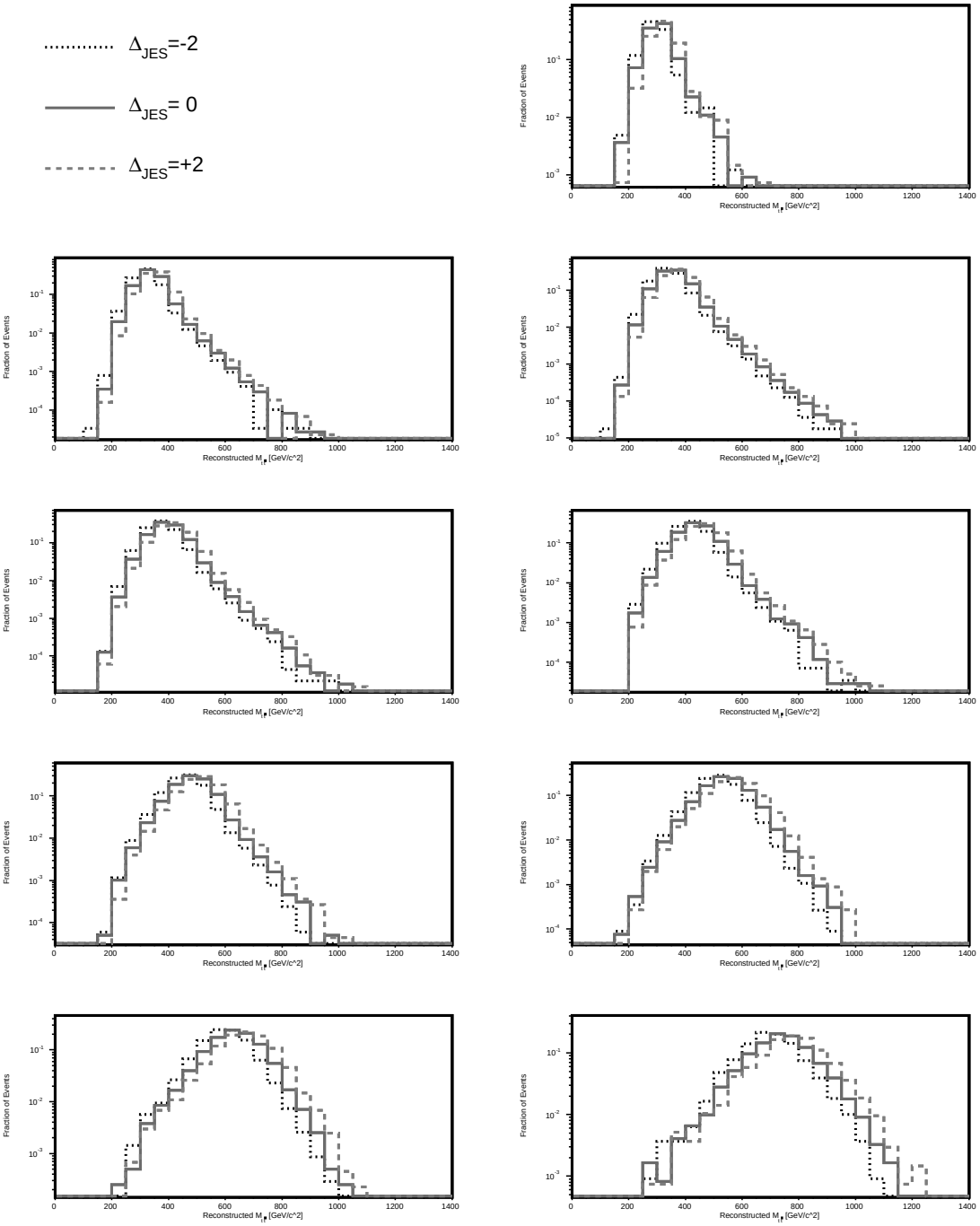

Figure 9.5: Variation of $M_{t\bar{t}}$ with Δ_{JES} in each bin of $M_{t\bar{t}}^{true}$. Events in true bin 1 are in the top right plot, events in true bins 2 and 3 are the in the second row, *etc.*

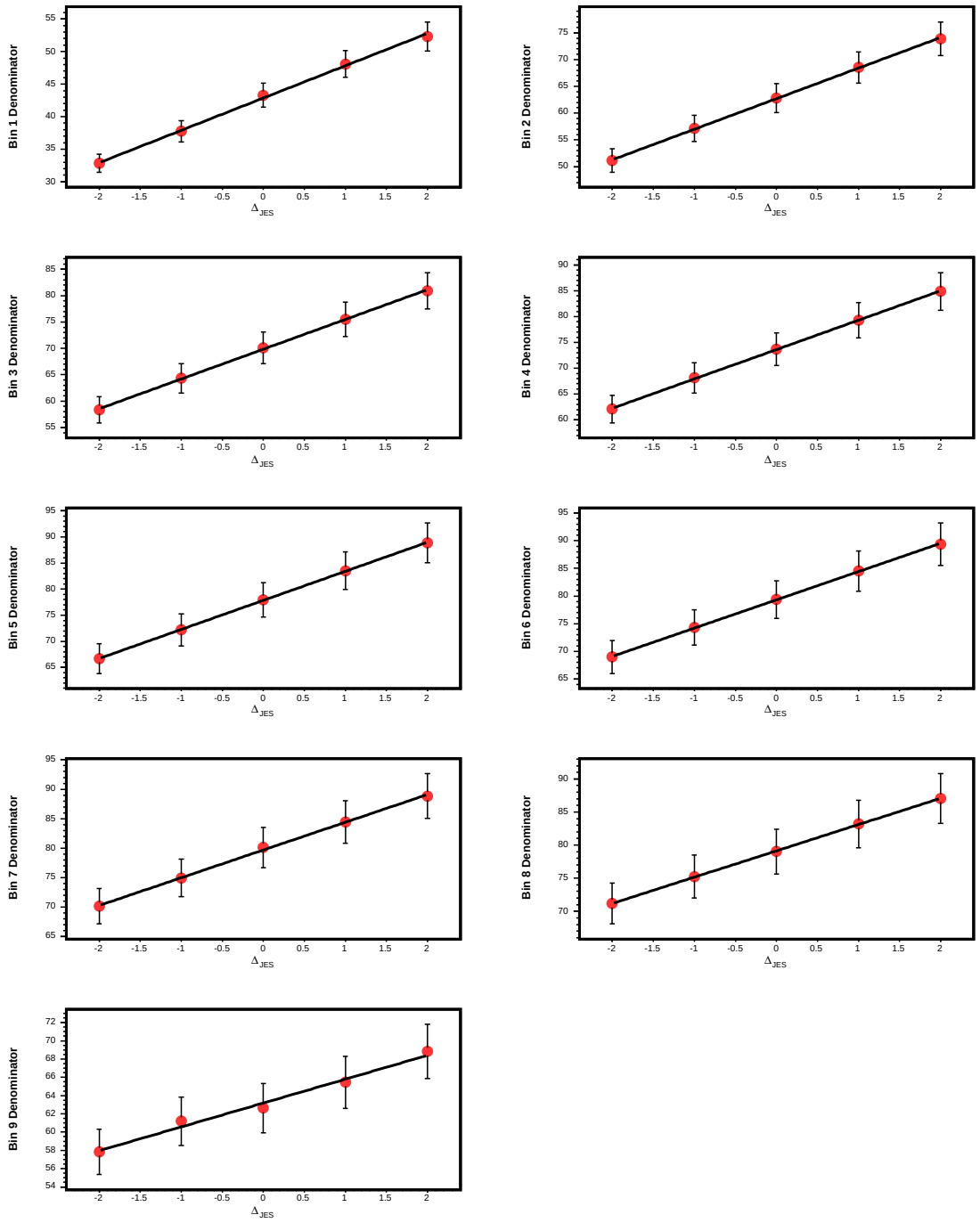

Figure 9.6: Denominator in each bin as a function of Δ_{JES}. Bins 1 and 2 are in the first row, 3 and 4 in the second row, *etc.* The points are the values for $\Delta_{JES} = \{-2, -1, 0, 1, 2\} \cdot \sigma_{JES}$ and the black line is the fitted function.

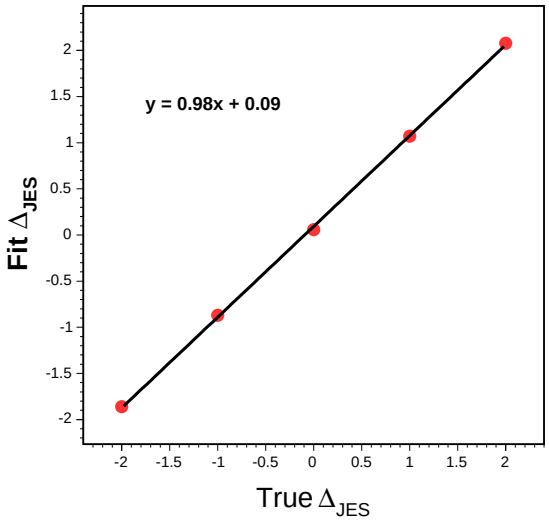

Figure 9.7: Mean value of Δ_{JES}^{fit} from pseudo-experiments versus Δ_{JES}^{true}.

First I check the linearity of the Δ_{JES} fit by plotting the fitted value of Δ_{JES}, Δ_{JES}^{fit}, versus the true (input) value Δ_{JES}, Δ_{JES}^{true}, for pseudo-experiments performed at a range of Δ_{JES}^{true} values. The result is shown in Figure 9.7. A fit to the Δ_{JES}^{fit} versus Δ_{JES}^{true} line gives:

$$\Delta_{JES}^{fit} = 0.98 \cdot \Delta_{JES}^{true} + 0.09 \tag{9.8}$$

which indicates that a small correction is needed to the value of Δ_{JES}^{fit} to obtain the true value. The means of the the pull distributions for Δ_{JES}^{fit} show similar shifts from zero.

I apply the correction to the Δ_{JES}^{fit} from Equation 9.8 and repeat the pseudo-experiments. The new Δ_{JES}^{fit} versus Δ_{JES}^{true} curve is shown in Figure 9.8. The means and widths of the pull distributions for Δ_{JES}^{fit} at various values of Δ_{JES}^{true} are shown in Figures 9.9 and 9.10. The correction has removed the bias in the value of Δ_{JES}^{fit}. Furthermore, the uncertainty returned by the fit is accurate as the pull widths are consistent with one across the range of Δ_{JES}^{true} values. The resolution of the fit is shown in Figure 9.11. The uncertainty is approximately $0.46 \cdot \sigma_{JES}$ - it is slightly higher at large negative values of Δ_{JES}^{true} and slightly lower at large positive values of Δ_{JES}^{true}. This is significantly less than the $1 \cdot \sigma_{JES}$ uncertainty of the nominal jet energy scale. The trade-off for the reduced systematic uncertainty is an increase in the statistical uncertainty. I will show in the next section that the end result is an overall reduction in the total expected uncertainty.

I also check in these pseudo-experiments the pulls for the unfolded number of events in each bin. The input covariance matrix to the unfolding includes the uncertainty on the background expectation in each bin and the Poisson uncertainty on the number of events reconstructed in each bin as before in addition to a contribution from the uncertainty on Δ_{JES}^{fit}. The pull means and widths are generally consistent with zero and one, respectively, within their uncertainties. For those bins with a pull width less than one I do not correct for the over-estimation of the uncertainty. For

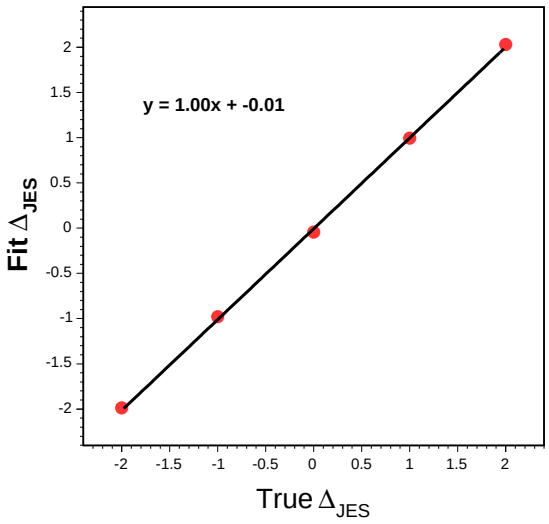

Figure 9.8: Mean value of Δ_{JES}^{fit} from pseudo-experiments versus Δ_{JES}^{true} after the correction is applied.

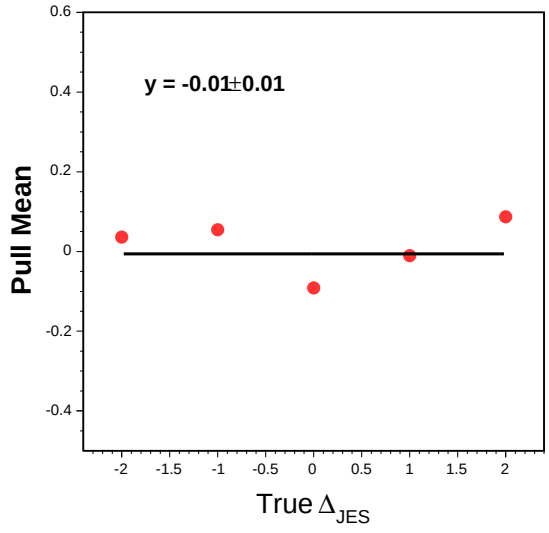

Figure 9.9: Mean of Δ_{JES}^{fit} pull distribution versus Δ_{JES}^{true} after the correction is applied.

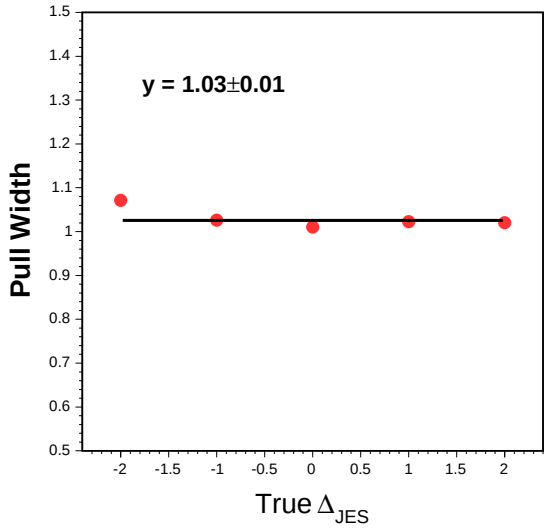

Figure 9.10: Width of Δ_{JES}^{fit} pull distribution versus Δ_{JES}^{true} after the correction is applied.

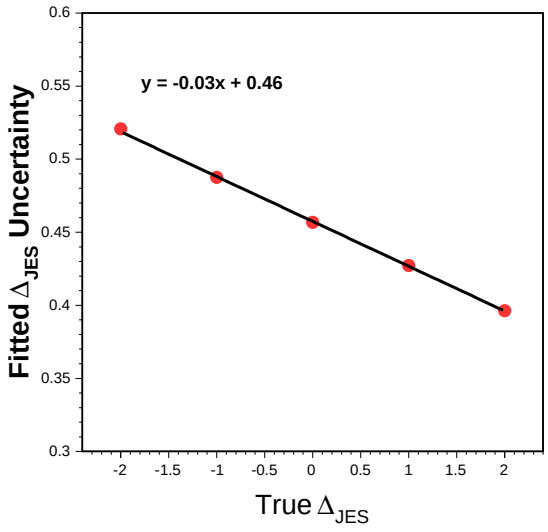

Figure 9.11: The mean uncertainty on Δ_{JES}^{fit} from pseudo-experiments versus Δ_{JES}^{true}.

Pull Mean			
$M_{t\bar{t}}$ [GeV/c^2]	Δ_{JES}^{true}=-1	Δ_{JES}^{true}=0	Δ_{JES}^{true}=1
0-350	0.11 ± 0.03	-0.02 ± 0.02	0.06 ± 0.02
350-400	0.09 ± 0.03	0.05 ± 0.02	0.09 ± 0.02
400-450	-0.03 ± 0.02	0.04 ± 0.02	0.02 ± 0.02
450-500	-0.07 ± 0.02	0.02 ± 0.02	-0.01 ± 0.02
500-550	-0.03 ± 0.02	-0.02 ± 0.02	0.01 ± 0.02
550-600	-0.04 ± 0.02	-0.05 ± 0.02	-0.00 ± 0.02
600-700	0.04 ± 0.02	-0.01 ± 0.02	-0.02 ± 0.02
700-800	0.12 ± 0.02	0.08 ± 0.02	-0.01 ± 0.02
800-1400	0.13 ± 0.02	0.13 ± 0.02	0.02 ± 0.02
Pull Width			
$M_{t\bar{t}}$ [GeV/c^2]	Δ_{JES}^{true}=-1	Δ_{JES}^{true}=0	Δ_{JES}^{true}=1
0-350	1.12 ± 0.02	1.07 ± 0.02	1.01 ± 0.02
350-400	1.11 ± 0.02	1.09 ± 0.02	1.01 ± 0.02
400-450	0.92 ± 0.01	0.92 ± 0.01	0.89 ± 0.01
450-500	0.98 ± 0.02	0.93 ± 0.02	0.92 ± 0.02
500-550	1.00 ± 0.02	0.95 ± 0.01	0.93 ± 0.02
550-600	1.01 ± 0.02	0.97 ± 0.02	0.94 ± 0.01
600-700	1.01 ± 0.02	0.96 ± 0.02	0.96 ± 0.02
700-800	0.95 ± 0.02	0.95 ± 0.02	0.95 ± 0.02
800-1400	0.93 ± 0.02	0.92 ± 0.01	0.94 ± 0.02

Table 9.1: The mean and widths of the pull for the number of unfolded events in each bin, as defined in Equation 7.48, at various Δ_{JES} points.

those means that are shifted from zero, the effect on the final cross section is small with respect to the statistical uncertainty and I do not correct for it.

9.6 New Systematic Uncertainties

In addition to the systematic uncertainties described in Chapter 8, there are additional systematic uncertainties associated with the Δ_{JES} measurement. First, there is a "residual" Δ_{JES} uncertainty associated with describing the jet energy scale as one large shift from the nominal, rather than as shifts from each individual level of correction described in Section 4.2.4. This uncertainty is assessed by shifting each level of uncertainty on the jet energy scale: relative, multiple interactions, absolute, and out of cone individually and then adding the result in quadrature. Secondly there is an uncertainty on the b-jet energy scale. This is added because the jets from W are light quarks, but I apply the correction to all jets in the event. The b-jet energy scale uncertainty includes an uncertainty on the b-jet semi-leptonic branching ratio and the b-quark fragmentation in the Monte Carlo simulation and the energy scale of the b-jets themselves. The updated systematic uncertainties are presented in Table 9.6. The total does not include the 6% uncertainty due to the luminosity measurement.

Bin Number	1	2	3	4	5	6	7	8	9
MC Gen.	0.7	2.4	5.3	5.7	4.6	3.3	1.4	0.0	1.0
ISR/FSR	1.5	1.3	0.8	0.2	1.1	2.1	2.0	2.2	3.3
Residual JES	7.1	5.9	3.9	2.5	1.4	2.2	4.5	7.2	8.7
b-jet JES	4.1	2.2	1.1	1.9	1.0	0.6	0.7	2.1	2.7
Back. Shape	0.4	0.3	0.6	0.6	0.4	0.4	0.8	1.3	1.8
Back. Norm.	10.3	7.4	2.3	1.6	3.0	4.0	4.4	4.9	5.1
Acceptance	4.5	4.4	4.3	4.4	4.6	4.6	4.4	4.0	3.8
PDF Set	7.7	6.1	3.0	1.0	4.8	9.3	14.0	17.4	18.8
Total	16.0	12.6	8.9	8.1	8.9	12.0	16.1	20.1	22.2

Table 9.2: Summary of systematic uncertainties on $d\sigma/dM_{t\bar{t}}$ in each bin for the improved analysis with Δ_{JES} fit. All uncertainties are given as percentages. The bins are defined in Table 4.3.

The total expected uncertainty of the improved analysis is given in Table 9.3. Now the statistical uncertainty reflects the uncertainty on Δ_{JES}. The statistical uncertainty in each bin is approximately 10% higher with respect to the baseline analysis, as given in Table 8.2. Again the 6% uncertainty due to the luminosity measurement is not included. Table 9.4 presents side-by-side the expected uncertainties for the baseline versus improved analysis. In the tail of the distribution, the most relevant area for new physics, the systematic uncertainties are reduced by approximately one half. At the same time the statistical uncertainty increases by only about 10%. The overall sensitivity is significantly improved by the *in situ* jet energy scale calibration.

$M_{t\bar{t}}$ [GeV/c^2]	Stat.+JES	Sum Syst.	Total
0-350	24.1	16.0	28.9
350-400	15.0	12.6	19.7
400-450	10.3	8.9	13.6
450-500	13.8	8.1	16.0
500-550	15.8	8.9	18.1
550-600	17.5	12.0	21.2
600-700	20.7	16.1	26.3
700-800	32.3	20.1	38.0
800-1400	43.8	22.2	49.1

Table 9.3: Summary of total expected uncertainties. All uncertainties are given as percentages

	Baseline Analysis			Improved Analysis		
$M_{t\bar{t}}$ [GeV/c^2]	Stat.	Sum Syst.	Total	Stat.+JES	Sum Syst.	Total
0-350	22.4	29.1	36.8	24.1	16.0	28.9
350-400	14.2	17.0	22.2	15.0	12.6	19.7
400-450	9.5	12.3	15.5	10.3	8.9	13.6
450-500	12.5	22.2	25.5	13.8	8.1	16.0
500-550	14.4	23.3	27.4	15.8	8.9	18.1
550-600	16.2	24.9	29.7	17.5	12.0	21.2
600-700	19.7	30.1	35.9	20.7	16.1	26.3
700-800	31.1	35.3	47.0	32.3	20.1	38.0
800-1400	42.1	37.6	56.5	43.8	22.2	49.1

Table 9.4: Comparison of expected uncertainties for the baseline analysis with no Δ_{JES} fit and the improved analysis with the Δ_{JES} fit. All uncertainties are given as percentages and the total does not include the uncertainty due to the luminosity measurement.

Chapter 10

Results

10.1 Introduction

I this Chapter I will present my measurement of $d\sigma/dM_{t\bar{t}}$ in 2.7 fb^{-1} of data. I begin in Section 10.2 by checking several relevant kinematic distributions in the data. In Section 10.3 I present the result of the fit for Δ_{JES} and show the unfolded $M_{t\bar{t}}$ distribution in Section 10.4. In Section 10.5 I give the final calculation of $d\sigma/dM_{t\bar{t}}$ and present several cross checks of the result in Section 10.6.

10.2 Kinematic Distributions

In order to check the Monte Carlo models of the signal and background in the Monte Carlo I compare, in the data and Monte Carlo simulation, the important kinematic distributions used in the $M_{t\bar{t}}$ reconstruction - the energy of the 4 most energetic jets in the event, the momentum of the lepton, and the missing transverse energy. In these distributions, the background distribution is normalized to the expectation in Table 5.3 and the signal distribution is the default $t\bar{t}$ model with $\Delta_{JES} = 0$, normalized to the difference between the number of data events and the background expectation. The transverse energy of the leading 4 jets in the event is shown in Figure 10.1, the transverse momentum of the lepton is shown in Figure 10.2, and the distribution of missing transverse energy in shown in Figure 10.3. There are no serious discrepancies with the predicted distributions.

A useful variable for discriminating $t\bar{t}$ events from other processes is H_T. The H_T is the scalar sum of the transverse energy of all objects in the event - jets, missing energy and the lepton. Energetic $t\bar{t}$ events have higher H_T than other events, as can be seen in Figure 10.4. This distribution shows consistency with SM $t\bar{t}$ production, with only a slight excess of events in the high H_T tail. The distribution of $M_{t\bar{t}}$ in the data is shown in Figure 10.5. The binning in this figure is slightly different from the binning used to calculate $d\sigma/dM_{t\bar{t}}$ in order to show the threshold for $t\bar{t}$ production at low $M_{t\bar{t}}$. Again there is no serious discrepancy with the models, and the distribution seems to be consistent with SM $t\bar{t}$ production, with only a few excess events in the high $M_{t\bar{t}}$ region.

10.3 M_{jj} Fit

The M_{jj} distribution of the data is given in Figure 10.6. The M_{jj} distribution in data is shifted slightly higher than the signal and background models at the nominal jet energy scale so I expect

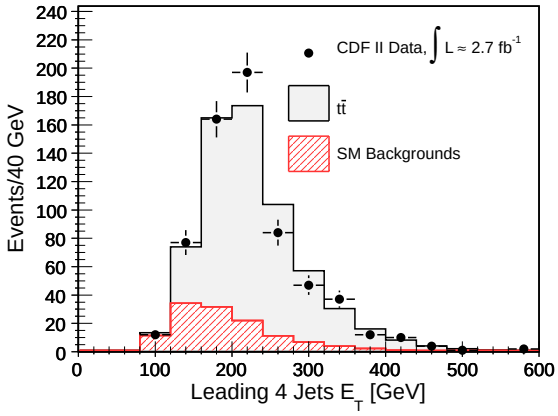

Figure 10.1: The distribution of E_T for the leading 4 jets in the data.

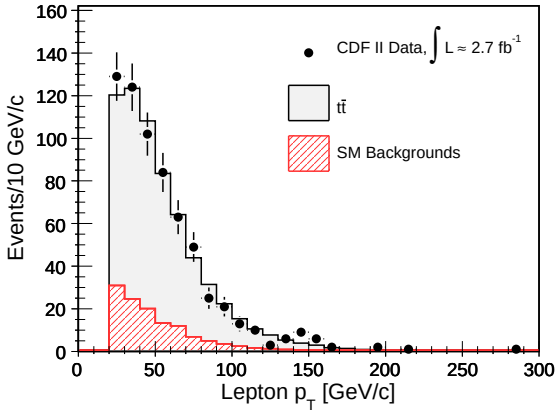

Figure 10.2: The distribution of p_T for the electron or muon in the data.

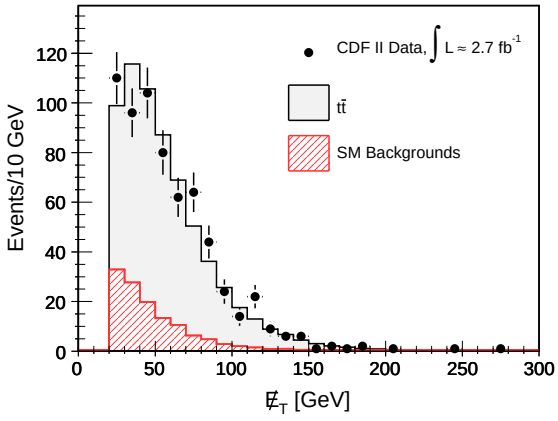

Figure 10.3: The distribution of $\not\!\!E_T$ in the data.

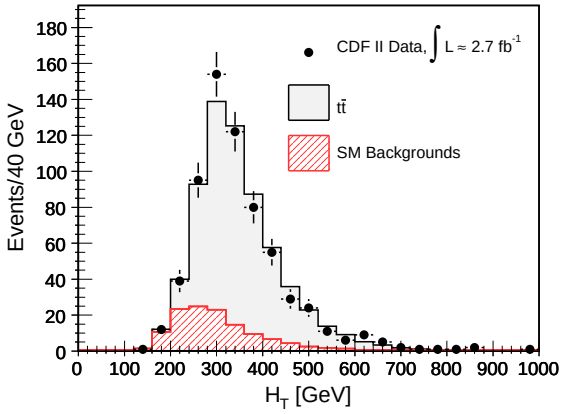

Figure 10.4: The distribution of H_T in the data.

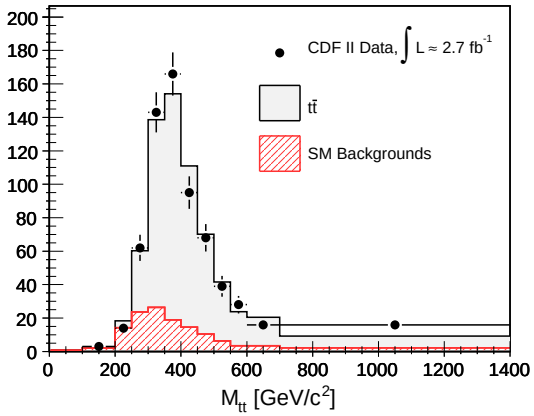

Figure 10.5: The distribution of $M_{t\bar{t}}$ in the data.

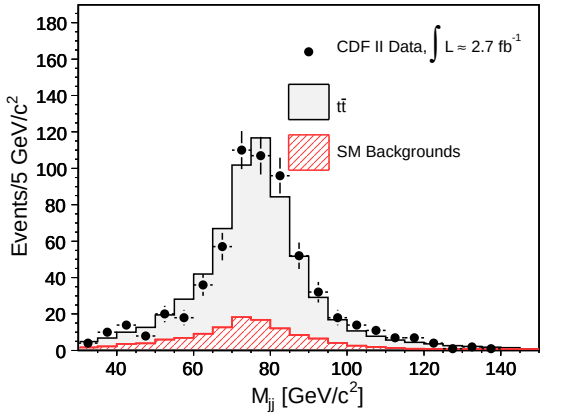

Figure 10.6: The distribution of M_{jj} in the data.

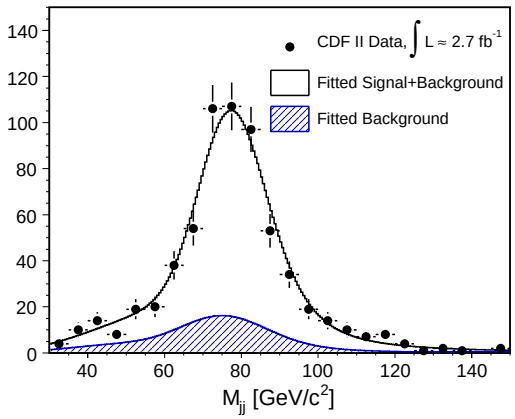

Figure 10.7: The fitted M_{jj} distribution in data.

to fit $\Delta_{JES} > 0$. Using the likelihood procedure described in detail in Section 9.2, I do fit a higher-than-nominal value of $\Delta_{JES} = 1.3 \pm 0.5\ \sigma_{JES}$. This value is corrected according to Equation 9.8 to give $\Delta_{JES}^{data} = 1.27 \pm 0.5\ \sigma_{JES}$. I fit a total number of background events in the data sample, N_{bkg}^{fit}, of 123 ± 21.6, which is slightly lower than the expectation of 126 ± 22.5 given in Table 5.3. The M_{jj} distribution is shown along with the signal and background templates with $\Delta_{JES} = \Delta_{JES}^{data}$ in Figure 10.7.

10.4 Unfolding

The unfolding begins by first subtracting the background distribution, shown in Figure 5.3, from the reconstructed $M_{t\bar{t}}$ distribution in each bin. The total background is normalized to N_{bkg}^{fit}. The $M_{t\bar{t}}$ distribution in data, with the binning used in the unfolding, is shown in Figure 10.8. In this figure the background content has been normalized to N_{bkg}^{fit} and the difference between the data and the background is the $t\bar{t}$ content. Next I build the detector response matrix, filled with actual numbers of events (Equation 7.31), at $\Delta_{JES} = \Delta_{JES}^{data}$, as shown in Figure 10.9. Based on pseudo-experiments, I set the effective rank of the system, k, to 4. The logarithm of the elements of the vector d (Equation 7.38) for the background-subtracted data is shown in Figure 10.10. This figure is consistent with the same effective rank as that used in the pseudo-experiments. The final unfolded distribution, compared to the true distribution at $\Delta_{JES} = \Delta_{JES}^{data}$ is shown in Figure 10.11.

10.5 Differential Cross Section

I calculate $d\sigma/dM_{t\bar{t}}$ by dividing the number of $t\bar{t}$ events in each bin of the unfolded distribution by the appropriate denominator, calculated at $\Delta_{JES} = \Delta_{JES}^{data}$ (see Figure 9.6). The final differential cross section is shown in Figure 10.12 and Table 10.1.

I will discuss in the next chapter the consistency of this result with the SM, but clearly there

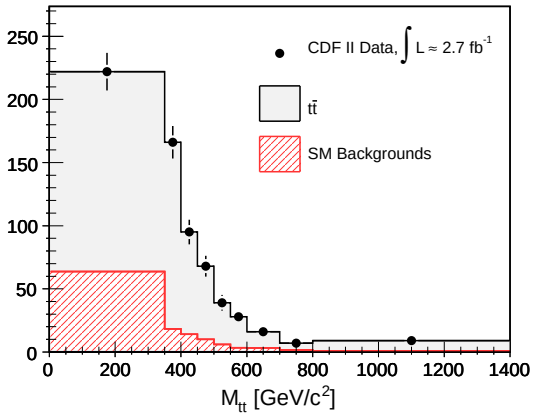

Figure 10.8: The distribution of $M_{t\bar{t}}$ in the data. The background distribution is normalized to N_{bkg}^{fit} and the $t\bar{t}$ content is the difference between the data and the background.

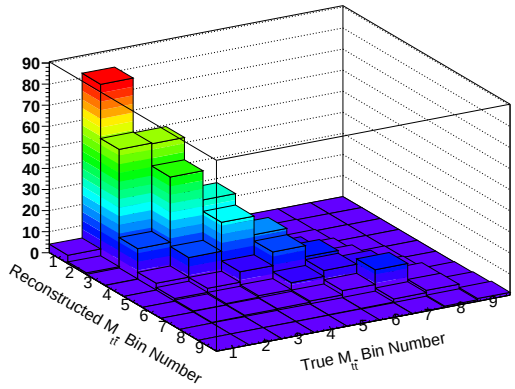

Figure 10.9: The detector response matrix used for unfolding the reconstructed $M_{t\bar{t}}$ distribution in data.

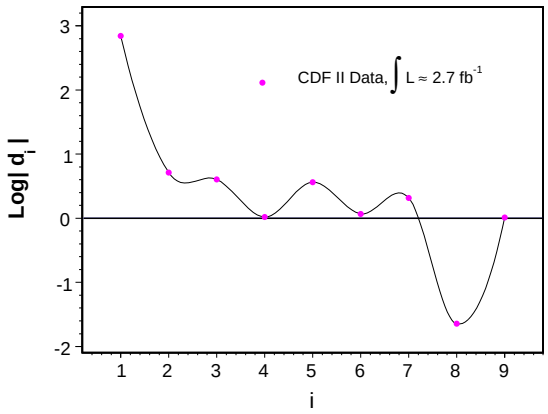

Figure 10.10: The elements of the vector d in the data.

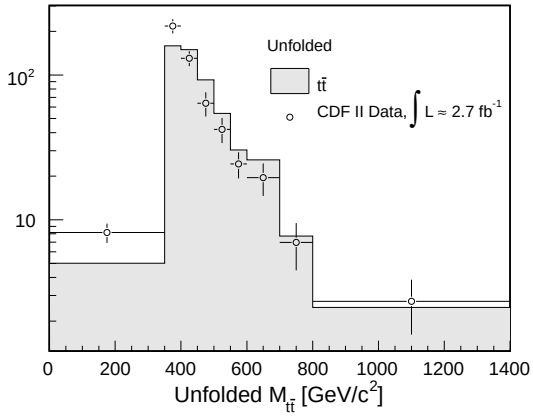

Figure 10.11: The unfolded background-subtracted $M_{t\bar{t}}$ distribution in data.

Δ_{JES}^{data} (after correction) $[\sigma_{JES}]$	1.3 ± 0.5
$M_{t\bar{t}}$ [GeV/c^2]	$d\sigma/dM_{t\bar{t}}$ [fb/GeV/c^2]
≤ 350	0.47 ± 0.07 (stat.+JES) ± 0.08 (syst.) ± 0.028 (lumi.)
350-400	62.3 ± 7.0 (stat.+JES) ± 7.9 (syst.) ± 3.7 (lumi.)
400-450	33.8 ± 4.0 (stat.+JES) ± 3.0 (syst.) ± 2.0 (lumi.)
450-500	15.8 ± 3.0 (stat.+JES) ± 1.3 (syst.) ± 0.9 (lumi.)
500-550	9.9 ± 2.0 (stat.+JES) ± 0.9 (syst.) ± 0.6 (lumi.)
550-600	5.7 ± 1.2 (stat.+JES) ± 0.7 (syst.) ± 0.3 (lumi.)
600-700	2.3 ± 0.6 (stat.+JES) ± 0.4 (syst.) ± 0.1 (lumi.)
700-800	0.8 ± 0.3 (stat.+JES) ± 0.2 (syst.) ± 0.0 (lumi.)
800-1400	0.07 ± 0.03 (stat.+JES) ± 0.02 (syst.) ± 0.004 (lumi.)
Integrated Cross Section [pb]	6.9 ± 1.0 (stat.+JES)

Table 10.1: Measured $d\sigma/dM_{t\bar{t}}$ in 2.7fb^{-1} of data.

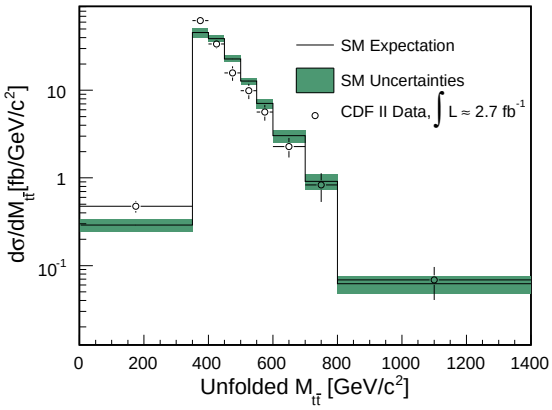

Figure 10.12: $d\sigma/dM_{t\bar{t}}$ measured in 2.7 fb^{-1} of data. The uncertainty does not include the 6% uncertainty due to the luminosity measurement.

are no large deviations from the SM expectation in Figure 10.12. The integrated cross section of 7.0 ± 1.0 pb, where the uncertainty is the statistical+JES uncertainty only, is also consistent both with the SM expectation [7] and the current CDF II combination of 7.0 ± 0.6 pb [37].

10.6 Cross Checks

I perform several cross checks of this result using different sub-samples of the data:

1. Events where the lepton is an electron.
2. Events where the lepton is a muon.
3. Events with ≥ 2 b-tags.

For each of these sub-samples I modify each piece of the analysis:

- The probability distribution functions $P_{sig}(M_{jj}; \Delta_{JES})$ (Equation 9.1) and $P_{bkg}(M_{jj})$ (Equation 9.3) are changed based on the shape of the M_{jj} templates for each sub-sample.
- The $M_{t\bar{t}}$ distribution of the background that is subtracted changes to reflect the shape in each sub-sample.
- The parameterization of the detector response matrix in terms of Δ_{JES} changes based upon the $M_{t\bar{t}}^{true}$ versus $M_{t\bar{t}}$ distribution for each sub-sample.
- The parameterization of the acceptance in terms of Δ_{JES} changes to reflect the acceptance for each sub-sample.

Because the physics of each of the sub-samples is the same as the complete data sample (at least in the SM), all of the results should be consistent with each other within their associated uncertainties.

A large discrepancy would most likely be the result of a problem calculating the acceptance, or with any of the parameterizations used.[1] The results in the various sub-samples are presented in Table 10.2. The results are all consistent with each other, and the result in Table 10.2, within $1 \cdot \sigma$ of the uncertainties.

	Electron Only	Muon Only	≥ 2 b-tags
Δ_{JES}^{data} (after correction) $[\sigma_{JES}]$	1.6 ± 0.6	0.4 ± 0.7	1.3 ± 0.7
$M_{t\bar{t}}$ $[GeV/c^2]$	$d\sigma/dM_{t\bar{t}}$ $[fb/GeV/c^2]$ (stat.+JES uncert. only)		
≤ 350	0.5 ± 0.1	0.4 ± 0.1	0.3 ± 0.1
350-400	62.7 ± 9.4	59.4 ± 10.3	46.9 ± 9.2
400-450	29.2 ± 4.9	42.7 ± 6.7	34.6 ± 6.2
450-500	13.4 ± 3.7	21.9 ± 5.0	18.1 ± 4.6
500-550	9.8 ± 2.5	11.2 ± 3.2	8.9 ± 2.9
550-600	6.0 ± 1.5	5.8 ± 1.9	4.6 ± 1.7
600-700	2.0 ± 0.7	2.6 ± 1.0	2.2 ± 1.0
700-800	0.4 ± 0.3	1.2 ± 0.5	0.8 ± 0.5
800-1400	0.03 ± 0.03	0.10 ± 0.05	0.07 ± 0.04
Integrated Cross Section [pb]	6.5 ± 1.3	7.6 ± 1.6	6.1 ± 1.4

Table 10.2: Comparison of results in different sub-samples of the data.

[1] It also could indicate an incredibly exotic BSM model of physics where, for example, the branching ratios of the W-like daughters of the $t\bar{t}$ pair are drastically different from that in the SM so the W-like object decays much more often to muons, but that would be very strange. A mistake is far more likely.

Chapter 11

Consistency with the Standard Model and Limits on New Physics

11.1 Introduction

In order to set limits on new physics, I need a quantitative measure of the agreement between the data and the SM physics hypothesis as well as a measure of the agreement between the data and the BSM physics hypothesis. I calculate a test statistic, X, which distinguishes between the SM and BSM models. Given a distribution of X for each model and the value of X, X_{obs}, that I calculate from the data, I calculate the probability that X_{obs} comes from each model. I will describe this procedure in more detail in Section 11.3.

I will set limits on the coupling of Kaluza-Klein (KK) gravitons to top quarks in the Randall-Sundrum (RS) model described briefly in Section 1.4. In the RS model a single extra dimension is compactified to an orbifold with two branes at specific points: a "Plank brane" at $\phi = 0$ and a "TeV brane" at $\phi = \pi$. The SM fields are confined to the TeV brane. Warping of the extra dimension causes the Plank mass to be warped down at the TeV brane to $\Lambda = M_{Pl}e^{-\pi\kappa R}$ where κ is the warp factor and R is the size of the extra dimension. The KK gravitons couple with strength $\sim 1/\Lambda$. The masses of the KK gravitons are given by:

$$m_n^2 = x_n \kappa e^{-\pi\kappa R} \tag{11.1}$$

where x_n are the positive zeroes of the Bessel function $J_1(x)$. This leads to a series of resonances in the $t\bar{t}$ invariant mass spectrum [9]. I set the mass of the first resonance to 600 GeV/c^2, chosen because it is well above the peak of the $M_{t\bar{t}}$ distribution where the effects of variations in the jet energy scale are the largest, and set limits on the value of κ/M_{Pl}.

11.2 Generation of RS Monte Carlo Events

In order to test my new physics hypothesis I need a Monte Carlo model for the events. The first ten RS graviton resonances are implemented in `MadEvent` in the `topBSM` model [21]. The mass of the first resonance, and κ/M_{Pl}, can be adjusted; the widths of the resonances are calculated internally. I generate $p\overline{p} \to t\bar{t} \to W^+bW^-\overline{b}$ at 7 κ/M_{Pl} points. I use the CDF standard `CTEQ5L` PDFs. The events are then passed on to `PYTHIA` [19] for showering and put through the CDF II detector simulation [61]. The cross sections, as calculated by `MadEvent`, for each κ/M_{Pl} point are given in Table 11.1.

κ/M_{Pl}	Cross Section [pb]
0.05	8.7
0.08	8.9
0.10	9.1
0.12	9.4
0.15	9.8
0.18	10.4
0.20	10.7

Table 11.1: Cross Sections for RS gravitons at various κ/M_{Pl} points.

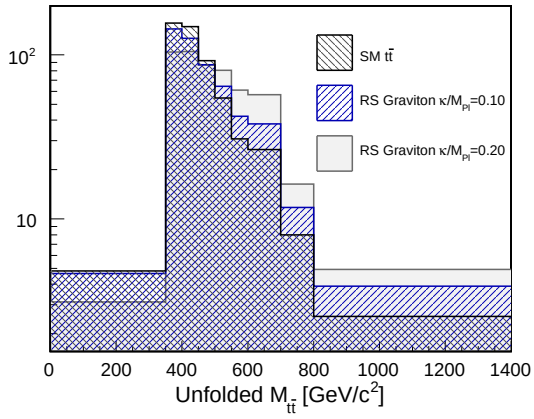

Figure 11.1: The unfolded $M_{t\bar{t}}$ distributions for the RS graviton signal and the SM background.

The unfolded $M_{t\bar{t}}$ distributions for $\kappa/M_{Pl} = 0.10$ and 0.20, along with the SM background distribution, are shown in Figure 11.1. The gravitons produce broad distortions to the tail of $M_{t\bar{t}}$ spectrum which are larger for higher values of κ/M_{Pl}.

11.3 Setting Limits with CL_s

I use a modified frequentist approach to set limits described in Reference [59]. Given a test statistic X which distinguishes BSM-like outcomes from SM-like outcomes the confidence level for excluding the presence of both the new physics and the SM is $1 - CL_{s+b}$, where CL_{s+b} is given by:

$$CL_{s+b} = P_{s+b}(X \leq X_{obs}) \tag{11.2}$$

where P_{s+b} is the probability to observe X less than or equal to X_{obs}. P_{s+b} gives the significance of X_{obs} - for an ensemble of experiments how often would the result be more consistent with the BSM plus SM $(s+b)$ hypothesis. The $s+b$ hypothesis is excluded at a confidence level given by the value of $1-CL_{s+b}$. While $1-CL_{s+b}$ can be used to set limits, it can be poorly behaved if there are not enough events in the data sample to account for the SM-only hypothesis. Instead the interval

$1 - CL_s = 1 - \frac{CL_{s+b}}{CL_b}$ is used. The quantity $1 - CL_b$ gives the confidence level for the SM-alone where CL_b is:

$$CL_b = P_b(X \leq X_{obs}). \tag{11.3}$$

The probability to observe $X \leq X_{obs}$ gives the consistency of the data with the SM. The confidence level, given by $1 - CL_b$ is the "p-value" for the SM-only hypothesis. This p-value must be very small to indicate a serious discrepancy with the SM. A "three sigma" deviation from the SM corresponds to a p-value of 1.3×10^{-3} while a "five sigma" deviation from the SM corresponds to a p-value of 2.87×10^{-7}.[1]

To set a 95% confidence level lower limit on the value of κ/M_{Pl} the procedure is as follows:

1. Construct the X distribution at each κ/M_{Pl} point and for the SM background.
2. Calculate CL_{s+b}, CL_b and CL_s at each κ/M_{Pl} point.
3. The 95% confidence level lower limit is given by the value of κ/M_{Pl} where $1 - CL_s = 0.95$.

The expected limits can be calculated in pseudo-experiments using SM-only events. Before I describe how I construct the X distributions, I will detail the test statistic that I use.

11.3.1 The Anderson-Darling Statistic

The Anderson-Darling statistic, denoted A^2, is a particularly useful statistic for detecting deviations in the tails of a distribution [58, 60]. I calculate A^2 by comparing the unfolded $M_{t\bar{t}}$ distribution in the data to the $M_{t\bar{t}}^{true}$ distribution in the SM Monte Carlo simulation. In the data there are N events in the unfolded distribution divided into $B = 9$ bins with d_j events in bin j. The distribution function, S_k, for the data is given by:

$$S_k = \frac{1}{N} \sum_{j=1}^{k} d_j, \qquad k = 1, ..., 9 \tag{11.4}$$

The SM $M_{t\bar{t}}^{true}$ distribution has M events in $B = 9$ bins with d'_j events in bin j. The distribution function for the SM, S'_k, is given by:

$$S'_k = \frac{1}{M} \sum_{j=1}^{k} d'_j, \qquad k = 1, ..., 9 \tag{11.5}$$

The Anderson-Darling statistic is defined as:

$$A^2 \equiv \frac{NM}{N+M} \sum_{j}^{B-1} \frac{(S_j - S'_j)^2}{S''_j(1 - S''_j)} \frac{d''_j}{D''} \tag{11.6}$$

[1] The relationship between p-value and significance levels in terms of sigma is based on the Gaussian distribution. A three sigma deviation is considered significant evidence for a deviation; a five sigma deviation is required to claim discovery.

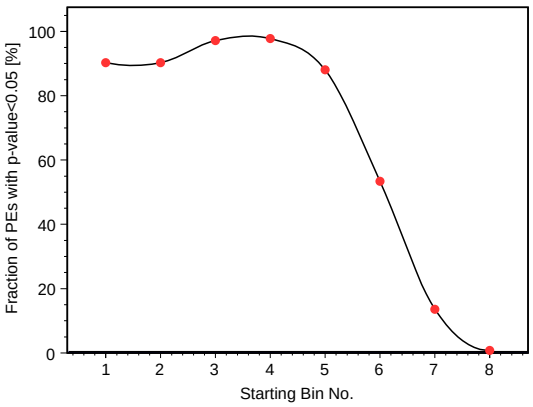

Figure 11.2: The fraction of pseudo-experiments with small p-values for a SM-only hypothesis for events in the BSM model with $\kappa/M_{Pl} = 0.15$.

where $d''_j = d_j + d'_j$, $D'' = \sum_j^{B-1} d''_j$ and S''_k is defined as in Equation 11.5 with d''_j substituting for d_j.

The distribution function is a probability distribution. S_k gives the fraction of events in the data for bin 1 to bin k, when $k = 9$, $S_k = 1$. By comparing the distribution function for the data to the distribution function in the SM, I'm looking for large deviations from the expected SM distribution function. The term $S''_j(1-S''_j)$ in the denominator of Equation 11.6 gives greater weight to deviations in the tails of the distribution.

The optimal bin range for the summation in Equation 11.6 can be found by finding the bin range which gives the best sensitivity to new physics and the best expected limit. To test the best bin range for maximum sensitivity to BSM physics I perform pseudo-experiments where the data is drawn from the Monte Carlo model of RS gravitons with $\kappa/M_{Pl} = 0.15$. I then calculate the p-value for X_{obs} in each pseudo-experiment for the SM-only model, given by $1 - CL_b$. I want to chose the bin range which gives the largest fraction of small p-values - which would indicate disagreement with the SM model. The largest disagreement with SM is seen when the A^2 sum begins with bin four. In Figure 11.3 I show the fraction of pseudo-experiments where the p-value from the RS model with $\kappa/M_{Pl} = 0.15$ is less than 0.05, which peaks for starting with the fourth bin of the $M_{t\bar{t}}$ distribution. The expected limit versus the starting bin number is shown in Figure 11.2. The best expected limit is set when starting at $j = 4$, or $M_{t\bar{t}} \geq 450$ GeV/c^2. I set limits by computing the A^2 statistic for $M_{t\bar{t}} \geq 450$ GeV/c^2.

11.3.2 Constructing the Distributions

I use a pseudo-experiment technique to construct the A^2 distribution for each model. When constructing the distribution functions for each pseudo-experiment I need to take into account two effects: statistical fluctuations in the data and systematic uncertainties on the Monte Carlo models. The distribution function for the data in each pseudo-experiment, S_k, is given by a Poisson fluctua-

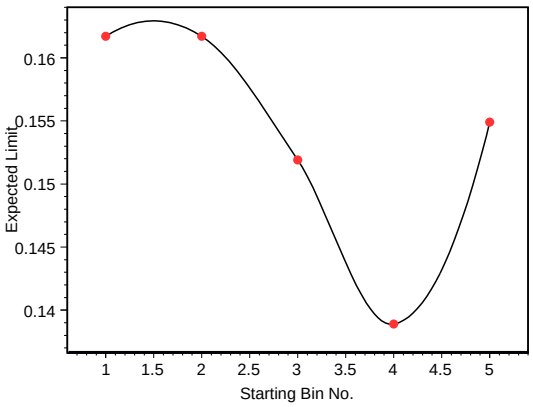

Figure 11.3: The expected limit versus the starting bin number for the summation in Equation 11.6.

tion of the expectation in the SM. To construct the distribution function for the Monte Carlo model, S'_k, an additional systematic "fluctuation" is required. This systematic fluctuation is achieved by first smearing the mean expectation in each bin of the Monte Carlo distribution, μ_i, according to the systematic uncertainty in that bin, σ_{μ_i}. Assuming Gaussian uncertainties, the mean is shifted to μ'_i, a random number pulled from a Gaussian with mean μ_i and width σ_{μ_i}. S'_k is constructed from a Poisson fluctuation of μ'_i.

The most rigorous procedure would be to perform a systematic fluctuation for each systematic uncertainty listed in Table 9.6. Each fluctuation would shift the expectation in each bin to a new value μ'_i. In practice the effect of systematic uncertainties in the Monte Carlo model produce only small changes to the A^2 distribution in my analysis. I have found that the only appreciable change to A^2 occurs when the SM is modeled with the PDF `MRST72` instead of `CTEQ5L`. Because the sum total of the systematic uncertainties would be somewhere between the SM distribution and the extreme set by the `MRST72` distribution, I take a conservative approach and use the A^2 distribution generated with `MRST72` to represent the total effect of all the systematic uncertainties. The limit I calculate will not be stronger than the limit I would calculate with the full systematic procedure implemented. At the same time, the limit will not be significantly worse because the expected limit is relatively insensitive to the systematic uncertainties.

11.4 Limits on the Coupling of RS Gravitons to Top Quarks

The distribution of A^2 in the SM-only hypothesis, compared to the distribution for two κ/M_{Pl} points is shown in Figure 11.4. I measure $A^2 = 0.61$. The confidence level for the SM alone, given by $1 - CL_b$, is 28%, which is consistent with a SM-only hypothesis. The observed confidence level at each κ/M_{Pl} point is given in Figure 11.5. I exclude $\kappa/M_{Pl} > 0.16$ at the 95% confidence level.

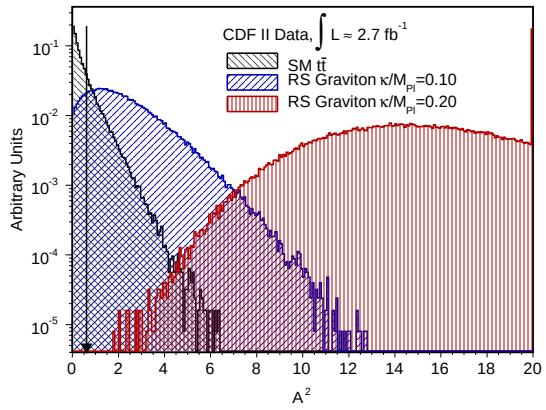

Figure 11.4: The A^2 distributions, from Monte Carlo events with the `MRST72` PDF set, for the SM-only and two BSM hypotheses. The value of A^2 in the data is shown by the arrow.

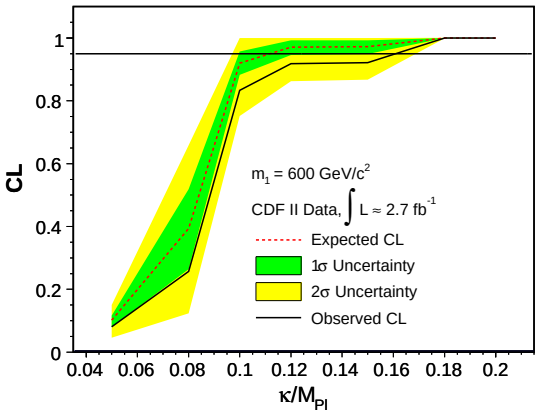

Figure 11.5: The expected and observed confidence levels for excluding κ/M_{Pl}.

Chapter 12

Conclusions

I have measured the $t\bar{t}$ differential cross section, $d\sigma/dM_{t\bar{t}}$, in 2.7 fb^{-1} of data. The p-value for this measurement, in the SM-only hypothesis, is 34%. I set a limit on the value of κ/M_{Pl} in the RS model of $\kappa/M_{Pl} > 0.16$ at the 95% confidence level by studying the coupling of KK gravitons to top quarks, where the mass of the first resonance is 600 GeV/c^2.

The unfolding technique that I have used is applicable to other measurements of the $t\bar{t}$ system. Besides $d\sigma/dM_{t\bar{t}}$, many other differential distributions provide a window to physics beyond the SM. For example, $d\sigma/dcos\theta$ provides a handle on the spin of particles which may appear as resonances in the $M_{t\bar{t}}$ distribution. This distribution will be smeared by the same effects which smear the $M_{t\bar{t}}$ distribution. If a resonance were discovered in $M_{t\bar{t}}$, study of $d\sigma/dcos\theta$ would provide additional key information about the source of the resonance.

While I have not found evidence for new physics, a large range of κ/M_{Pl} values are allowed by the limit I set. This limit could be improved at the Tevatron with the application of more data. The beginning of physics at the LHC will allow for the study of the high mass region of $M_{t\bar{t}}$ that is inaccessible at the Tevatron. In this region the higher mass KK resonances would be visible. The $M_{t\bar{t}}$ spectrum may yet provide a glimpse of new physics.

References

[1] S. Eidelman, *et al.* Physics Letters B 592 (2004)1-1109.

[2] The Tevatron Electroweak Working Group. `http://tevewwg.fnal.gov/top/`

[3] A few good textbooks covering the Standard Model are "Quarks and Leptons" by F. Halzen and A. Martin (1984); "Introduction to Elementary Particles" by D. Griffiths (1987); and "An Introduction to Quantum Filed Theory" by M. Peskin and D. Schroeder (1995). I also have relied heavily on notes from courses given at the University of Illinois by Professor A. El-Khadra.

[4] Wolfgang Wagner, "Top Quark Physics in Hadron Collisions," Rep. Prog. Phs. **68**, 2409 (2005).

[5] The ALEPH, DELPHI, L3, OPAL, SLD Collaborations, the LEP Electroweak Working Group, the SLD Electroweak and Heavy Flavour Groups, "Precision Electroweak Measurements on the Z Resonance," Phys. Rept. **427**, hep-ex/0509008 (2006).

[6] H. L. Lai *et al.* [CTEQ Collaboration], "Global QCD Analysis of Parton Structure of the Nucleon: CTEQ5 Parton Distributions,"Eur. Phys. J. C **12**, 375 (2000).

[7] M. Cacciari, *et al.* "The $t\bar{t}$ Cross-Section at 1.8 and 1.96 TeV: A Study of the Systematics Due to the Parton Densities and Scale Dependence," JHEP **040**, 068 (2004).

[8] The LEP Electroweak Working Group. `http://lepewwg.web.cern.ch/LEPEWWG/`

[9] R. Frederix and F. Maltoni, "Top Pair Invariant Mass Distribution: a Window on New Physics," hep-ph/0712.23355v1 (2007).

[10] J. Rosner, "Prominent Decay Modes of a Leptophobic Z'," Phys. Let. B **387**, 113 (1996). K. Lynch, *et al.*, "Finding Z' Bosons Coupled Preferentially to the Third Family at CERN LEP and the Fermilab Tevatron," Phys. Rev. D. **63**, 035006 (2001). M. Carena, *et al.*, "Z' Gauge Bosons at the Fermilab Tevatron," Phys. Rev. D **70**, 093009 (2004).

[11] G. Cvetic,"Top-quark Condensation," Rev. Mod. Phys. **71**, 513 (1999).

[12] C. Hill and S. Parke, "Top Quark Production: Sensitivity to New Physics," Phys. Rev. D **49**, 4454 (1994).

[13] P. Frampton and S. Glashow, "Chiral color: an Alternative to the Standard Model," Phys. Let. B **190**, 157 (1987).

[14] D. Choudhury, *et al.*, "Top Production at the Tevatron/LHC and Nonstandard, Strongly Interacting Spin One Particles," Phs. Let. B **657**, 69 (2007).

[15] L. Randall and R. Sundrum, "A Large Mass Hierarchy from a Small Extra Dimension," Phys. Rev. Let **83**, 3370 (1999).

[16] B. Lillie, *et al.*, "The Bulk RS KK-Gluon at the LHC," hep-ph/0701166 (2007).

[17] `http://www.fnal.gov/pub/inquiring/physics/accelerators/index.html`

[18] The CDF Collaboration, "The CDF II Technical Design Report," FERMILAB-Pub-96/390-E (1996).

[19] T. Sjostrand, S. Mrenna and P. Skands, "`PYTHIA` 6.4: Physics and Manual,"JHEP **05**, 026 (2006).

[20] G. Corcella, *et al.*, "`HERWIG` 6: an Event Generator for Hadron Emission Reactions with Interfering Gluons (Including Supersymmetric Processes),"JHEP **0101**,010 (2001).

[21] J. Alwall *et al.*, "`MadGraph/MadEvent` v4: the Next Web Generation," JHEP **0709**, 028 (2007).

[22] M.L. Mangano, *et al.*, "`ALPGEN`: a Generator for Hard Multiparton Processes in Hadronic Collision, "JHEP **0307**, 001 (2003).

[23] D. J. Lange, "The `EvtGen` Particle Decay Simulation Package," Nucl. Instrum. Meth. A **462**, 152 (2001).

[24] E. Gerchtein and M. Paulini, "CDF Detector Simulation Framework and Performance," CHEP03 Conference Proceedings, physics/0306031 (2003).

[25] R. Brun and F. Carminati, "`GEANT` Detector Description and Simulation Tool," CERN Programming Library Long Writeup **W5013** (1993).

[26] R. Veenhof, "`GARFIELD`, a Drift Chamber Simulation Program," Version 6.22, CERN.

[27] G. Grindhammer, *et al.*, "The Fast Simulation of Electromagnetic and Hadronic Showers," Nuc. Instrum. and Methods A **290**, 469 (1990).

[28] D. Acosta *et al.* (The CDF Collaboration), "Measurement of the Cross Section for $t\bar{t}$ Production in $p\overline{p}$ Collisions Using the Kinematics of Lepton+Jets Events," Phys. Rev. D **72**, 052003 (2005).

[29] A. Abulencia *et al.* (The CDF Collaboration), "Measurements of Inclusive W and Z Cross Sections in $p\overline{p}$ Collisions at $\sqrt{s} = 1.96$ TeV," J. Phys. G: Nucl. Part. Phys. **34**, 2457 (2007).

[30] A. Bhatti, *et al.*, "Determination of the Jet Energy Scale at the Collider Detector at Fermilab," Nuc. Instr. and Methods Phys. Research A **566**, 375 (2006).

[31] `http://www-cdf.fnal.gov/physics/new/top/2004/jets/cdfpublic.html`

[32] D. Acosta, *et al.* (The CDF Collaboration),"Measurement of the $t\bar{t}$ Production Cross Section in $p\overline{p}$ Collisions at $\sqrt{s} = 1.96$ TeV Using Lepton+Jets Events with Secondary Vertex b-tagging," Phys. Rev. D **71**, 052003 (2005).

[33] J. M. Campbell and R. K. Ellis, "An Update on Vector Boson Pair Production at Hadron Colliders," Phys. Rev. D **60**, 113006 (1999). D. Acosta, *et al.* (The CDF Collaboration), "First Measurements of Inclusive W and Z Cross Sections from Run II of the Tevatron Collider," Phys. Rev. Lett. **94**, 091803 (2005). Z. Sullivan, "Understanding Single-top-quark Production and Jets at Hadron Colliders," Phys. Rev. D **70**, 114012 (2004).

[34] U. Grundler, "A Measurement of the $t\bar{t}$ Production Cross Section in $p\overline{p}$ Collisions at $\sqrt{s} =$ 1.96 TeV Using Soft Muon Tagging," PhD Thesis, University of Illinois (2008).

[35] `http://www-cdf.fnal.gov/internal/physics/top/RunIIBtag/1200invpb_results/`

[36] T. Schwarz, A. Ivanov and R. Erbacher.
http://www-cdf.fnal.gov/physics/new/top/2008/xsection/ttbar_secvtx_3invfb/
CDF Public Note 9462.

[37] http://www-cdf.fnal.gov/physics/new/top/2008/xsection/ttbar_combined_3invfb/.
CDF Public Note 9448.

[38] A. Abulencia, *et al.* (The CDF Collaboration), "Measurement of the Top Quark Mass with the Dynamical Likelihood Method using Lepton plus Jets Events with b-tags in $p\overline{p}$ Collisions at $\sqrt{s} = 1.96$ TeV," Phys. Rev. D **74**, 092005 (2006).

[39] T. Aaltonen, *et al.* (The CDF Collaboration), "Search for Resonant $t\bar{t}$ Production in $p\overline{p}$ Collisions at $\sqrt{s} = 1.96$ TeV," Phys. Rev. Lett. **100**, 231801 (2008).

[40] A Abulencia, *et al.* (The CDF Collaboration),"Top Quark Mass Measurement Using the Template Method in the Lepton + Jets Channel at CDF II," Phys. Rev. D. **97**, 221801 (2006).

[41] T. Aaltonen, *et al.* (The CDF Collaboration), "Limits on the Production of Narrow $t\bar{t}$ Resonances in $p\overline{p}$ Collisons at $\sqrt{s} = 1.96$ TeV," Phys. Rev. D **77**, 051102 (2008).

[42] V.M. Abazov, *et al.* (The DØ Collaboration), "Search for $t\bar{t}$ Resonances in the Lepton Plus Jets Final State in $p\overline{p}$ Collisons at $\sqrt{s} = 1.96$ TeV," submitted to Phys. Rev. Let., hep-ex/0804.3664 (2008).

[43] V.M. Abazov, *et al.* (The DØ Collaboration),"Search for $t\bar{t}$ Resonances in the Lepton Plus Jets Final State in $p\overline{p}$ Collisons at $\sqrt{s} = 1.96$ TeV," DØ Public Note 5600 (2008).

[44] T. Aaltonen, *et al.* (The CDF Collaboration), "A Search for Massive Gluon Decaying to Top Pair in Lepton+Jet Channel," CDF Public Note 9164 (2008).

[45] V. Blobel, "Unfolding Methods in High Energy Physics Experiments," DESY 84-118 (1984).

[46] G. Zech, "Comparing Statistical Data to Monte Carlo Simulation - Parameter Fitting and Unfolding," DESY 95-113 (1995).

[47] V. Blobel, "An Unfolding Method for High Energy Physics Experiments," hep-ex/0208022 (2002) .

[48] A. Hocker and V. Kartvelishvili, "SVD Approach to Data Unfolding," hep-ph/9509307 (1995).

[49] M. Schmelling, "The Method of Reduced Cross-entropy: A General Approach to Unfold Probability Distributions," Nuclear Instruments and Methods in Physics Research A, **340**, 400 (1994).

[50] G. D'Agostini, "A Multidimensional Unfolding Method Based on Bayes' Theorem," DESY 94-099 (1994).

[51] C. Lawson and R. Hanson, "Solving Least Squares Problems," Prentice Hall (1974).

[52] http://www-cdf.fnal.gov/physics/new/top/2007/topProp/ttdiffXs/public/unfold/unfold.htm

[53] J. Pumplin, *et al.* (CTEQ Collaboration), "New Generation of Parton Distributions with Uncertainties from Global QCD Analysis," JHEP **0207**, 012 (2002).

[54] A. D. Martin, *et al.* (MRST Collboration), "Parton Distributions: A New Global Analysis," Eur. Phs. J. C **4**, 463 (1998).

[55] A. Abulencia *et al.* (CDF Collaboration), "Precise Measurement of the Top Quark Mass in the Lepton+Jets Topology at CDF II," Phys. Rev. Lett. **99**, 182002 (2007).

[56] A. Bridgeman and T. Liss, "Measurement of the $t\bar{t}$ Differential Cross Section, $d\sigma/dM_{t\bar{t}}$," CDF Public Note 9157.
`http://www-cdf.fnal.gov/physics/new/top/2007/topProp/ttdiffXs/public/diffXsPublic.htm`

[57] F. James, "`MINUIT` Function Minimization and Error Analysis: Reference Manual," CERN Computing and Networks Division. `http://wwwasdoc.web.cern.ch/wwwasdoc/minuit/minmain.html`
The `C++` implementation for `Root` is written by R. Brun.

[58] T.W. Anderson and D.A. Darling, "Asymptotic Theory of Certain 'Goodness of Fit' Criteria Based on Stochastic Processes," Annals of Math. Stat. **23**, 193 (1952).

[59] T. Junk, "Confidence Level Computation for Combining Searches with Small Statistics," Nuc. Instrum. and Methods in Physics Research A **434**, 435 (1999).

[60] My use of the Anderson-Darling statistic was inspired by studies completed for the CDF Run I analysis of the inclusive jet cross section $d\sigma/dE_T$. CDF Note 3419 by L. Demortier entitled "Assessing the Significance of a Deviation in the Tail of a Distribution" is available to CDF users for reference.

[61] The code for the entire `MadEvent` to `PYTHIA` to CDF simulation process was written by Nate Goldschmidt, based on code developed by the CDF Karlsruhe group.

Author's Biography

Alice Patricia Bridgeman was born and raised in West Virginia. For college she attend The Johns Hopkins University in Baltimore, MD, graduating with a B.A. in Biophysics in 2003. She began graduate school at the University of Illinois in the fall of 2003. She decided to try out high energy physics in the summer after her first year, and has stuck with it ever since. After graduation from the U of I she will work as a postdoctoral associate at Argonne National Lab. She will work as part of the STAR collaboration at RHIC and study the contribution of the gluons to the spin of the proton.